Vienna Doctoral Programme on
Water Resource Systems

Doctoral Thesis

Inverse reconstruction of wind load and stochastic response analysis from sparse long-term response measurements

Inverse Rekonstruktion von Windlasten und stochastische Reaktionsberechnung auf der Grundlage lückenhafter Langzeitmessungen

submitted in satisfaction of the requirements for the degree of
"Doctor of Science in Civil Engineering"

as part of the
Vienna Doctoral Programme on Water Resource Systems

by

MSc. Abbas Kazemi Amiri
Othmargase 21/22
1200 Vienna

Examiners

Univ.Prof. Dipl.-Ing. Dr.techn. Christian Bucher
Forschungsbereich für Baumechanik und Baudynamik
Institut für Hochbau und Technologie
TU Wien

Univ.-Prof. Dr.-Ing. Rüdiger Höffer
Windingenieurwesen und Strömungsmechanik
Fakultät fuer Bau- und Umweltingenieurwissenschaften
Ruhr-Universität Bochum

Univ.Prof. Dipl.-Ing. Dr.techn. Christoph Adam
Arbeitsbereich für Angewandte Mechanik
Institut für Grundlagen der Technischen Wissenschaften
Universität Innsbruck

Vienna, October 2016

Kurzfassung

Windlasten wirken auf verschiedene Bauwerkstypen, u.a. Wohnhäuser, Hochhäuser, Türme, Hochspannungsleitungen, Windturbinen zu Land und zur See, Kräne und Industrieschornsteine. Die Ursachen für Windschäden können unterschiedlicher Natur sein, etwa erhöhte Windlasten bei Stürmen (z.B. Orkane, Taifune), aeroelastische Instabilität, Gebäudeschäden durch plötzliche Änderung des Winddruckgradienten oder kumulative Ermüdungsschäden in Bauteilen. Aus diesem Grund wurde zur Windbeanspruchungen von Bauwerken in den letzten Jahrzehnten viel geforscht. Daher liegt auch das Hauptaugenmerk dieser Dissertation, neben anderen Arten der Anregung, bei winderregten Schwingungen.

Das Hauptziel der Dissertation ist die inverse Identifikation der Windlast, welche die Ursache winderregter Schwingungen ist. Die Bezeichnung invers deutet darauf hin, dass die Windlast nicht einfach gemessen werden kann, sondern durch ihre Auswirkungen auf die Struktur, nämlich die Strukturantwort, bestimmt wird. Dazu wird eine neue Impulsantwort-Matrix hergeleitet, welche dann zur Identifizierung der Lasten verwendet wird. Die schlechte Kondition der Impulsantwort-Matrix macht es notwendig, ein Regularisierungsschema anzuwenden, um die Last aus dem verrauschten gemessenen Antwortsignal zu identifizieren. Zur Lösung des inversen Problems wurde die *Tikhonov*-regularisierte Lösung in Verbindung mit dem generalisierten Kreuzvalidierungsverfahren (GCV) und der L-Kurven-Methode verwendet. Das Identifikationsverfahren wurde für ein einfaches Simulationsbeispiel sowie für das entsprechende Experiment implementiert. Es wird gezeigt, dass die Genauigkeit der experimentell bestimmten Lasten von der Sensibilität der Messgeräte in verschiedenen Frequenzbereichen abhängt. Im nächsten Schritt wird ein Verfahren zur inversen Windlastbestimmung präsentiert, welches auf Mehrfreiheitsgrad-Systeme angewendet werden kann und für praktische Zwecke besonders geeignet ist. Zur Steigerung von Genauigkeit und Recheneffizienz erfolgt die Lastbestimmung im modalen Unterraum. Dafür sind nur die modalen Parameter eines Systems, nämlich Eigenfrequenzen und -vektoren sowie die Dämpfungskoeffizienten, notwendig. Es wird untersucht, welcher Antworttyp geeigneter für das vorgeschlagene Verfahren zur Windlastbestimmung ist. Die Ergebnisse der Simulation für eine reale Struktur zeigen, dass die modalen Windlasten mit höherer Genauigkeit aus der Verschiebungs- als aus der Beschleunigungsantwort bestimmt werden können, selbst bei starkem Rauschen. Danach wurde das präsentierte Verfahren zur Windlastbestimmung im Feldversuch erprobt. Die Messungen erfolgten an einem 9,1 m hohen abgespannten Mast. Die modalen Windlasten werden im modalen Unterraum des Mastes identifiziert. Die experimentell ermittelten modalen Lasten wurden durch Vergleich mit den Simulationsergebnissen validiert.

Da das Wiener Doktoratskolleg (DK) Water resource systems ein interdisziplinäres Programm ist, wird viel Wert auf Forschungszusammenarbeit zwischen und innerhalb der Fachgruppen des DKs gelegt. Der Beitrag des Dissertanten zur gemeinsamen Forschungsarbeit besteht aus zwei Teilen. Der erste Teil verfolgt das zweite Ziel der Dissertation, nämlich stochastische Antwortuntersuchung einer Struktur mithilfe Daten zur mittleren Windgeschwindigkeit, wenn nur unstetige/spärliche Antwortdaten der Struktur zumindest innerhalb eines Jahres verfügbar sind. Das Ergebnis einer solchen Studie ist besonders hilfreich für

die Schwingungsdämpfung bei Windanregung. Die Daten zur Windgeschwindigkeit wurden von der Wetterstation des Hydrological Open Air Laboratory (HOAL) des DKs geliefert. Daraus wurden Histogramme und die zugehörigen Wahrscheinlichkeitsverteilungen der mittleren Wind-geschwindigkeit verschiedener Windrichtungen erhalten. Simultan zur Strukturantwort wurde auch die mittlere Windgeschwindigkeit gemessen. Die Beschleunigung des Mastes wurde mittels eines automatischen 18-Stunden Auslösers gemessen. Nach jeder Auslösung erfolgte eine zehnminütige Aufzeichnung der Beschleunigungen. Dann wurde der mathematische Zusammenhang zwischen den Daten der mittleren Windgeschwindigkeit und der Standardabweichung der Antwort, Schwellenüberschreitungen der Verschiebungsantwort und Flächenmomenten der Leistungsspektraldichte der Spannungen ermittelt.

Der zweite Teil der Gemeinschaftsarbeit des Dissertanten trägt nicht unmittelbar zu den Zielen der Dissertation bei, dennoch sind die angewandten Theorien für den Inhalt der Dissertation recht relevant. In dieser Arbeit werden die methodologischen Entwicklungen einer neuen Modellordnungsreduktions- (MOR) Strategie basierend auf "proper orthogonal decomposition" (POD) für nichtlineare dynamische Probleme präsentiert. Eine Beispielstruktur mit linearelastischem Materialverhalten sowie ein realer Krankenhausbau mit Basisisolierung aus einzelnen Reibungslagern wurden zur Bewertung der Methode herangezogen. Die Ergebnisse zeigen genaue Annäherungen der physikalischen (vollen) Antworten mittels dieser neuen MOR-Strategie, falls das wahrscheinliche Verhalten der Struktur bereits durch POD-Schnappschüsse erfasst wurde.

Die Dissertation versuchte die Effizienz der Impulsantwortmatrix von Strukturen zu verbessern und entwickelte eine praktische Vorgangsweise zur inversen Ermittlung der Windlasten auf eine Struktur - nur mittels Daten, die in der Wirklichkeit gemessen werden können. Die Dissertation liefert eine effektive Methode zur Untersuchung der langzeitigen stochastischen Antwort winderregter Strukturen, wobei das ständige Messen der Strukturantwort nicht mehr nötig ist. Diese Methode kann auch bei numerischen Simulationen eingesetzt werden, um realistischere Untersuchungen zur langzeitigen Antwort von Strukturen bei Wind zu erhalten.

Abstract

Wind can affect a wide range of structures including ordinary buildings, high-rise buildings and towers, overhead power lines, on/offshore wind turbines, cranes and industrial chimneys etc. In this sense the wind loading accounts for the destructive effects on the structures, which — depending on the particular case — can be due to wind overloads in storm event (e.g. hurricanes, typhoons), aeroelastic stability issues, architectural damages due to sudden change in wind pressure gradients or cumulative fatigue damage in structural elements. As a result wind loading of the structures has received substantial research works in the past decades. Due to this reason, the main attention in this dissertation was drawn to the wind-induced vibration of structures among other excitation sources.

The primary goal of the dissertation is inverse identification of the wind load, which is the source of wind-induced vibrations. By "inversely" it is pointed out that wind load cannot be easily measured directly and it is recovered from its effect on the structure, i.e. from the structural response. To this end new formulations to derive the impulse response matrix is provided, which is then used in the problem of load identification. The ill-conditioning of the impulse response matrix made it necessary to deploy a regularization scheme to recover the applied force from noise polluted measured response. The *Tikhonov* regularized solution in conjunction with generalized cross validation (GCV) and L-curve method were used to solve the inverse problem. The identification procedure was implemented for a simple simulation example as well as its corresponding experimental laboratory case. It is shown that the accuracy of experimentally identified load depends on the sensitivity of measurement instruments over the different frequency range. In the next step, a procedure for inverse wind load reconstruction is presented, which is applicable to multiple degrees of freedom system and is especially suitable for practical purposes. For the sake of higher accuracy and computational efficiency the load identification is performed in the modal subspace. In this way just the modal parameters of a system namely eigenfrequencies and -vectors as well as the damping ratios should be known. It is investigated, which response type is more appropriate for the proposed wind load reconstruction procedure. The results of problem simulations for a real structure demonstrate that the modal wind loads can be successfully identified more accurately from displacement than acceleration response even at relatively high noise levels. Afterwards the field application of the introduced procedure for the wind load identification was carried out. The structure under measurement is a 9.1 m (30 ft) tall guyed mast. The modal wind loads are identified in modal subspace of the mast for several single degree of freedom systems, whose characteristic parameters are obtained by an operational modal analysis procedure. The experimentally reconstructed modal loads were verified by inspecting the analogy between field and simulation results.

Since Vienna doctoral program on water resource systems (DK) is a multidisciplinary program, collaborative research works between and within research clusters of the DK is one of the main focuses of the doctoral program. The author's contribution to the collaborative research work consists of two parts. The first part pursues the second goal of the dissertation, which is stochastic response analysis of a structure assisted by mean wind speed data, when just the structure discontinuous/sparse response data at least within one year is available. The outcome of such study is remarkably helpful to the structural vibration control under wind excitations. The wind speed data was provided by the weather station, belonging to the Hydrological Open Air Laboratory (HOAL) of the DK. Thereby histogram and accordingly the mean wind speed probability distribution function of different blowing directions were obtained. Every triggered structural data was tagged by its associated mean wind speed data. The structural acceleration of the mast was measured according to an 18-hour automatic trigger. The ten-minutes acceleration data was recorded after each triggering. Then the mathematical relationship between mean wind speed data and response standard deviation, displacement response threshold passage counts and moments of area of the stress power spectral density was established.

The author's second collaboration may not directly contribute to attain the objectives of the dissertation, but the applied theories are pretty relevant to the content of the dissertation. In this collaboration, the methodical developments of a new model order reduction (MOR) strategy based on the proper orthogonal decomposition (POD) method, which applies to the nonlinear dynamic problems, are presented. An academic example structure with bilinear elastoplastic material behavior as well as a realistic hospital complex with single frictional base isolators were used to assess the introduced method. The results demonstrate accurate approximations of the physical (full) responses by means of this new MOR strategy if the probable behavior of the structure has already been captured in the POD snapshots.

The dissertation tried to improve the efficiency of the impulse response matrices of structural systems and developed a practical procedure for inverse reconstruction of wind loads on the structure, only based on the data that can be achieved via measurement in reality. The dissertation provided an effective method for long-term stochastic response analysis of structures under wind excitation, while continuous response measurement is no longer needed. This method can also be deployed in numerical simulations to achieve more realistic long-term response analysis of structures under wind.

Acknowledgements

I would like to show my sincere appreciation and respect for my dear supervisor, Professor Christian Bucher, whose supports mean to me something beyond the level of supervision. I am honored to have such a kind and literally nobel individual as my supervisor. I express my gratitudes to him for being always patient to answer my questions. He gave me the sense of bravery and ambition, to be able to work on new topics, about which I might have no idea beforehand.

I would like to thank the Austrian Science Foundation for funding this work as part of the Vienna Doctoral Programme on Water Resource Systems (DK Plus W1219-N22). I would also like to give my appreciation to Professor Günter Blöschl for conducting our doctoral program in its best way, with his unique seriousness and professional academical attitude.

I am heartily grateful to the examiners, Professor Rüdiger Höffer and Professor Christoph Adam, who accepted to dedicate their precious time to evaluate this work.

I would like to remember my deceased Professor Franz Ziegler, who taught me the alphabets of the professional academical research. I would also like to highly thank all of my previous professors and teachers, who watered my young tree of knowledge. I would also like to thank my colleagues at Forschungsbereich für Baumechanik und Baudynamik, TU Wien, for their technical helps as well as spiritual supports.

I would like to express my appreciation to Professor Takashi Maruyama (University of Kyoto, Japan) and Professor Rüdiger Höffer (Rühr Universität Bochum, Germany), who kindly hosted my abroad research stay for the dissertation.

I would like to remember my deceased grand parents, Doosti, Manidjeh, Kazem, Ebrahim and grant parents-in-law, Iran, Mansoor and Mahmood, whose love will remain in my heart forever.

I would like to deeply thank my dear parents Mahboobeh and Madjid for their exemplary supports and endless love, as well as my dear parents-in-law Mahboobeh and Hassan, for encouraging me to pursue higher education. I would also like to give my appreciation to my dear grand mother Mehrangiz and uncle Massoud for their kindness, as well as my darling brother and sister, Mehrshad and Mahkameh.

Last but certainly not least, I would like to give my love and special appreciation to my dearest, Mahnameh, for being always so supportive and motivated in our married life. My words cannot definitely express her kindness, patience and boundless wisdom in overcoming the life complications within the past years.

To my beloved kind friend, Mahnameh

Contents

List of Figures

List of Tables

Chapter 1

Introduction

1.1 Motiviation

Nowadays due to developments in technology and advancements of computers, data acquisition and measurement devices, the experimental analysis of structures plays a supplementary and important role in assessment of structures behavior. In light of this point, the main goal of the dissertation is to develop methods in structural dynamics that are applicable in field and experimental purposes especially under wind excitations. Those required data for this purpose could be obtained from measurement of structural responses or for instance mean wind speed data.

The main attention in this dissertation was drawn to the wind-induced vibration. This is due to the fact that wind affects a large variety of the man-made structures on earth. The wind effects especially wind loading on the structures, depending on the particular case, could be destructive and impose considerable costs for maintenance or enormous expenses in case of structural failures. The good knowledge on the features of wind loading turns out to a better design and analysis of the structures. However getting such knowledge is pretty difficult, since wind loads (pressure) can not be measured in real scales easily and either simulations or reduced-scale experiments must be conducted. In either case some simplifications or assumptions needs be made, that those are later translated in terms of uncertainties. Moreover wind features the long-term action, of order of decades, on the structures and it is a loading source which is almost alway present. As a result, for studying the structural response or gradual damage under wind loading, long and continuous observation is demanded, which might not be always or in every case possible.

With respect to the mentioned complications in studying of wind loading effects on the structures, two main goals are pursued in this dissertation. Those are firstly and primarily reconstruction of acting wind loads on a structure from the measured structural responses and secondly long-term structural response analysis under wind according to available sparse structural response data, assisted by the corresponding continuous record of wind speed data.

1.2 Research questions corresponding to dissertation goals

In order to develop any analysis procedure, some theoretical development is always needed beforehand and since the dissertation deals with the experimental methods, additional practical consideration should be made too. Following, the research questions with their associated chapters in the dissertation are addressed, which will come up in every stage of work to attain the mentioned goals:

- How can an efficient and accurate impulse response matrix be generated, which only requires the modal properties of the structure? (Chapter 2)
- Is it possible to reconstruct wind loads acting on a multiple degrees of freedom structures solely from measured responses? In this Chapter a procedure for this purpose is introduced and evaluated by the simulation of the problem. (Chapter 3)
- Does the field application of the introduced procedure in Chapter 3 identifies the wind loads with the quality as observed in the problem simulation? (Chapter 4)

Chapter 5 includes two sections and provides the results of collaborative research projects with two other PhD candidates, as the fulfillment of the requirements of the doctoral program. The first section of Chapter 5 concerns the second goal of this dissertation, while the second section of this Chapter may not directly correspond to the dissertation goals, however its applied methods and theories are quite relevant to the course of research in this dissertation. This Chapter answers the following research questions:

- How can wind speed data assist to analyze the stochastic response of structures under wind vibration over one year, when just the discontinuous/sparse response data is available? (Chapter 5, section 5.1)
- How could be an efficient order reduction strategy be developed, that applies to nonlinear dynamic problems? (Chapter 5, section 5.2)

The dissertation was written in the cumulative paper-based format and organized by chapters. The chapters are made of scientific manuscripts, which are either published in a scientific peer-reviewed journal, or were already submitted and consequently is in process. The content of chapters is given as follows:

Chapter 2 describes the details for deriving an augmented impulse response matrix. The applicability of the introduced impulse response matrix in wind load identification for a simple structure was successfully examined in the dynamics modeling laboratory. Chapter 2 was published in the journal of *Sound and Vibrations* (*Kazemi-Amiri and Bucher* (2015)).

In Chapter 3, the development of a practical procedure for wind load identification of real structures is, based on the findings of Chapter 2, reported. This chapter was submitted to *Mechanical systems and Signal Processing*. The accuracy of the load identification procedure was evaluated by simulation of the problem through modeling of correlated mean wind speeds. In this chapter an import issue, which is finding the proper response quantity (displacement or acceleration) for wind load identification, is also investigated.

In Chapter 4, the results of filed application to a real structure, according to the introduced method in Chapter 3, are presented. This chapter comprehensively deals with the operational modal analysis of the structure, experimental details in wind load identification and then describes the validation of reconstructed wind loads in modal subspace . Chapter 4 was submitted to the *journal of Wind Engineering & Industrial Aerodynamics*. The short version of this chapter, which only reports the experimental results briefly, was presented in a peer-review-based conference (*Movic&Rasd 2016*). This work was accepted for publication in *Journal of Physics: Conference series*.

Chapter 5, section 5.1 describes the suggested methods for stochastic response analysis of a structure under wind-induced excitations from the sparse measured response data. The one year standard deviation of structural response at an arbitrary point, a certain threshold passage probability and application to fatigue analysis were discussed in the mentioned chapter. The measurement was carried out on the same structures as in Chapter 4. This section is in preparation for submission to a journal.

Chapter 5, section 5.2 was recently accepted for publication in *Earthquake Engineering and Structural Dynamics* (*Bamer et al.* (2016)). This section provides a methodical development for model order reduction in treatment of nonlinear dynamic problems with application to earthquake engineering.

Chapter 2

Derivation of a new parametric impulse response matrix utilized for nodal wind load identification by response measurement

This paper provides new formulations to derive the impulse response matrix, which is then used in the problem of load identification with application to wind induced vibration. The applied loads are inversely identified based on the measured structural responses by solving the associated discrete ill-posed problem. To this end — either based on the parametric structural model or modal characteristics — the impulse response functions of acceleration, velocity and displacement have been computed. Time discretization of convolution integral has been implemented according to an existing and a newly proposed procedure, which differ in the numerical integration methods. The former was evaluated based on a constant rectangular approximation of the sampled data and impulse response function in a number of steps corresponding to the sampling rate, while the latter interpolates the sampled data in an arbitrary number of sub-steps and then integrates over the sub-steps and steps respectively. The identification procedure was implemented for a simulation example as well as an experimental laboratory case. The ill-conditioning of the impulse response matrix made it necessary to use Tikhonov regularization to recover the applied force from noise polluted measured response. The optimal regularization parameter has been obtained by L-curve and GCV method. The results of simulation represent good agreement between identified and measured force. In the experiments the identification results based on the measured displacement as well as acceleration are provided. Further it is shown that the accuracy of experimentally identified load depends on the sensitivity of measurement instruments over the different frequency range.

2.1 Introduction

The load identification in engineering problems becomes more important if the excitations are caused by the actions which cannot be measured directly. A good knowledge on applied loads is necessary for extraction of their characteristics or their reproduction via simulation for other purposes. The idea of direct measurement of the applied loads generally becomes more infeasible if the structure as well as the load action become more complex. For example, wind loading is one of the dominant design parameter for structures having low natural frequencies such as tall buildings or long bridges. The presence of the fluctuating wind components due to turbulence makes the wind force measurement even tougher, because more sensitive force or pressure measurement devices in huge numbers are necessary, which might not be practically realistic. On the other hand measurement of the response to the excitation is more common and better developed due to its extensive use in the other application areas such as system identification. Consequently an indirect procedure that gives the ability to identify the load from measured response — a so called inverse problem — seems to be attractive.

Load identification can be done in time or frequency domain, the best choice depends on the type of loading or the identification purposes. The authors interest is to apply the solution of this inverse problem, i.e. the inverse wind load identification, in wind fatigue analysis of a full-scale guyed-mast. Therefore it is required to prepare and evaluate a load identification procedure in the time domain, which is consistent with the methodology in the subsequent application.

For the sake of load identification we initially need to set up a complete input-output relation for the direct problem (based on already known, e.g. previously identified parameters of the structure) for two reasons. Firstly having an updated finite element model for fatigue analysis is needed. Secondly utilization of an experimental input-output model such as quasi impulse response matrix (*Jankowski* (2013)) due to its limitations is not appropriate.
Once the input-output model is generated the load identification can formally be treated in the discrete manner as a linear system of equations that is, $\mathbf{u} = \bar{\mathbf{H}}\mathbf{p}$. Unfortunately, it is an ill-posed problem since the impulse response matrix $\bar{\mathbf{H}}$ is usually ill-conditioned and the deconvolution by means of pseudo-inverse multiplication may lead to unbounded solutions in the presence of noise in measured data $\mathbf{u}$. Consequently we need to call upon alternative methods which are designed to solve discrete ill-posed problems. From a general aspect these methods are classified into direct or iterative procedures. However, neither regularization by means of projection of the problem nor the iterative regularization plus projection (c.f. *Klimer and O'Lary* (2001)) falls within the scope of this paper. Thus the solution of a discrete ill-posed problem just based on a direct scheme is dealt with. In this scheme, there are several different ways such as Tikhonov regularization (*Tikhonov and Arsenin* (1997)) and family of truncated singular value decomposition (TSVD) methods (*Varah* (1973); *Hansen* (1987)). These methods aim at filtering out the contribution of noise in the response or improving the conditioning of $\bar{\mathbf{H}}$.

It must be noted that the regularization methods need a regularization parameter as a stop criterion to tune the amplitude of smoothening of the response. The parameter selection methods are categorized into two general classes. The first class includes the methods working based on a priori knowledge about the measurement noise and the second, which is applicable independently of any knowledge about noise. The methods of generalized cross validation (GCV) (*Wahba et al.* (1979)) and L-curve (*Lawson and Hanson* (1974); *Hansen and O'Lary* (1993)) are two examples of the second class. Also it has been recommended to evaluate which parameter selection method is more efficient according to the nature of the certain problem.

In this paper the regularization method of Tikhonov for the regularization together with two procedures of GCV and L-curve for finding the regularization parameter, were selected. We provide the results of load identification via simulation and laboratory experiments for a rigidly clamped cantilever beam. The applied loads are realized by white noise limited to 25 Hz and wind excitation, which are identified separately from measured displacement and acceleration response by means of the derived ordinary and augmented impulse response matrices.

2.2 Dynamic response analysis of discrete-time systems

In this section an input-output relation in a discretized time domain is constructed. In other words we are going to build the impulse response matrix, which when it is multiplied by the input signal (i.e. force record), renders the output as time history of displacement. In this chapter this aim was reached by means of modal analysis since its closely consistent with modal testing methods of system identification in practical cases. It is mentioned here that the input-output relation might be alternatively also derived via testing, mathematical system identification (*Juang* (1994)) or simulation of application of impulsive loads on degrees of freedom when the finite element model of the structure exists.

2.2.1 Impulse response matrix

The linear equations of motion for an MDOF system with classical damping are given in the following system of differential equations:

$$\mathbf{m}\ddot{\mathbf{u}} + \mathbf{c}\dot{\mathbf{u}} + \mathbf{k}\mathbf{u} = \mathbf{p}(t) \tag{2.1}$$

while $\mathbf{u}$, $\mathbf{m}$, $\mathbf{c}$, $\mathbf{k}$ denote the displacement, mass, damping and stiffness of the system as well as the dynamic force $\mathbf{p}$, which applies on the system's degrees of freedom.
Projecting Eq. (3.1) onto modal coordinates by means of substitution $\mathbf{u}(t) = \mathbf{\Phi}\mathbf{q}(t)$ together with premultiplying each term in the equation by $\mathbf{\Phi}^T$ renders the set of uncoupled modal equations of motion (*Ziegler* (1998))

$$\ddot{\mathbf{q}} + 2\, diag[\zeta_i \omega_i]\, \dot{\mathbf{q}} + diag[\omega_i^2]\, \mathbf{q} = \mathbf{P}(t) \tag{2.2}$$

Each single equation in the system of Eq. (5.10) may be solved by means of a convolution integral (Duhamel's integral) and the response in all modal coordinates in a compact form is

$$\begin{bmatrix} q_1 \\ \vdots \\ q_n \end{bmatrix} = \int_0^t \begin{bmatrix} h_1(\tau) & & 0 \\ & \ddots & \\ 0 & & h_n(\tau) \end{bmatrix} \begin{Bmatrix} P_1(t-\tau) \\ \vdots \\ P_n(t-\tau) \end{Bmatrix} d\tau = \int_0^t \mathbf{h}(\tau)\, \mathbf{\Phi}^T\, \mathbf{p}(t-\tau)\, d\tau \tag{2.3}$$

where n denotes the number of degrees of freedom. The impulse response function $h(\tau)$ can be calculated mathematically by solving the SDOF equation of motion. Then we move backward and incorporate the responses to all vibration modes i.e. computing the superimposed response in the global coordinates. Hence Eq. (3.13) is premultiplied by $\mathbf{\Phi}$ which yields the response in the global coordinates

$$\mathbf{u} = \int_0^t \underbrace{\mathbf{\Phi}\, \mathbf{h}(\tau)\, \mathbf{\Phi}^T}_{\bar{\mathbf{h}}}\, \mathbf{p}(t-\tau)\, d\tau \tag{2.4}$$

For numerical evaluation of the convolution integral, $\bar{\mathbf{h}}(\tau)$ and $\mathbf{p}(t-\tau)$ might be assumed to be constant within the time step. Then the discrete-time-domain response becomes (*Meirovitch* (1980))

$$\mathbf{u}(k\Delta t) \approx dt \sum_{j=0}^{k-1} \bar{\mathbf{h}}_j\, \mathbf{p}_{k-j-1} \tag{2.5}$$

while k and dt stand for the total number of time steps and the length of which, respectively. At each time step the matrix of impulse response functions is computed as $\bar{\mathbf{h}}_j = \bar{\mathbf{h}}(j\,dt)$ and $\mathbf{p}_{k-j-1}$ refers to the discretized force at the time step $k-j-1$. The final task in creating the displacement impulse response matrix namely $\bar{\mathbf{H}}$ is rearranging the previous equation in the matrix form. The resulting impulse response matrix due to its ordinary integral scheme is called $\bar{\mathbf{H}}_{Ord}$.

$$\begin{bmatrix} \begin{Bmatrix} u_1 \\ \vdots \\ u_n \end{Bmatrix}_1 \\ \vdots \\ \begin{Bmatrix} u_1 \\ \vdots \\ u_n \end{Bmatrix}_k \end{bmatrix} = dt \underbrace{\begin{bmatrix} \bar{\mathbf{h}}_0 & & & 0 \\ \bar{\mathbf{h}}_1 & \bar{\mathbf{h}}_0 & & \\ \vdots & \vdots & \ddots & \\ \bar{\mathbf{h}}_{k-1} & \bar{\mathbf{h}}_{k-2} & \cdots & \bar{\mathbf{h}}_0 \end{bmatrix}}_{\bar{\mathbf{H}}_{Ord}} \begin{bmatrix} \begin{Bmatrix} p_1 \\ \vdots \\ p_n \end{Bmatrix}_0 \\ \vdots \\ \begin{Bmatrix} p_1 \\ \vdots \\ p_n \end{Bmatrix}_{k-1} \end{bmatrix} \tag{2.6}$$

The above approximation becomes very inaccurate especially when the loading record includes high frequency components.

2.2.1.1 Augmented impulse response matrix

For a better accuracy of numerical methods for approximating the dynamic response a small time step is necessary. Unfortunately, selection of a smaller time step leads to a larger $\bar{\mathbf{H}}$ and accordingly larger size of problem in load identification. In parallel with growth of size of problem the regularization becomes computationally more demanding. Therefore another way of improving the efficiency of $\bar{\mathbf{H}}$ was sought in which the size of problem is kept constant. In this regard we introduce *augmented* impulse response matrix, which is generated by means of linearly interpolating the forces (sampled discrete values) between consecutive steps in an arbitrary number of sub-steps. The discretization pertaining to the augmented impulse response matrix is depicted in Fig. 2.1.

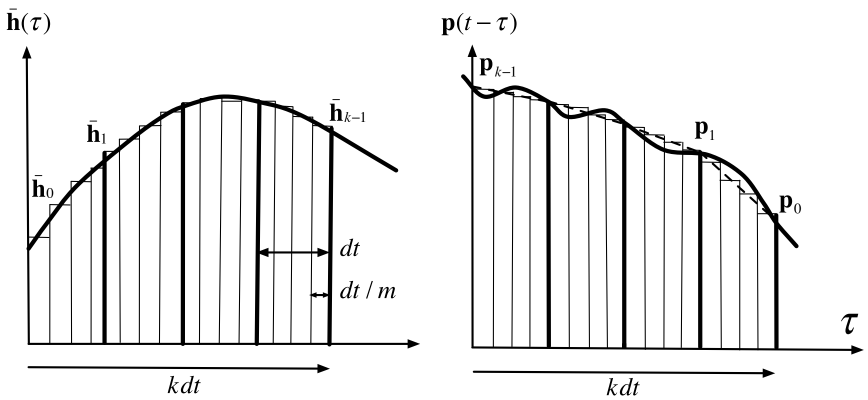

Figure 2.1: Evaluation of convolution integral considering the force interpolation

After applying the trapezoidal rule, the discretized displacement response is computed by means of augmented impulse response in the following form:

$$\begin{bmatrix} \begin{Bmatrix} u_1 \\ \vdots \\ u_n \end{Bmatrix}_0 \\ \vdots \\ \begin{Bmatrix} u_1 \\ \vdots \\ u_n \end{Bmatrix}_k \end{bmatrix} = \underbrace{\frac{dt}{2m^2} \begin{bmatrix} 0 & & \cdots & & 0 \\ \bar{\mathbf{H}}_{1,1} & \bar{\mathbf{H}}_{1,2} & & & \\ \bar{\mathbf{H}}_{2,1} & \bar{\mathbf{H}}_{2,2} & \bar{\mathbf{H}}_{1,2} & & \vdots \\ \vdots & \vdots & \ddots & \ddots & \\ \bar{\mathbf{H}}_{k-1,1} & \bar{\mathbf{H}}_{k-1,2} & \cdots & \bar{\mathbf{H}}_{2,2} & \bar{\mathbf{H}}_{1,2} \end{bmatrix}}_{\bar{\mathbf{H}}_{Aug}} \begin{bmatrix} \begin{Bmatrix} p_1 \\ \vdots \\ p_n \end{Bmatrix}_0 \\ \vdots \\ \begin{Bmatrix} p_1 \\ \vdots \\ p_n \end{Bmatrix}_k \end{bmatrix} \tag{2.7}$$

The augmented impulse response matrix, $\bar{\mathbf{H}}_{Aug}$, consists of the following components:

$$\bar{\mathbf{H}}_{u,v} = \mathbf{\Phi} diag\left[h_{u,v_1} \cdots h_{u,v_n}\right] \mathbf{\Phi}^T \tag{2.8}$$

while $h_{u,v}$ denotes the element of the following matrix at n-th mode

$$\mathbf{h}_n = \begin{bmatrix} a_{1,1} & b_{1,2} & & \cdots & 0 \\ a_{2,1} & c_{2,2} & b_{2,3} & & \\ \vdots & \vdots & \ddots & \ddots & \vdots \\ a_{k-1,1} & c_{k-1,2} & \cdots & c_{k-1,k-1} & b_{k-1,k} \end{bmatrix} \tag{2.9}$$

Then the components of $\mathbf{h}_n$ are obtained as:

$$a_{j,1} = \sum_{p=0}^{m-1} (2p+1) h_{j+\frac{2p-1}{2m}-1} \tag{2.10a}$$

$$b_{j,j+1} = \sum_{p=0}^{m-1} (2(m-p)-1)\, h_{\frac{2p-1}{2m}} \tag{2.10b}$$

$$c_{j,k+1} = \sum_{k=0}^{j-1} \left(\sum_{p=0}^{m-1} (2p+1) h_{j+\frac{2p-1}{2m}-2} + \sum_{p=m}^{2m-1} (4m-2p-1) h_{j-k+\frac{2p-1}{2m}-2} \right) \tag{2.10c}$$

2.2.2 Complete set of discrete dynamic response

For a full formulation of input-out setup, the impulse response functions of displacement, velocity and acceleration should be known. Afterwards depending on the type of the response sensor attached to any degrees of freedom, the applied force may be inversely identified.
The impulse response function of the displacement is a well-known function and available in a couple of publications *Meirovitch* (1980); *Chopra* (1995); *Clough and Penzien* (1995). Thus the impulse response functions of velocity and acceleration for a single mode need to be determined. These functions were calculated by solving the equation of motion of an SDOF system under impulsive force and are given through Eqs. (2.11) for $t \geq 0$.

$$h(t) = \frac{e^{-\zeta\,\omega_n t}}{m\,\omega_d} sin\omega_d\, t \tag{2.11a}$$

$$\dot{h(t)} = \frac{e^{-\zeta\,\omega_n t}}{m\,\omega_d} \left[\omega_d\, cos\omega_d\, t - \zeta\,\omega_n\, sin\omega_d\, t\right] \tag{2.11b}$$

$$\ddot{h(t)} = \frac{1}{m} \left[\delta(t) - \frac{e^{-\zeta\,\omega_n t}}{\omega_d} (2\zeta\,\omega_n \omega_d\, cos\omega_d\, t + \omega_n^2\, sin\omega_d\, t)\right] \tag{2.11c}$$

where $\delta(t)$ denotes the Dirac delta function.

With the similar reasoning to reach Eq. (2.4) and using the corresponding function from Eqs. (2.11), the dynamic response of velocity and acceleration can be calculated. Consequently the complete set of responses of an n degrees of freedom system for an excitation interval discretized in k time steps are available by using any discretization scheme, as below:

$$\{\mathbf{u}\}_{k*n} = \left[\bar{\mathbf{H}}_d\right]_{(k*n)(k*n)} \{\mathbf{p}\}_{k*n} \tag{2.12a}$$

$$\{\dot{\mathbf{u}}\}_{k*n} = \left[\bar{\mathbf{H}}_v\right]_{(k*n)(k*n)} \{\mathbf{p}\}_{k*n} \tag{2.12b}$$

$$\{\ddot{\mathbf{u}}\}_{k*n} = \left[\bar{\mathbf{H}}_a\right]_{(k*n)(k*n)} \{\mathbf{p}\}_{k*n} \tag{2.12c}$$

These relations might be reduced in the absence of either any response sensors or excitations in a single node.

2.3 Load identification using regularization method

There is a couple of methods dealing with providing a good solution for the system of linear equations $\mathbf{u}_{poll} = \bar{\mathbf{H}}\,\mathbf{p}$ when the matrix $\bar{\mathbf{H}}$ is ill-conditioned and the vector $\mathbf{u}_{poll}$ is polluted by noise. Here we use *Tikhonov* regularization method (*Tikhonov and Arsenin* (1997)), which has the following form

$$min\left\{\left|\left|\mathbf{u}_{poll} - \bar{\mathbf{H}}\,\mathbf{p}\right|\right|^2 + \alpha^2\,||\mathbf{p}||^2\right\} \tag{2.13}$$

The norm sign here as well as in the subsequent equations denotes the *Euclidean* norm. The difficulty with solving the optimization problem Eq. (2.13) is how to choose the appropriate parameter α (referred to as regularization parameter) because the solution is sensitive to its choice.

2.3.1 Selection of regularization parameter

2.3.1.1 L-curve

L-curve is the log-log plot of the smoothened solution versus the residual norm, corresponding to different values of regularization parameter. Depending on the selection of regularization parameter, there is a trade-off between residual norm and the size of solution. Hence L-curve aims at finding the balancing regularization parameter, which should lie on the corner of L-curve. This corner can be approximately recognized as the point on which the curvature of L-curve is maximal. As a result, the problem of parameter selection changes to finding such an α, which is the minimizer of negative value of L-curve's curvature (*Hansen and O'Lary* (1993)).

2.3.1.2 GCV

This method suggests to solve the following constrained optimization problem for load identification to restrict the norm of load response

$$min \left\{ \frac{1}{n} \left|\left| \mathbf{u}_{poll} - \bar{\mathbf{H}}\,\mathbf{p} \right|\right|^2 + \lambda \, ||(\mathbf{p})||^2 \right\} \tag{2.14}$$

while n is the number of rows of $\bar{\mathbf{H}}$. It could be interpreted as Tikhonov regularization in which α is chosen as $\sqrt{n\lambda}$.

This method approximates the regularization parameter as the minimizer of the function (*Wahba et al.* (1979))

$$V(\lambda) = \frac{1}{n} \left|\left| \left(\mathbf{I} - \bar{\mathbf{H}}\hat{\bar{\mathbf{H}}}(\lambda) \right) \mathbf{u}_{poll} \right|\right|^2 \Bigg/ \left[\frac{1}{n} Trace \left(\mathbf{I} - \bar{\mathbf{H}}\hat{\bar{\mathbf{H}}}(\lambda) \right) \right]^2 \tag{2.15}$$

while $\hat{\bar{\mathbf{H}}}(\lambda) = \left(\bar{\mathbf{H}}^T \, \bar{\mathbf{H}} + n\lambda I \right)^{-1} \bar{\mathbf{H}}^T$ is the matrix, which maps $\mathbf{u}_{poll}$ onto the solution $\mathbf{p}$. In other words $\mathbf{p}$ is the solution of minimization expression in Eq. (2.14) i.e. $\mathbf{p} = \hat{\bar{\mathbf{H}}}\,\mathbf{u}_{poll}$

2.4 Numerical results

In the first step the solutions of direct problem, i.e. dynamic response analysis, by means of ordinary and augmented response matrices are compared. These results, provided in Section 2.4.1, aim at justifying the introduction of augmented impulse response matrix.
Secondly we provide the numerical results of inverse problem in terms of simulation and experimental laboratory-scale load identification, respectively in Sections 4.4.1 and 2.4.3. The inverse problem has been solved by means of regularization methods.

The case study is a rigidly clamped aluminum alloy cantilever, which has been modelled as a single degree of freedom system. As a result there is always one unknown force versus a single measured structural response. The system parameters of the equivalent mass-spring-dashpot model corresponding to the cantilever has been identified, which are given in Section 2.4.3.1. The identified system parameters were utilized to construct the parametric impulse response matrices for numerical and experimental load identification in Sections 4.4.1 and 2.4.3.

The codes needed for the procedure of load identification have been implemented in slangTNG (*Bucher and Wolff* (2013)). The results gained from slangTNG were cross-checked with those achieved from Regularization toolbox (*Hansen* (2007)), which showed good agreement with each other.
The accuracy of the identified load, $\mathbf{p}_{ident.}$, with respect to the actual force i.e. $\mathbf{p}_{act.}$ is evaluated by the following definition:

$$Error(\%) = ||\mathbf{p}_{ident.} - \mathbf{p}_{act.}|| \, / \, ||\mathbf{p}_{act.}|| * 100 \tag{2.16}$$

2.4.1 Response comparison of ordinary and augmented schemes

It was already stated in Section 2.2.1.1 that the computed structural response by augmented scheme has more accuracy over the ordinary scheme. Our investigations show that by increasing the number of sub-steps in augmented scheme its corresponding response is improved. This leads to the faster convergence of augmented scheme compared to the ordinary one in computing the dynamic response, thus consequently leads to a smaller size of problem in the load identification. In Fig. 2.2 we demonstrate the displacement response under wind loading computed by ordinary and augmented impulse response matrix in comparison with the Newmark method response as the benchmark method. In this example the structure is a single degree of freedom system with the same specifications as those of the laboratory case study given in section 2.4.3.1. In wind load simulation the data time step was taken to be 0.1 sec. The time step to calculate the displacement response was set to 0.034 sec. Therefore the wind force data was linearly interpolated to obtain the same time step length. The number of sub-steps in computing the displacement response based on augmented scheme is 1 and 5 respectively. The comparison between the computed response of augmented scheme in Fig. 2.2a and Fig. 2.2b indicate that in a given time step length with increasing the number of sub-steps an accurate response by augmented scheme is obtained. On the other hand the response from ordinary impulse matrix given in Fig. 2.2a has not still converged, which means the length of time step for ordinary scheme has yet to be shortened. It has been observed that the response by augmented scheme changes very slightly for sub-steps $m > 5$.

2.4.2 Simulation of load identification

In order to simulate the measured structural response, white noise was added to the computed ”displacement responses” of the structure under the actual force. Then this noise-polluted displacement response was used for the load identification purpose. The magnitude of the additional noise was scaled with respect to the standard deviation of the actual response and adjusted by defining a noise level multiplier. In the numerical simulation of load identification, the number of sub-steps for construction of augmented impulse response matrix i.e. m considered to be 5.

Firstly the recovering of a white noise excitation limited to 25 Hz is simulated. The duration of excitation, noise level and sampling rate are 5 sec, 2.5% and 120 sec^{-1} respectively. The simulation of identification was run several times and it was observed that both identification methods are stable in recovering the force based on the noisy displacement response. Use of the word ”stable” means that the optimal regularization parameter can be found based on the criteria of L-curve or GCV as many as times the load identification was repeated. Moreover the identified forces obtained by using the augmented impulse response matrix were recovered more accurately than those obtained by using the ordinary impulse response matrix (c.f. Table 2.1). Fig. 2.3 represents the comparison of the identified white noise with the actual force.

In order to evaluate the consistency of identification methods for wind load, the fluctuating parts of wind velocity and correspondingly wind loads were generated. This was done by simulating a one dimensional single variable stationary random process, thus just the wind velocity auto spectrum is needed. For digital simulation of wind speed, amongst existing power spectral density (PSD) functions (*Simiu and Scanlan* (1978)), Davenport's auto spectrum (*Davenport* (1961a)) was (arbitrarily) selected. The spectrum was widened and the upper frequency was extended to 30 Hz in order to cover the relatively high resonance frequency region of the structure. The wind force PSD is plotted in Fig. 2.8.
For simulation of wind load identification, the actual displacement response of the structure was polluted at 2.5% noise level. The response sampling rate and duration of excitations were respectively 180 sec^{-1} and 5 sec.

The error analysis of the identified wind loads is given in Table 2.1. The results demonstrate that the recovered wind force by use of augmented impulse response matrix via L-curve is unacceptable. This problem occurs due to the difficulty in finding the location of the L-curve corner, since many points on the L-curve have the properties to be the optimal regularization parameter based on L-curve criterion. The recovered wind forces via GCV using both impulse response matrices have the same quality and are better identified than their counterpart by means of L-curve and ordinary impulse response matrix.

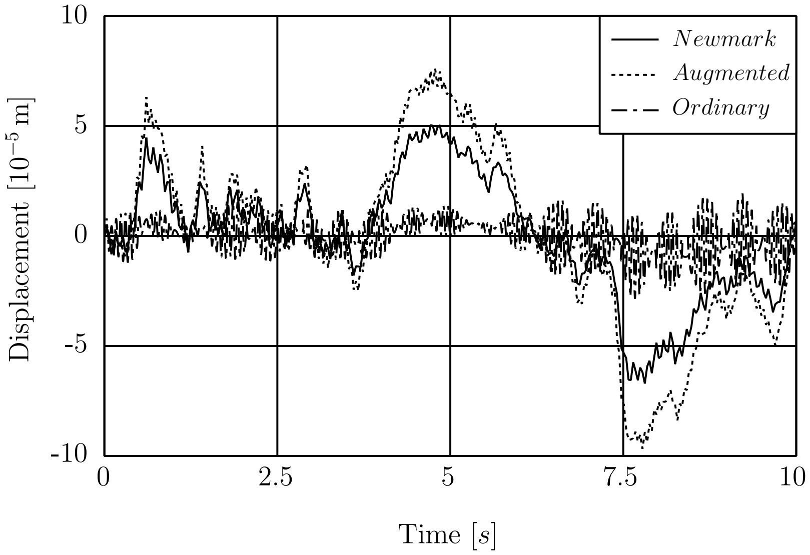

(a) Number of augmented scheme sub-steps m=1

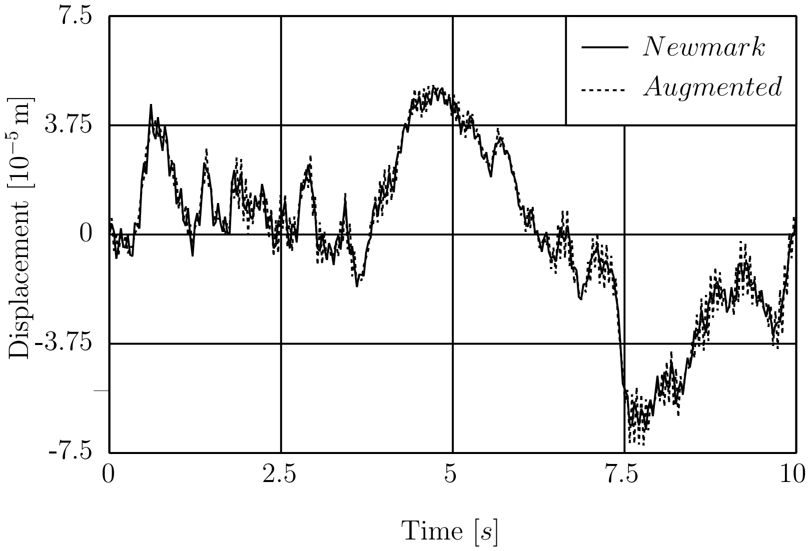

(b) Number of augmented scheme sub-steps m=5

Figure 2.2: Effect of increasing number of sub-steps in augmented scheme response of structure to wind load excitation

In Fig. 2.4 the time history of recovered wind forces based on the noisy displacement response is shown.

Table 2.1: Error (%) associated with the identified loads via simulation

Impulse response matrix	White		Wind force	
	L-curve	GCV	L-curve	GCV
Ordinary	34	35	38	29
Augmented	23	21	-*	29

* has not resulted to an acceptable response

2.4.3 Laboratory-scale load identification

2.4.3.1 Case study

As mentioned earlier the case study investigates the load identification for a vertically erected aluminum alloy cantilever whose one end is rigidly clamped. The cantilever is a rectangular beam with cross sectional dimensions 0.03 and 0.01 m as well as 0.68 m height, which is bending over its weak axis. Three sensors have been mounted on the tip of the beam. Two of them are piezoelectric accelerometers, which are used to derive the acceleration and displacement responses at the same time. The displacement response was obtained from the measured acceleration via the signal conditioner. The third sensor measures the applied force directly from the shaker. Shaker applies one point-force at the tip of the beam as well. The specifications of measurement equipments, which are the products of Brüel & Kjær, are given in Table 2.2. The picture of the whole setup is also shown in Fig. 2.5.

Table 2.2: Laboratory equipments specifications

Type	Sensitivity	Frequency range [kHz]	Measurement utility
Accelerometer 4383	3.217 [pC/ms^{-2}]	0.1-8.4	Displacement
Accelerometer 4383	3.190 [pC/ms^{-2}]	0.1-8.4	Acceleration
Force transducer 8230	3.915 [pC/N]	-*	Force
Nexus 2692	-	0.1-100	Signal conditioner

* has not been provided by the manufacturer

The configuration of loading stimulates the structure such that the first mode is the governing mode of vibration. As a result the structure has been modeled directly as a single degree of freedom system and the dynamic response of the cantilever is truncated to its first mode. Then we readily determined the first mode eigenfrequency, mass, stiffness and damping ratio. Firstly the eigenfrequency was determined by an impulse test and compared with those gained via incremental-frequency and variable-frequency harmonic excitation that was estimated nearly the same as 13.8 Hz. In order to determine the equivalent values of mast and stiffness of the cantilever (in the first mode), different lumped masses were attached on the cantilever's tip successively. Every time by observing the changes in the eigenfrequencies and from the definition of the natural frequency in term of mass and stiffness, one can setup a least squares problem and solve for the equivalent values of mast and stiffness. The damping ratio was obtained via the so-called "harmonic decay" test. The modal system parameters including mass, stiffness and damping ratio are respectively 0.2196 kg, 1666.4 Nm^{-1} and 0.07%.

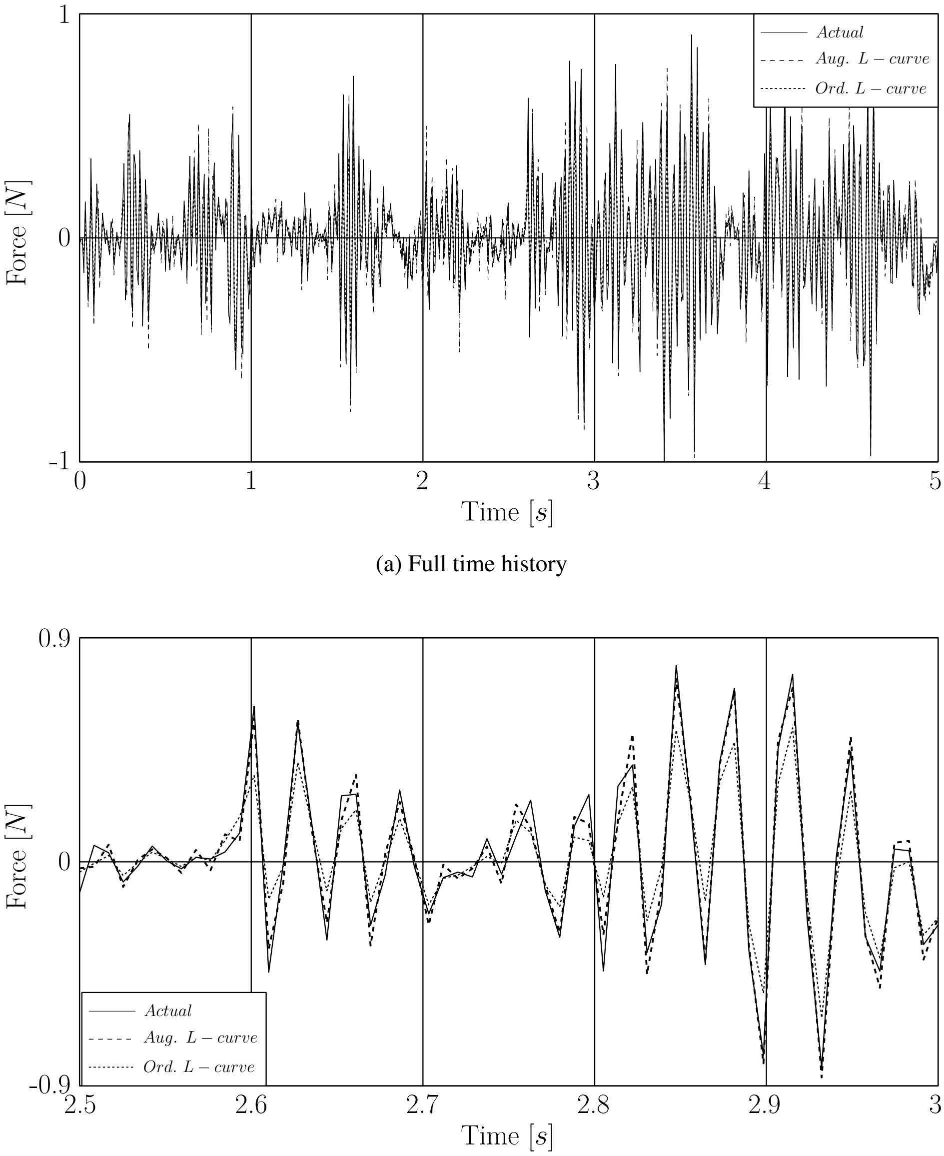

(a) Full time history

(b) A window of time history between 2.5 and 3 sec

Figure 2.3: Simulation of load identification based on noisy displacement for white noise excitation

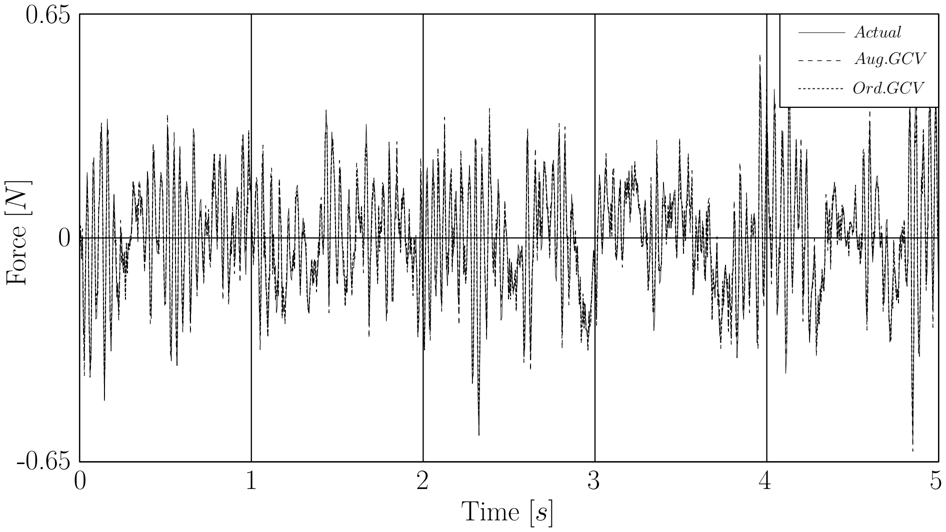

(a) Full time history

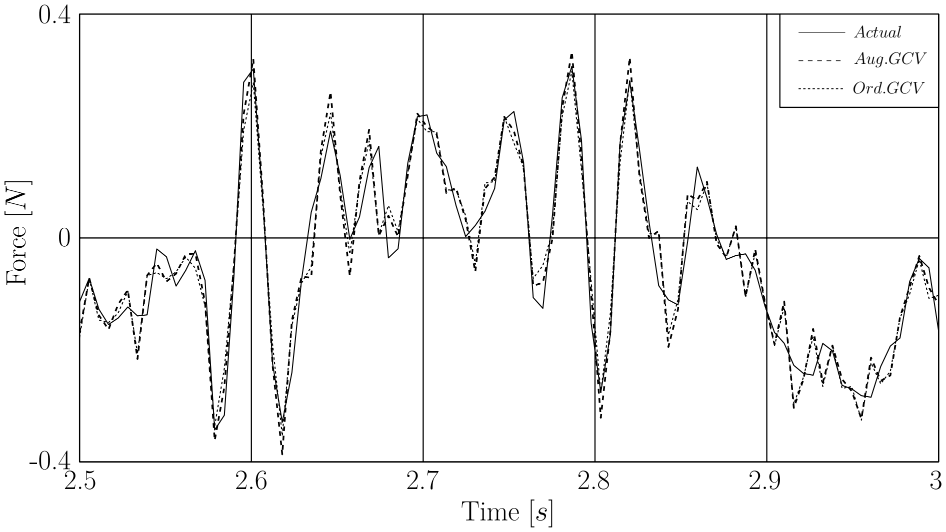

(b) A window of time history between 2.5 and 3 sec

Figure 2.4: Simulation of load identification based on noisy displacement for fluctuating wind load

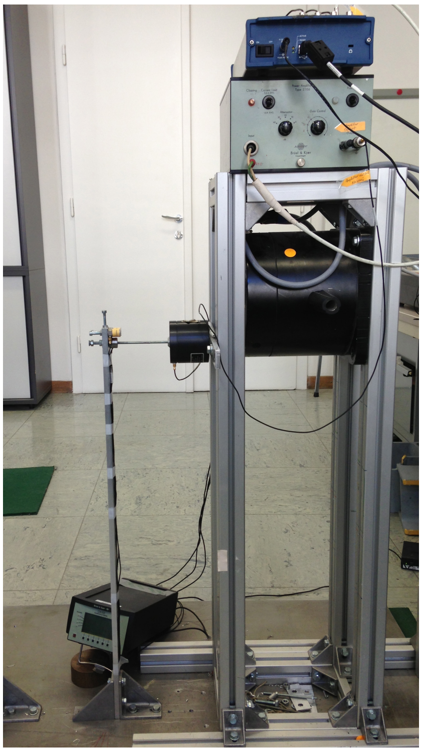

Figure 2.5: Picture of laboratory-scale setup

2.4.3.2 Experimental load identification

For the sake of experimental load identification the identification procedure was repeated for the white noise and fluctuating wind force based on measured displacement. Moreover in this section the results of the experimental wind load identification based on measured acceleration will be also provided. The acceleration responses have been used just when we initially speculated that the reason of inaccuracy in the identified wind load is related to the measured displacement response. However the main focus is on using the measured displacement response, since the L-curve or GCV function corresponding to the measured displacements were much more likely to have the standard shape, as expected in their theories, than those of the acceleration response. This will be shown later. The investigation on application of the acceleration-based wind load identification will be dealt with more in details in the forthcoming lines.

The first part of the experimental analysis again consists of identification of the white noise excitation with the same features as previously explained in Section 4.4.1. The results of experimentally recovered white noise show nearly the same accuracy with which were obtained in the corresponding numerical simulation. The identification results of white noise are provided in Table 2.3. Since the identification of white noise excitation has the satisfactory exactness alike the simulations, we end with it here and resume with the wind load identification.

The experimental wind load identification was repeated based on the measured displacement response as have been already simulated in Secion 4.4.1 for wind-type excitation. The identification results of wind load demonstrate that the recovered forces based on GCV or L-curve criteria do not have acceptable accuracy. For instance in Fig. 2.6 the comparison of identified fluctuating wind load with the actual one by means of GCV in augmented scheme has been depicted. Table 2.3 provides the wind load identification results based on different methods in both schemes. According to this table the errors corresponding to the augmented scheme are slightly smaller than the ordinary one but nevertheless not good enough.

Table 2.3: Error (%) associated with the experimental identified loads

Impulse response matrix	White		Wind force	
	L-curve	GCV	L-curve	GCV
Ordinary	31	32	61	61
Augmented	21	21	60	57

With repeating the procedure of the experimental wind force recovering under different simulated wind excitations, it was perceived that the regularization methods are stable while the recovered force is not in agreement with the measured force. It means that the optimal regularization parameters found based on the GCV and L-curve criteria do not render the identified loads of good quality.
first of all it was supposed that this problem occurs due to the high-pass filtering within double integration of acceleration response, since we have obtained the displacement from acceleration response via the signal conditioner device. Thus in order to circumvent such problem, the wind load was identified directly based on the acceleration response by selecting the third of Eqs. (2.11). Several runs of this procedure shows that slightly better or worse results may be achieved. Therefore the utilization of acceleration response does not significantly improve the identified wind load.

More inspection revealed that the displacement-based identified load divided by structure's stiffness, k, is very close to the measured displacement response. This comparison was illustrated in Fig. 2.7a. But rather as shown in Fig. 2.7b, this analogy does not exist for the white noise excitation case. Hence according to this observation, it can be concluded that the use of this kind of measured displacement response led to recovering a sort of quasi-static force. In other words the measured displacements due to the wind excitation, which has dominant low frequency components, do not sufficiently contain the portion of high frequency components of the displacement response. As a result, those parts of loading concerning the inertia and damping force are not identified.

According to this finding it was assumed that the inadequate sensitivity of the measurement sensors and not other issues regarding the identification methods, gave rise to the inaccurate identified wind loads. It was because the applied wind excitation has the characteristics that stimulated the stiffness of the structure (which belongs to lower frequency components of response) much more than its inertia (which conversely belongs to higher frequency components of response). In addition, the portion of the damping force due to the small damping ratio of structure as well as the low velocity of loading is not considerable.

One way to resolve the problem in measurement when the sensors do not have sufficient sensitivity is to amplify the amplitude of the quantity of interest, which in our case is the acceleration response. This amplification must occur before the sensor level so that the sensor be able to sense it. Therefore the excitation input must be modified. Since the acceleration response is proportional to the excitation frequency, consequently by raising the lower band of excitation frequency we can increase the amplitude of acceleration response.
To this end we filtered out different frequency ranges in the lower band of the wind power spectral density by definition of three cut off frequency ranges i.e. $\nu_{cut\ off}$ for [0 2.5], [0 5] and [0 7.5] Hz. For example the corresponding wind spectrum to $\nu_{cut\ off} = [0\ 2.5]$ is depicted in Fig. 2.8

The identification results associated with the newly simulated wind forces not only prove our second assumption but also shows that the major problem was resolved when the very low frequency excitation components i.e. between [0 2.5] Hz were filtered out. Because the accuracy of the identified newly-

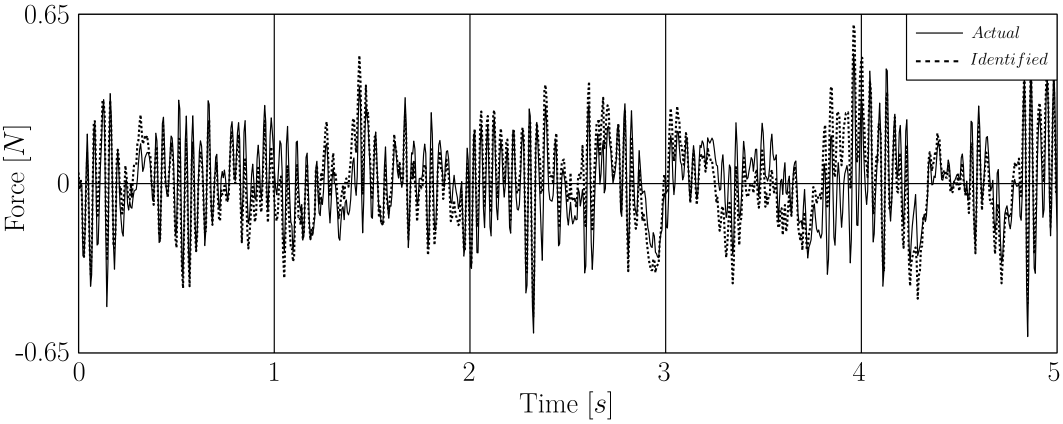

(a) Full time history

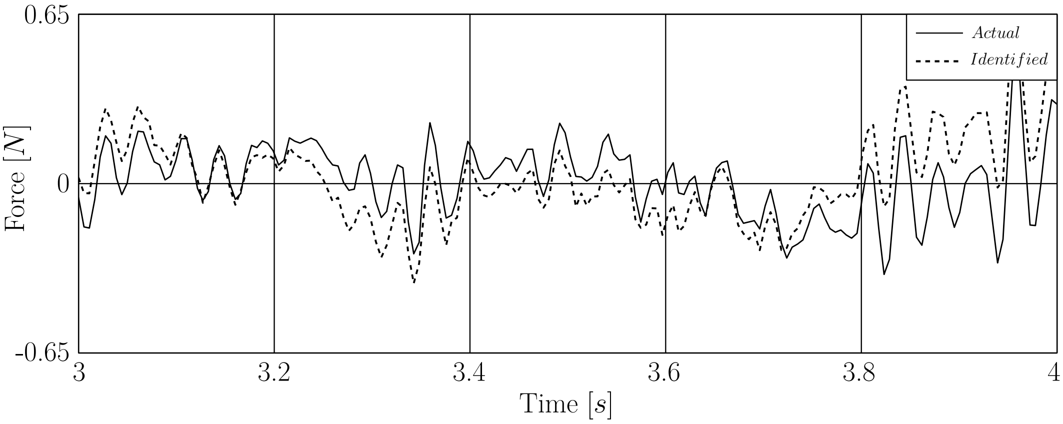

(b) A window of time history between 3 and 4 sec

Figure 2.6: Experimentally identified fluctuating wind load based on measured displacement response

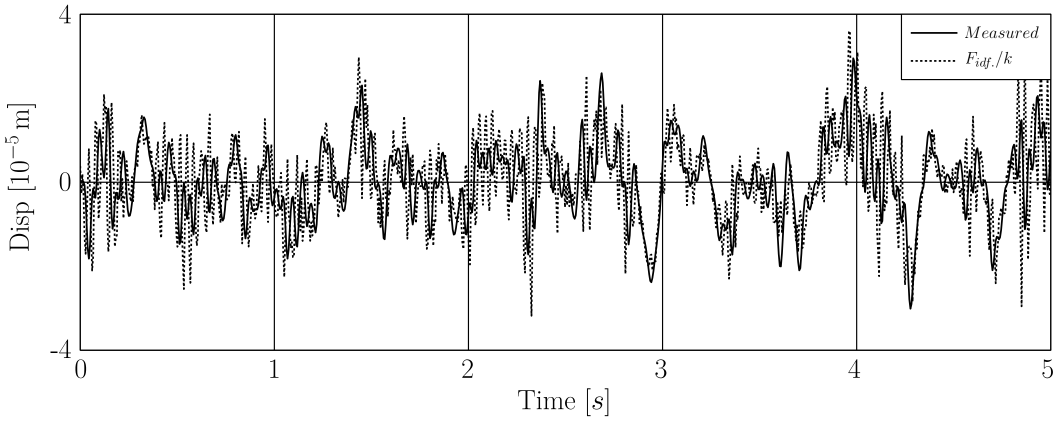

(a) Fluctuating wind excitation

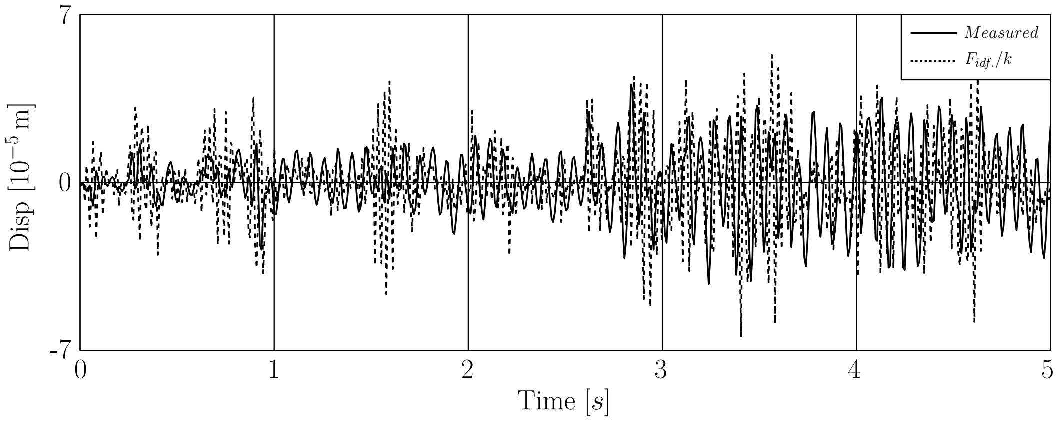

(b) White noise excitation

Figure 2.7: Comparison between measured and quasi-static displacements

generated wind loads was considerably improved by elimination of this range. It was observed that for the other two cut off ranges the improvement is insignificant. The recovered wind load with $\nu_{cut\ off} = [0\ 2.5]$ Hz by means of GCV is illustrated in Fig. 2.9. The results of identified wind loads based on measured displacement for wind loads with full frequency range as well as those with $\nu_{cut\ off}$ are provided in Table 2.4.

The problem of identification in low level vibrations could be also resolved either by use of acceleration transducer, which are appropriate for such vibrations, laser displacement sensors or by means of strain gauge instead of accelerometer as reported in *Hillary and Ewins* (1984).

The same sets of newly-generated wind excitations has been also used for force recovery by means of measured accelerations. Several times within wind load identification by means of measured accelerations, some irregularities in the shape of the curvature of L-curve or GCV minimizer have been observed that violated the L-curve and/or GCV criteria in finding the optimal regularization parameter. For instance, in Fig. 2.10 the GCV minimizer of the wind load with $\nu_{cut\ off} = [0\ 2.5]$ Hz corresponding to the ordinary impulse matrix is demonstrated. This figure reveals despite GCV's criterion, the proper identified solution is associated with the GCV parameter, which is located at the local minimum rather than the global

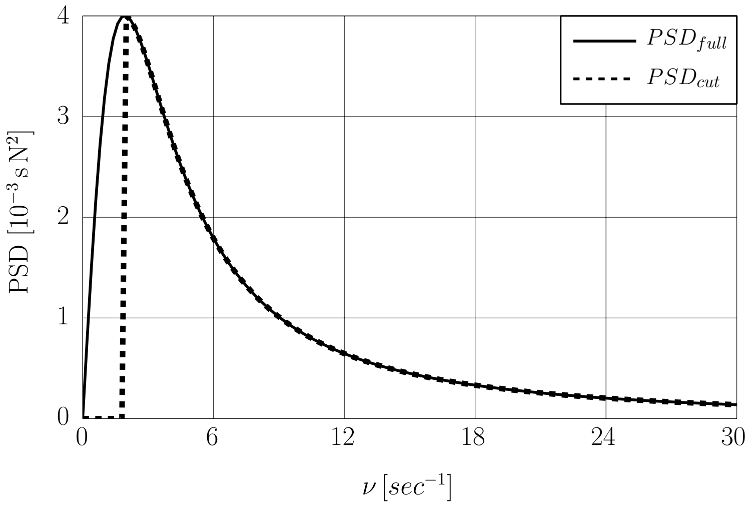

Figure 2.8: Wind force auto spectral densities for full frequency range and one with $\nu_{cut\ off} = [0\ 2.5]$ Hz

minimum. The associated error of identified wind loads based on measured acceleration responses are presented in Table 2.4. In this table the superscript-marked values correspond to the cases that the optimal regularisation parameters located at the local minimum. The trouble in these cases justifies to use the displacement response in load identification since the L-curve or GCV function corresponding to the measured displacements were nearly always well-shaped.

Table 2.4: Error (%) associated with the experimental identified loads based on measured displacement and acceleration

Cut off range [Hz]	Impulse matrix	Measurement			
		Displacement		Accelertion	
		L-curve	GCV	L-curve	GCV
–	Aug.	60	57	36*	44
	Ord.	61	61	50	48
[0 2.5]	Aug.	34	31	31	34
	Ord.	36	37	35	36*
[0 5]	Aug.	33	29	31	29
	Ord.	35	36	35	31*
[0 7.5]	Aug.	31	27	31*	31
	Ord.	34	34	34	33*

* corresponding to the regularization parameter at local minima

2.5 Conclusions

In this paper the formulations for derivation of impulse response matrices, which are used in the deconvolution problem of load identification, were presented. The dynamic loads were identified based on structural response measurement and by means of solving the corresponding inverse problem.

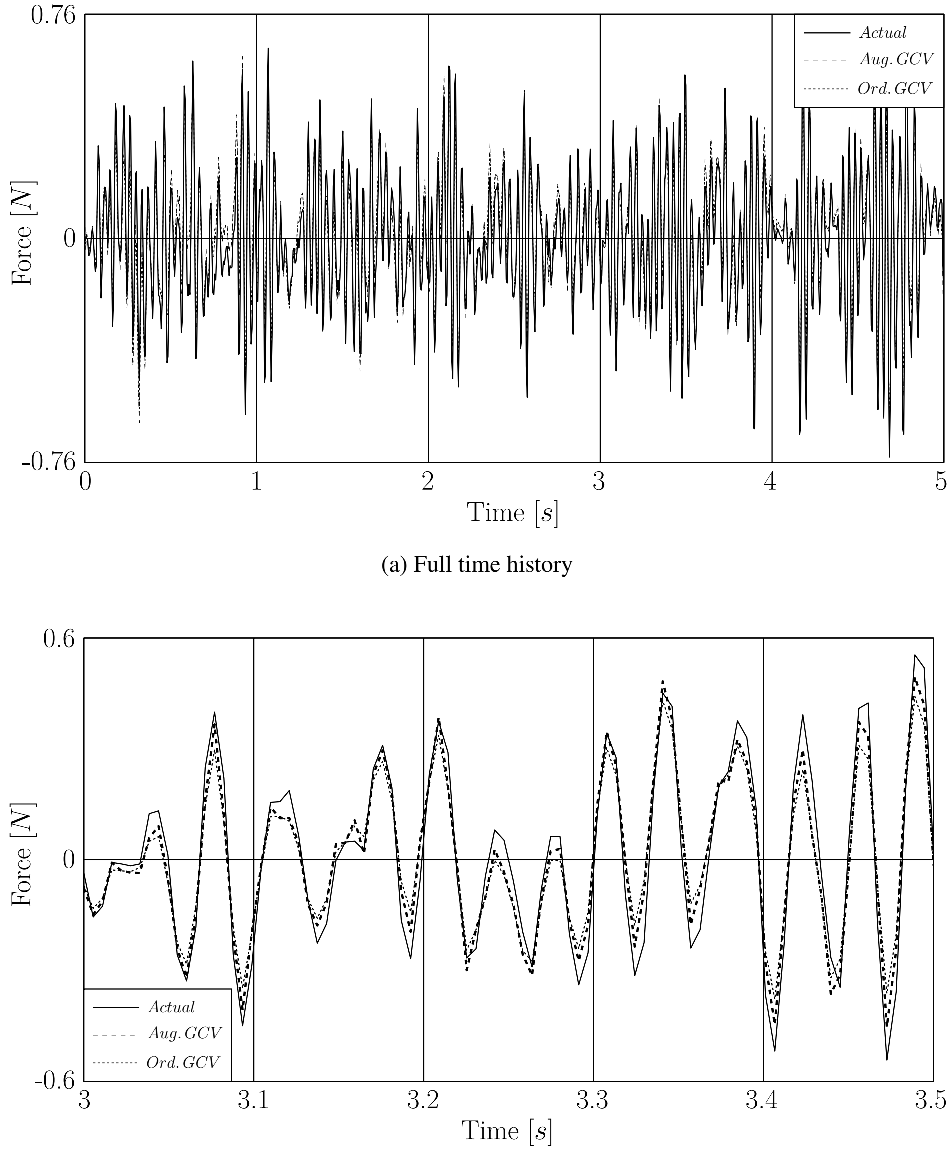

(a) Full time history

(b) A window of time history between 3 and 3.5 sec

Figure 2.9: Experimentally identified fluctuating wind load with $\nu_{cut\ off}$ between [0 2.5] Hz based on measured displacement response

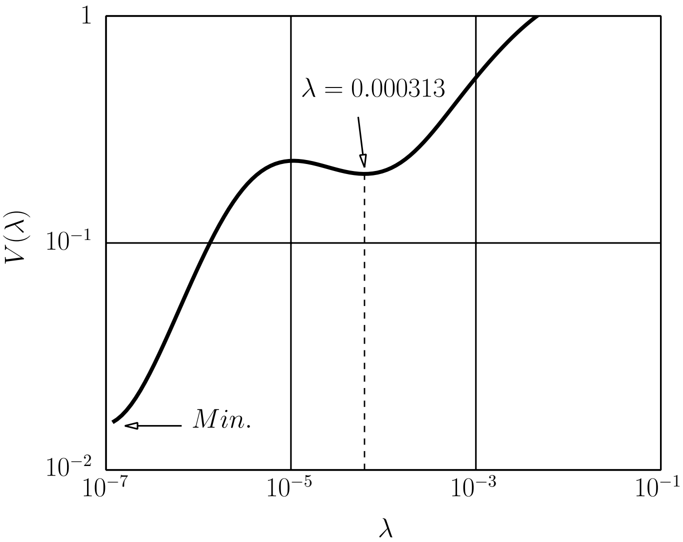

Figure 2.10: GCV minimizer in identifications by means of measured acceleration

Construction of two different types of impulse response matrices (ordinary and augmented), which are different in their integration schemes, were also presented. According to Section 2.4.1 the response via the augmented scheme converges faster than the response of the ordinary one. This is because the ordinary impulse response matrix is constructed based on the constant approximation of force within a time step. This assumption demands such a small time step in order that the approximated force resembles the real one.

Consequently in order to be able to select the time step longer than that of the ordinary scheme the augmented impulse response matrix, which interpolates the force in a number of sub-steps was introduced. However in the context of accuracy comparison, the sampling rates were selected relatively high so that the response of the ordinary scheme can converge too. Nonetheless the forces recovered by means of the augmented impulse matrix were more accurate than by the ordinary one even for such small time step lengths (c.f. Tables 2.1 and 2.4).

The identification results illustrate that the high accuracy of load identification drastically depends on the use of appropriate response sensors for different types of excitation in the sense of the contained frequency range. Otherwise the recovered force accuracy would be poor such as it occurred for the recovered wind load as was for instance shown in Fig. 2.6.

Last but not least the load identification based on the measured displacement response was observed to be more robust than acceleration based when L-curve or GCV methods are used. This is due to the fact that the L-curve and GCV criteria corresponding to the acceleration response were observed to fail way more often than when the displacement response was utilized. As a result there is the lack of robustness in the placement of the optimal regularization parameter according to those criteria (e.g. Fig. 2.10) when the acceleration response is used.

Chapter 3

A practical procedure for inverse wind load reconstruction of large degrees of freedom structures

The methodological development of a procedure for inverse wind load reconstruction from response measurement data is presented, which is especially suitable for practical purposes. To this end, according to a previous study of the authors, an "augmented impulse response matrix" (IRM) of the structure can be generated for different response types i.e displacement, velocity and acceleration. In this way just the modal parameters of a system namely eigenfrequencies and -vectors as well as the damping ratios should be known. The inverse wind load identification problem, due to its ill-posedness, is solved by means of the Tikhonov regularization scheme. For the sake of higher accuracy and computational efficiency the load identification is performed in the modal subspace, which requires to decompose the measured responses into the modal responses again by means of the modal parameters. In this contribution the acceleration and displacement responses are used to identify the applied wind load through the numerical simulation of the problem for an instrumented guyed mast. Moreover it is investigated, which response type is more appropriate for the proposed wind load reconstruction procedure. The results demonstrate that the modal wind loads can be successfully identified by the developed method more accurately from displacement than acceleration response even at relatively high noise levels, based on the comparison to the actual wind loads in time and frequency domain.

3.1 Introduction

The "cause or input identification" inversely from "effect or measured output data" is a well-known problem in different disciplines of applied mathematics and physics. There is a wide range of inverse problems (*Neto et al.* (2013)) from astronomy (*Brown and Craig* (1986)) to structural vibrations (*Gladwell* (2005)) and further to medical imaging (*Nashed and Scherzer* (2001)), image restoration (*Gunturk and Li* (2013)) and so on. The common principle in all those examples is that the direct observation of the causal factors is too difficult, while their effects can readily be recorded by the measurement apparatus.

There are many cases in structural dynamics and vibrations, in which the applied loads, e.g. wind excitation, cannot be measured directly. The knowledge on the dynamic loads properties can be considerably useful in different ways including in the pre- or post-analysis, for instance in structural health monitoring or failure analysis (*Jankowski* (2013)). Hence the recovery of the dynamic loads or the so-called "load identification” inversely from the response measurement (an inverse problem) becomes important. If it is to reconstruct the applied load in time domain where usually an impulse response matrix (IRM), as the discrete form of convolution integral, is used then the deconvolution problem is usually ill-posed due to the ill-conditioning of the IRM and noise presence in measured responses. There are several techniques for solving the force reconstruction problem, thus the reader is referred to the literature e.g. *Sanchez and Benaroya* (2014) for more information. However it is well-known that regularization methods, especially Tikhonov regularization (*Groetsch* (1984); *Tikhonov and Arsenin* (1997)), are the techniques, which generally aim at providing a stable solution, no matter how much the IRM is ill-conditioned (*Jacquelin et al.* (2003)), but indeed the optimal regularization parameter must be properly determined. In this regard there exists two methods of generalized cross validation (GCV) (*Wahba et al.* (1979)) and L-curve *Lawson and Hanson* (1974); *Hansen and O'Lary* (1993) for finding the optimal regularization parameter, while no additional information about the measurement noise is required.

Although the input identification problem has been dealt with from different aspects in the literature over the last decades (e.g. *Zhu and Law* (2002); *Azam et al.* (2015a)) however only few of those studies specialize the wind load identification problem (*Law et al.* (2005); *Hwang et al.* (2009)). The inverse wind load identification problem has some additional difficulties, which will be discussed subsequently in section 3.2.2.

In this paper the methodological development of a practical procedure for the inverse wind load identification is presented. The input-output relation is established in terms of an augmented impulse response matrix (IRM) for each mode according to a previous study of the authors (*Kazemi-Amiri and Bucher* (2015)). The measured responses will be decomposed into modal responses, that is, the problem is transformed to the load identification for a number of single degree of freedom systems. The Tikhonov regularization scheme, for resolving the ill-posedness, is utilized in combination with both L-curve and GCV for the sake of cross-check. The identified loads can be transferred from one structure's modal subspace to that of another structure provided that, strictly speaking, they have identical geometry and number of degrees of freedom. The number of modal coordinates, whose modal wind loads can be identified accurately depends on the number of the properly decomposed modal responses. This will be discussed later in sections 3.2.1 and 3.2.2.

One important focus is directed to the influence of the measured response quantity on the quality of the identified load, in a mathematical point of view. Thus the procedure has been examined for both displacement and acceleration responses as the two common types of responses in the experimental and field measurement purposes. The procedure is verified through the numerical analysis for a 9.1 m (30 ft) meter tall instrumented guyed mast, which serves as a weather station tower in the Hydrological Open Air Laboratory Petzenkirchen (*Blöschl et al.* (2016)). The wind load along the mast has been generated numerically by simulation of the linear fluctuating part of the wind speed. The measured responses were obtained from the finite element model of the mast structure under wind excitations. The results represent the capability of the developed procedure for wind load identification of the real structures with significant number of degrees of freedoms.

3.2 Development of the modal wind load identification

3.2.1 Basic equations

The aim is to set up an augmented version of the impulse response matrix for dynamic response analysis of the systems in an input-output scheme. For this purpose, the classically damped equation of motion for a multiple degrees of freedom linear system is considered (*Ziegler* (1998)).

$$\mathbf{m}\ddot{\mathbf{u}} + \mathbf{c}\dot{\mathbf{u}} + \mathbf{k}\mathbf{u} = \mathbf{p}(t) \tag{3.1}$$

In the above relation $\mathbf{u}$, $\mathbf{m}$, $\mathbf{c}$, $\mathbf{k}$ denote the displacement, mass, damping and stiffness matrices of the system as well as the dynamic force $\mathbf{p}$, which acts on the system's degrees of freedom. An uncoupled set of single degree of freedom systems can be obtained in modal coordinates through these substitutions $\mathbf{u}(t) = \mathbf{\Phi}\mathbf{q}(t)$ and $\mathbf{P} = \mathbf{\Phi}^T\mathbf{p}$:

$$\ddot{\mathbf{q}} + 2\, diag[\zeta_i\omega_i]\; \dot{\mathbf{q}} + diag[\omega_i^2]\; \mathbf{q} = \mathbf{P}(t) \tag{3.2}$$

where ζ_i, ω_i stand for the damping ratio and natural circular frequency at i^{th} mode respectively.
Each single equation in the system of Eq. (5.10) may be solved by means of convolution (Duhamel's integral) and the response in all modal coordinates in a compact form is

$$\begin{bmatrix} q_1(t) \\ \vdots \\ q_n(t) \end{bmatrix} = \int_0^t \begin{bmatrix} h_1(\tau) & & 0 \\ & \ddots & \\ 0 & & h_n(\tau) \end{bmatrix} \begin{Bmatrix} P_1(t-\tau) \\ \vdots \\ P_n(t-\tau) \end{Bmatrix} \mathrm{d}\tau = \int_0^t \mathbf{h}(\tau)\mathbf{\Phi}^{\mathrm{T}}\mathbf{p}(\mathrm{t}-\tau)\,\mathrm{d}\tau \tag{3.3}$$

where n denotes the number of degrees of freedom. The impulse response function $h(\tau)$ can be derived mathematically by solving the SDOF equation of motion.

In order to obtain the modal responses, the preceding integral can be numerically evaluated for each mode independently. For the sake of a higher accuracy, the modal response is approximated by the trapezoidal rule, which produces the input-output relation in terms of matrix multiplication through a so-called *augmented impulse response matrix* for different response types (acceleration and displacements) (*Kazemi-Amiri and Bucher* (2015)):

$$\{\mathbf{q}_i\} = \left[\bar{\mathbf{h}}_{d_i}\right]\{\mathbf{P}_i\} \tag{3.4a}$$

$$\{\ddot{\mathbf{q}}_i\} = \left[\bar{\mathbf{h}}_{a_i}\right]\{\mathbf{P}_i\} \tag{3.4b}$$

While l is equal to the total number of time steps, then $\{\left[\bar{\mathbf{h}}_{d_i}\right], \left[\bar{\mathbf{h}}_{a_i}\right]\} \in \mathbb{R}^{l*l}$ stand for the augmented modal displacement and acceleration impulse response matrices (IRM) at the ith mode, whose corresponding impulse response functions can be computed from the following equations.

$$h_i(t) = \frac{e^{-\zeta_i\,\omega_i t}}{M_i\,\omega_{d_i}} sin\omega_{d_i} t \tag{3.5a}$$

$$\ddot{h}_i(t) = \frac{1}{M_i}\left[\delta(t) - \frac{e^{-\zeta_i\omega_i t}}{\omega_{d_i}}(2\zeta_i\omega_i\omega_{d_i} cos\omega_{d_i} t + \omega_i^2 sin\omega_{d_i} t)\right] \tag{3.5b}$$

In the above relations $\delta(t)$ and ω_{d_i} are *Dirac delta function* and the damped natural circular frequency, respectively. Note that the modal shapes are usually scaled so that the modal masses become equal to unity ($M_i = 1$). For more details on the calculation of augmented response matrices, the readers are referred to (*Kazemi-Amiri and Bucher* (2015)).

One needs to decompose the measured response in order to solve the Eqs. 3.4 for the applied modal loads. For the case of fully measured degrees of freedom $\mathbf{q}(t) = \mathbf{\Phi}^{-1}\mathbf{u}(t)$ gives the modal responses. However in reality just a limited number of measurement points on the structure are available. Hence one needs to exploit another available approximate solution like the least square by means of $\mathbf{\Phi}^\dagger = \left[\mathbf{\Phi}_r^T\,\mathbf{\Phi}_r\right]^{-1}\mathbf{\Phi}_r^T$, which is the pseudo inverse of the incomplete mode shapes matrix $\mathbf{\Phi}_r$. Consequently:

$$\tilde{\mathbf{q}}(t) = \mathbf{\Phi}_r^\dagger\mathbf{u}_r(t) \tag{3.6}$$

where $\tilde{\mathbf{q}}(t)$, $\mathbf{\Phi}_r$ and $\mathbf{u}_r(t)$ denote respectively the approximated modal response, reduced identified mode shapes and measured response vector at sensor locations, all for a number of identified modes. The study on the optimal number/configuration of the sensor stays out of the scope of this contribution. But in order to make $\tilde{\mathbf{q}}(t)$ closer to its exact value there should exist more sensors than the desired number of the decomposed modal responses. Moreover all the modal responses in a certain frequency range of measurement must be decomposed. This is due to the incompleteness of mode shapes data, namely their availability just at sensor locations, and in order to assure the separation of the existing modal responses within the excitation frequency band. As a result a numerical simulation before the sensor installation can be useful to get an insight into the smallest possible number of sensors and their configuration.

Having created the modal IRMs and calculated the modal responses, $\tilde{\mathbf{P}}_i$ i.e. the estimated applied wind load at each vibration mode of the structure can be identified by means of different regularization methods. Here Tikhonov regularization method, which has received much attention and investigations in the literature has been used:

$$min\left\{\left|\left|\tilde{\mathbf{q}}_i-\bar{\mathbf{h}}_i\tilde{\mathbf{P}}_i\right|\right|^2+\lambda_i^2\left|\left|\tilde{\mathbf{P}}_i\right|\right|^2\right\} \tag{3.7}$$

wherein $||.||$ represents the Euclidean norm. In order to solve the above problem for the applied modal wind load, the regularization parameter, namely λ_i, must be determined in advance. The methods of L-curve and GCV were both utilized for finding the optimal regularization parameter. In this way, there is an advantage that the Tikhonov solutions corresponding to each method can be cross-checked too.

Assume that the modal wind loads were identified from field measurement response data by means of modal IRMs, which were constructed by use of the results of an operational modal analysis. At this point the reconstructed modal wind load can be applied for instance to an updated finite element model of the actual structure (primary structure), but of course the field identified and FEM mode shapes must have been already scaled consistently. By this the response field of the structure (i.e. of all DOFs) to the wind excitation can be generated for a number of modes. Furthermore, if the identified load is to be used for further analyses on a modified version of the initial structure (secondary structure) for generating its totally unknown response field under the same wind loading, then it is necessary to be able to transfer the identified modal wind loads of the primary structure $\tilde{\mathbf{P}}_{St_1}$ to the modal subspace of the modified one to determine the modal wind loads of the secondary structure $\tilde{\mathbf{P}}_{St_2}$. Therefore it is looked for a transfer matrix $\mathbf{T}$, so that the modal subspaces can be exchanged. Consider $\mathbf{P}=\mathbf{\Phi}^T\mathbf{p}$ and the fact that the wind load $\mathbf{p}$ in the physical subspace is identical for both structures, therefore:

$$\mathbf{T}\tilde{\mathbf{P}}_{St_1}=\tilde{\mathbf{P}}_{St_2}\ \Rightarrow\ \mathbf{T}\mathbf{\Phi}_{St_1}^T=\mathbf{\Phi}_{St_2}^T \tag{3.8}$$

Right multiplication by $\mathbf{m}_{St_1}\mathbf{\Phi}_{St_1}$, while $\mathbf{\Phi}_{St_1}^T\mathbf{m}_{St_1}\mathbf{\Phi}_{St_1}=\mathbf{I}$, then it renders:

$$\mathbf{T}=\mathbf{\Phi}_{St_2}^T\mathbf{m}_{St_1}\mathbf{\Phi}_{St_1} \tag{3.9}$$

However, in practical point of view there might exist just the modal characteristics of the primary structure, which are obtained through the operational modal analysis, while its updated finite element model and accordingly the mass matrix is not available. On the other hand it is inevitable to create the model of the secondary structure, since its model is required for the post-analysis procedure. Consequently the mass matrix of the secondary structure is available. As a result it seems quite reasonable to derive the above transfer matrix in terms of the secondary structure's mass matrix. Therefore the same scheme as above is followed such that:

$$\tilde{\mathbf{P}}_{St_1}=\mathbf{T}'\tilde{\mathbf{P}}_{St_2} \tag{3.10a}$$

$$\mathbf{T}' = \mathbf{\Phi}_{St_1}^T \mathbf{m}_{St_2} \mathbf{\Phi}_{St_2} \tag{3.10b}$$

Hence it yields $\mathbf{T} = \mathbf{T}'^{-1}$.

If the dynamic behavior of vibration prone structure is going to be improved by means of mechanical dampers e.g. TMD (*Hartog* (1956)) or TLCGD (*Ziegler* (2008); *Ziegler and Kazemi-Amiri* (2013)), the above modal subspace transferring may be unnecessary. This is due to the fact that the damper's effect can be represented in terms of an external load and consequently does not change the mode shapes of the primary structure as long as the additional damper mass compared to the structural modal mass is negligible.

It is important note that if it is to identify the modal wind loads directly from the ambient response vibration data, the mode shapes must have been already scaled correctly, as the mode shapes, which are derived by an output-only system identification methods, are not normalized with respect to the mass matrix. The mode shape scaling factors can be determined either by use of an updated finite element model (if available), or experimentally by means of other efficient methods, that work basically when just the ambient vibration data exists (*Parloo et al.* (2002); *Lopez-Aenlle et al.* (2010); *Khatibi et al.* (2012)).

In this contribution the modal subspace transferring corresponding to Step 6 was not implemented, since this work does not include post analysis on the secondary structure. However the required theory for this purpose was given as the complementary information.

3.2.2 Issues and considerations

In addition to the inherent difficulties in solving any inverse problem, the identification of wind load has its own particular complications too. Those complications, including the wind field randomness and continuousness (infinite number of unknowns), arise from the wind load nature. Consequently identification procedure should incorporate solving the corresponding inverse problem and coping with those complications. To this end the following consideration must be also mentioned: a) In order to keep the procedure sufficiently practical, it should merely need the structural modal characteristics as model parameters for establishing the IRM. In practice those parameters can be achieved by means of different system identification methods directly from the field measurement data. b) Structural response just on a limited number of points can be measured. c) The method for solving the inverse problem must be applicable to the random vibrations. Fortunately Tikhonov regularization has this capability as was demonstrated by a laboratory test in *Kazemi-Amiri and Bucher* (2015).

There are also other practical issues: Firstly the time length of the wind-induced response measurement is relatively long and of order of couple of ten minutes. Thus the IRM's size for the full or even a reduced order model of the structure will be too large, which makes the computations way too time-demanding and decreases the accuracy of the regularization method. Secondly a low number of measurement sensors are usually used. Consequently by means of a subspace transformation (e.g. modal truncation) not only the IRM's size remains computationally economic but also the underdetermined problem of wind load reconstruction will be transformed into a number of single unknown modal wind loads. The correctness of the identified load directly depends on the validity of the decomposed modal responses. The fundamental criterion to check the validity of the decomposed modal responses is: Each modal response must only have one dominant vibration frequency corresponding to the natural frequency of the system at that mode.

3.2.3 Procedure steps

Herein the steps of the wind load identification procedure is presented, as follows:

1. Identify the modal characteristics of the structural system through a system identification method in conjunction with the modal anlysis.
2. Establish the impulse response matrix of the system for a number of first modes of vibration (*see Eq.* (3.4)), dependent to the number of modes that can be identified well.
3. Decompose the measured responses acquired from different sensor channels mounted on the structure with respect to those modes by means of Eq. (4.2).
4. Check the validity of the decomposed modal responses by means of its power spectrum or simply its Fourier transform (*see section* 3.2.2).
5. Find the optimal regularization parameter for each mode by L-curve or GCV method.
6. Solve Eq. (4.4) for modal wind loads.
7. If necessary, normalize the operational mode shapes as explained in the end of section 3.2.1.
8. Transfer the identified modal wind load to another structure's modal subspace if required, through Eqs. (4.5) or Eqs. (4.7)

It is important note that steps 1 to 2 have to be carried out for each set of measurements, because in practice two reasons might lead to different identified modal characteristics:

- Change in material properties of the structures due to the temperature changes especially through different seasons or structural damage in case of relatively long-term monitoring (*Salcher et al.* (2016)).
- In case of operational modal analysis through ambient vibration testing, the identification results depend on the features of the ambient excitation. Consequently for a complex structure under a particular excitation sometimes some modes might not be excited/identified well, or in case of a system with closely located natural frequencies the order of the identified modes can be swapped from one excitation to another.

3.3 Evaluation of the wind load identification procedure

The introduced procedure will be numerically evaluated through simulation of the wind load identification problem for a guyed mast, serving as a weather station tower. The structural details of the mast side view are represented in Fig. 3.1a. The mast structure consists of three parts, each of which is made up of three main legs with the horizontal and diagonal braces. The guys connected to the third part of the mast also provide lateral support for the structure from three sides. The full-scale finite element model of the structure that was created in slangTNG (*Bucher and Wolff* (2013)) is schematically depicted in Fig. 3.1b. The structural damping was set up according to Rayleigh damping, such that the damping ratio of the first two modes was set equal to 1%. The first eight eigenfrequencies of the structure together with the damping ratios are given in Table 4.2.

3.3.1 Calculation of the noisy measured response

The displacement and acceleration responses of the mast to the wind excitations has been calculated by means of Newmark method. The wind loads were generated from digital simulation of the linear fluctuating part of the wind pressure and applied in two in-plane perpendicular directions along the

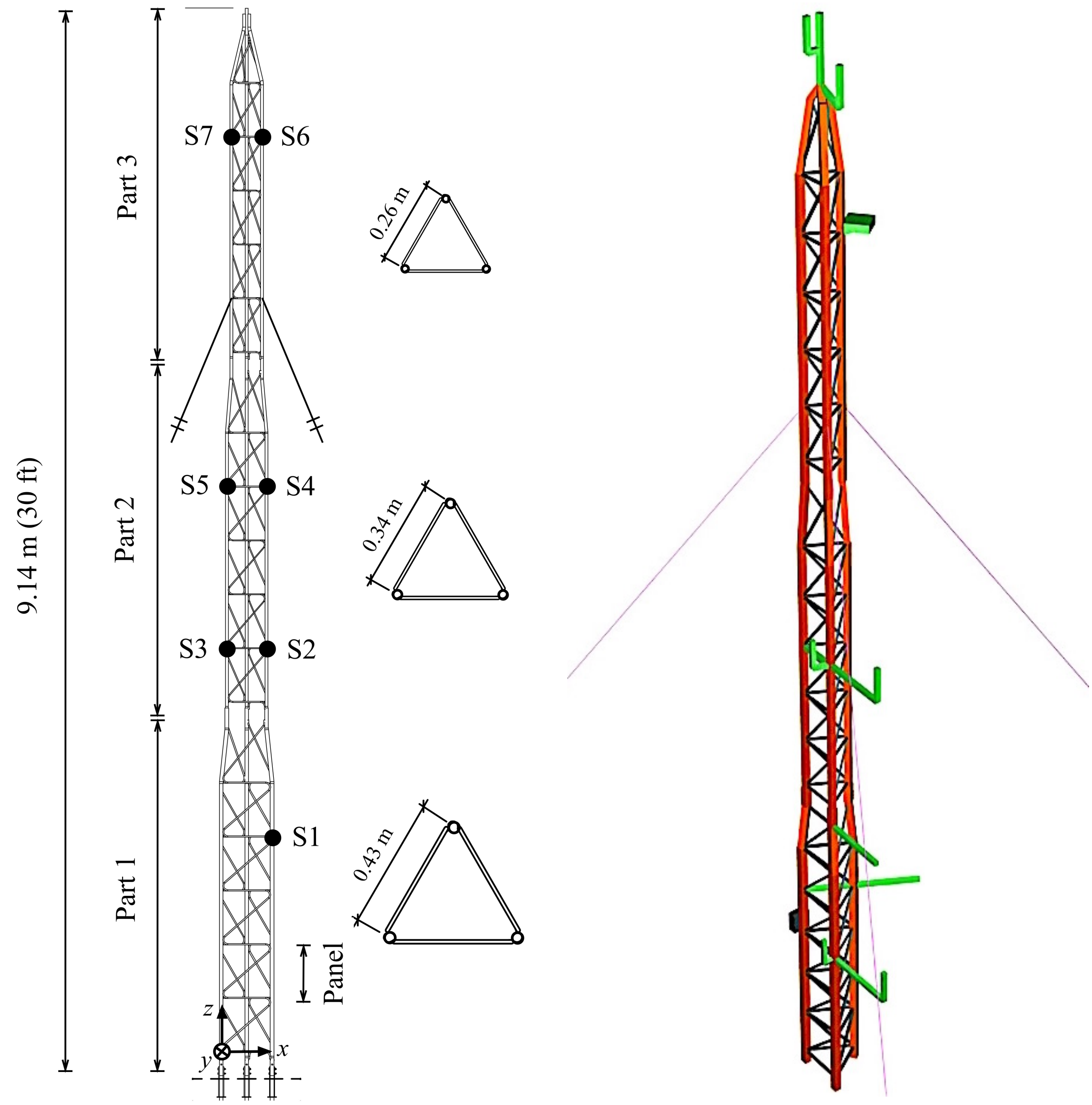

(a) Side view of the mast structure and response sensor locations

(b) Picture of the FE model of the instrumented guyed mast

Figure 3.1: The representation of the mast structure and the sensor configuration details

Table 3.1: The first eight natural frequencies and damping ratios of the structure

Mode	1	2	3	4	5	6	7	8
Eigenfrequency (Hz)	3.031	3.227	3.337	5.5240	5.685	6.065	8.246	8.816
Damping ratio (%)	1.00	1.00	1.00	1.16	1.18	1.22	1.51	1.63

mast. In order to generate the fluctuating wind pressure, the fluctuating wind speed along the mast was simulated as an 18-variate single dimensional stationary random process, independently in each direction. By this, the attack angle can also randomly change, since just the fluctuating part of wind load is going to be identified. According to Davenport concept (*Davenport* (1961b)), the quadratic fluctuating part of wind load can be neglected (*Simiu and Scanlan* (1978); *Holmes* (2007)), then the linear fluctuating wind load can be generated as a function of time t and height z, as follows:

$$f_w(t,z)_{x,y} = \rho A(z) C_d \bar{V}_{10} \left(\frac{z}{10}\right)^{\alpha} V(t)_{x,y} \tag{3.11}$$

where ρ, $A(z)$, C_d and $\bar{V}_{10}$ denote respectively the air density, the mast element exposed area, drag coefficient and the mean wind speed at 10 m height as well as the fluctuating wind speed, $V(t)_{x,y}$, which is to be simulated according to section 3.3.2. The law exponent, α, depends on the roughness length.

The resulted wind load is applied as tributary nodal forces along the structure, which correspond to the elements area of each mast panel. The 10 m height mean wind speed was taken equal to 10 m/s^{-1} and frequency upper-bound of the wind speed spectrum was set to 7 Hz that covers the first six vibration modes, thus the sampling rate for fluctuating wind speed simulation was taken equal to 14 s^{-1}. The displacement and acceleration responses were obtained from an almost evenly distributed configuration of the virtual sensors along the mast at seven sensor locations as marked by $[S1 : S7]$ in Fig 3.1a. While at locations $[S1\ S3\ S5\ S7]$ the response in two horizontal directions was measured, at the rest of the locations the response was additionally obtained just in one direction.
The noise-polluted response is then computed according the following definition at location i:

$$U_{Si_{noisy}} = U_{Si} + n_{lev} * \sigma_i * W_n \tag{3.12}$$

where U_{Si} denotes the measured response, whose standard deviation is σ_i. The artificial noise, W_n, is generated by means of white noise Gaussian signal rescaled to have values between $[-1 : 1]$, while the noise magnitude is controlled by the noise level n_{lev}.

3.3.2 Correlated fluctuating wind speeds simulation

The fluctuating wind speeds are digitally simulated in two perpendicular horizontal x-y directions (see Fig. 3.1a). The fluctuating wind speeds in each horizontal direction are correlated with respect to the height of the location on the structure. It is assumed that the correlated wind speeds in each horizontal direction belong to an independent zero mean stationary processes. The correlated fluctuating wind speeds were digitally simulated in each horizontal direction at 18 different heights, which pertain to 18 panels of the guyed mast as depicted in Fig. 3.1a . To begin the wind speeds simulation the power spectral density (PSD) matrix, $\mathbf{S}_v(\omega)$, with regard to the wind speeds at different locations is firstly required:

$$\mathbf{S}_V = \begin{bmatrix} S_{V_1V_1} & S_{V_1V_2} & \dots & S_{V_1V_m} \\ S_{V_2V_1} & S_{V_2V_2} & \dots & S_{V_2V_m} \\ \vdots & \vdots & \dots & \vdots \\ S_{V_mV_1} & S_{V_mV_2} & \dots & S_{V_mV_m} \end{bmatrix} \tag{3.13}$$

where $m = 18$ denotes the number of random process variates and $S_{V_pV_p}$ and $S_{V_pV_q}$ (i.e. the diagonal and off-diagonal components of PSD matrix) are calculated from auto- and cross spectral density functions respectively. Several different spectral density functions are available from literature (*Davenport* (1961a); *Kaimal et al.* (1998)), among which Solari's spectrum (*Solari* (1993)) has been chosen in this study:

$$S_{VV} = \frac{6.868\,\sigma_v^2\, f\, L_v/z_p}{(\omega/2\pi)\,[1+10.302\, f\, L_v/z_p]^{5/3}} \tag{3.14}$$

where σ_v^2, L_v and z_p denote the variance of fluctuating longitudinal component of the wind speed, the integral length scale of turbulence and the vertical distance from the ground. Moreover the Monin coordinate $f(z_p,\omega) = \omega\, z_p/2\pi\bar{V}\,(z_p)$ is dependent on $\bar{V}\,(z_p)$, i.e. the mean wind speed at a certain height. Then the off-diagonal components of PSD matrix can be obtained from the cross spectral density function according to (*Vickery* (1971); *Davenport* (1967)) at different heights z_p and z_q

$$S_{V_pV_q} = \sqrt{S_{V_pV_p} S_{V_qV_q}}\, exp\left[-C_z\,\frac{\omega}{\pi}\,\frac{|z_p - z_q|}{\bar{V}_p+\bar{V}_q}\right] \tag{3.15}$$

in which the real-valued exponential term, so-called $vertical\ coherence\ function$, which depends on the wind speed component frequency, accounts for the correlation of the wind speeds at heights z_p and z_q. According to *Simiu and Scanlan* (1978); *Kristensen and Jansen* (1979), C_z can be set equal to 10 for structural design purposes and $\bar{V}_p$ and $\bar{V}_q$ are mean wind speeds at given heights.

Afterwards the samples of a stationary random process with a given PSD can be generated according to (*Papoulis* (1984)):

$$\mathbf{V}(t) = \int_{-\infty}^{\infty} \sqrt{S_{VV}\,(\omega)}\, e^{i\,\omega t}\, \mathrm{d}\mathbf{B}(\omega) \tag{3.16}$$

where $\mathbf{B}(\omega)$ collects m rows of complex random processes. The above integral is usually evaluated numerically, then $\mathrm{d}\mathbf{B}(\omega)$ is replaced by its discretized form $\mathbf{b}(\omega) = \sqrt{\Delta\omega}\,(\mathbf{a}+i\mathbf{d})$, which is the function of m-row zero mean Gaussian random matrices i.e. $\mathbf{a}$ and $\mathbf{d}$ with unit variance.

At this stage one has to decompose the PSD matrix in order to apply the correlation between components of the wind speed at different heights. One method is using Cholesky decomposition of the PSD matrix (*Deodatis* (1996)). Another option that also brings a physical insight, is taking advantage of the analogy between representation of the wind velocity stochastic process and the random fields (*Bucher* (2009a)) by means of $spectral\ decomposition$ of the PSD matrix (*Di Paola and Gullo* (2001); *Di Paola* (1998)):

$$\mathbf{S}_V = \sum_{k=1}^{n} \psi_k(\omega)\, \psi_k(\omega)^T\, \Lambda_k(\omega) \tag{3.17}$$

provided that these orthogonality condition exists:

$$\begin{aligned} \boldsymbol{\psi}(\omega)^T\, \boldsymbol{\psi}(\omega) &= \mathbf{I} \\ \boldsymbol{\psi}(\omega)^T\, \mathbf{S}_V\, \boldsymbol{\psi}(\omega) &= \mathrm{diag}\,(\Lambda_k\,(\omega)) \end{aligned} \tag{3.18}$$

where k is the number of the frequency-dependent eigenvectors/values of the PSD matrix and $\boldsymbol{\psi}_k(\omega)$ is the matrix collecting the eigenvectors. The diagonal matrix $\Lambda_k(\omega)$ includes the eigenvalues belonging to the PSD matrix $\mathbf{S}_V(\omega)$ at each frequency.

As a result by virtue of Eqs.3.17 and 3.18 the integral in Eq. 3.16 can be numerically evaluated by means of a two sided inverse discrete Fourier transform of size N, in order to generate the fluctuating wind speed at different hights:

$$\mathbf{V}(t) = \sum_{j=-N}^{N} \left(\sum_{k=1}^{m} \psi_k(\omega_j)\, \sqrt{\Lambda_k(\omega)}\, b_{kj} \right) e^{i\,\omega_j t} = \sum_{k=1}^{m} \left(\sum_{j=-N}^{N} \psi_k(\omega_j)\, \sqrt{\Lambda_k(\omega)}\, b_{jk}\, e^{i\,\omega_j t} \right) \tag{3.19}$$

Given the substitution $\mathbf{H}(\omega_j) = \sum_{k=1}^{m} \psi_k(\omega_j)\, c_k(\omega)$ with $c_k(\omega) = \sqrt{\Lambda_k(\omega)}\, b_{kj}$, it implies that $\mathbf{H}(\omega)$, which is the Fourier transform of the correlated wind speeds with power spectral density matrix $\mathbf{S}_V$, is analogous to a random filed. It can be deduced from the equality in Eq. 3.19, that the correlated random wind speed components may be simulated in two equivalent ways. According to left-hand side of Eq. 3.19, one way is to generate *N* pairs of *m* random variable corresponding to each height, while the other possibility is the generation of *m*-pair random variables along the frequency band.

Figs. 3.2a and 3.2c represent the time history of a simulated fluctuating wind speed at the lowest and highest panels of the mast, respectively. The validity of the generated wind speed was investigated by the comparison between the simulated wind speed and Solari's power spectrum at those heights in Fig. 3.2b and 3.2c, which shows good agreement between analytical and simulation power spectrum.

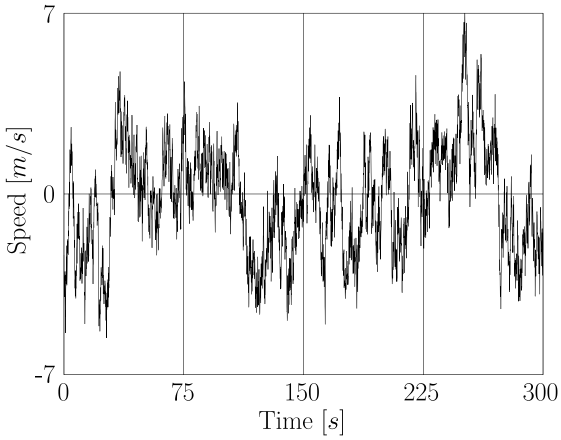

(a)

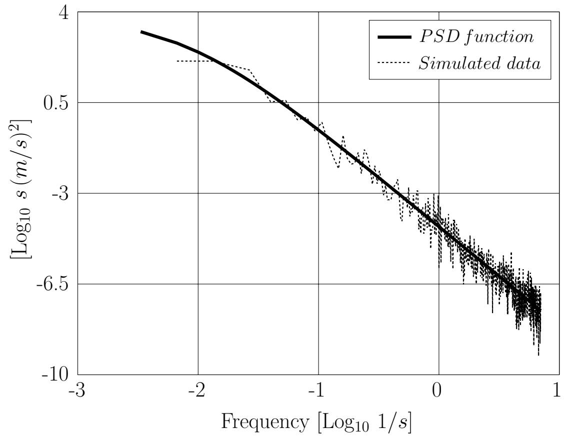

(b)

The lowest mast panel

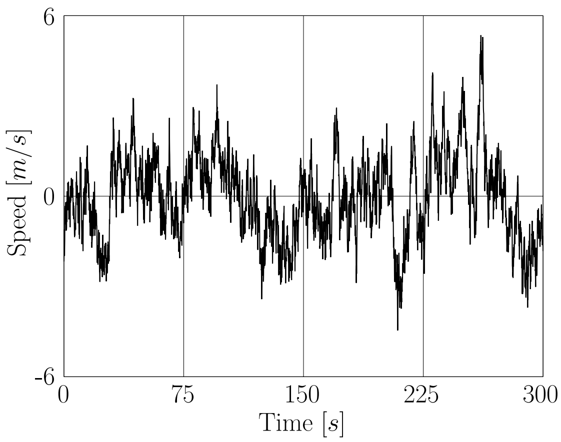

(c)

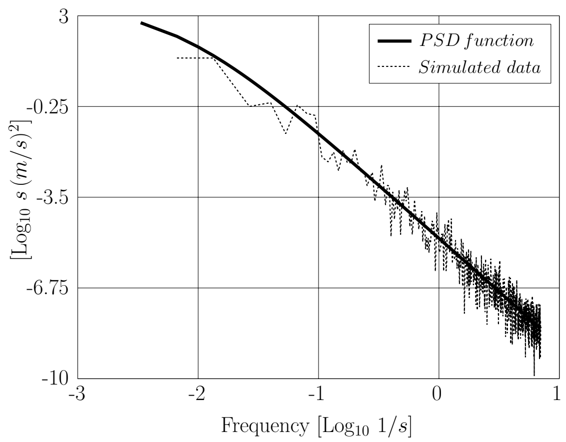

(d)

The highest mast panel

Figure 3.2: The samples of simulated wind speeds: Wind speed time history and the corresponding power spectra

3.3.3 Decomposed modal responses

The modal responses were derived according to the mode shape data and the responses at the sensor locations. For this purpose the measured responses were decomposed by Eq. 4.2 for the first six modes, which are contained in the excitation frequency range.

The validity of the decomposed modal responses can be examined by the modal response spectrum plot, in which there must exist only one dominant vibration frequency pertaining to the natural frequency of system in that mode. As such the Welch spectra of the decomposed modal responses of excited modes were plotted to check this criterion. In Figs. 3.3 the power spectrum of the displacement and acceleration response is represented respectively. The power spectra in Figs. 3.3a and 3.3c shows that firstly the spectrum plot at each mode has just one dominant peak. If for instance the displacement and acceleration responses were decomposed just into the first three modes, a spurious peak belonging to higher modes (4th or 5th) appears in the power spectrum of the first three modes (*see Figs.* 3.3*b and* 3.3*d*). This is why as mentioned earlier the contribution of all modes within the existing frequency range must be decomposed.

Overall the signal power of the displacement-based modal responses is much stronger in lower than in higher frequencies compared to the acceleration-based modal responses (proportional to the square of the circular frequencies). As a result one can anticipate, the recovery of the lower frequency components of the load signal can be accomplished from the modal displacement responses better than that of acceleration.

3.3.4 Results of the reconstructed modal wind loads

In order to evaluate the introduced method's capability, the wind load identification was performed based on the decomposed measured displacement and acceleration responses. The results pertaining to the first five modes were provided in terms of the comparison between the time histories of the identified and actual modal wind loads as well as their corresponding power spectra. The corresponding results of the sixth mode was discarded, because that mode was not sufficiently excited.

In Figs. 3.4 and 3.5 respectively the reconstructed wind load time history from displacement and acceleration response with $n_{lev} = \{5\%, 10\%, 15\%\}$ for the first vibration mode were plotted together with their power spectra.

The detailed results analysis pertaining to the measured displacement and acceleration responses are presented in Tables 3.2 and 3.3. For observing the effect of the noise magnitude on the reconstructed loads, the modal wind loads were reconstructed from responses with different noise levels, n_{lev}. In those tables the $coefficient\ of\ correlation$, $0 \leq \rho_c \leq 1$, represents the degree of trend similarity between the identified and actual wind loads at each mode, where the closer values of ρ_c to one yields the more linear correlation between the actual and identification results and vice versa (*Clough and Penzien* (1995)). On the other hand by means of the *relative error* index i.e. R_e defined in Eq. 3.20, it is possible to find out that the identified load of which measured response type, i.e. displacement or acceleration, is more sensitive to the rise in noise magnitude contained in the measurement data.

$$R_e(\%) = \left|\left|\tilde{\mathbf{P}}_i - \mathbf{P}_i\right|\right| / ||\mathbf{P}_i|| * 100 \tag{3.20}$$

In Eq. 3.20, $\tilde{\mathbf{P}}_i$ and $\mathbf{P}_i$ stand for identified and actual modal wind loads. As illustrated in Figs. 3.4 and 3.5, first of all the displacement-based reconstructed modal wind loads have higher accuracy at the same noise level compared to their acceleration-based counterparts. However the increase of the noise level reduces the quality of the load identification of both of them, which can be also perceived from the R_e values in Tables 3.2 and 3.3. Furthermore the GCV method, especially based on the acceleration response,

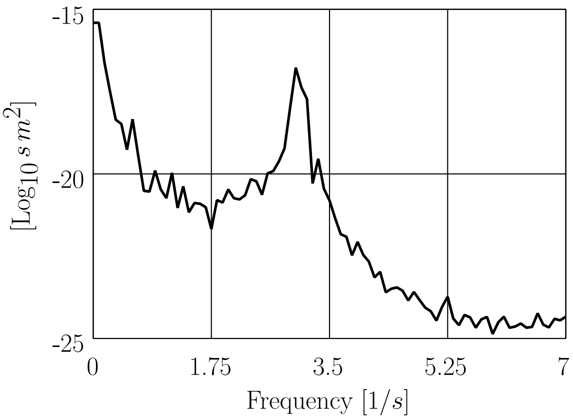

(a) Correctly decomposed displacement response

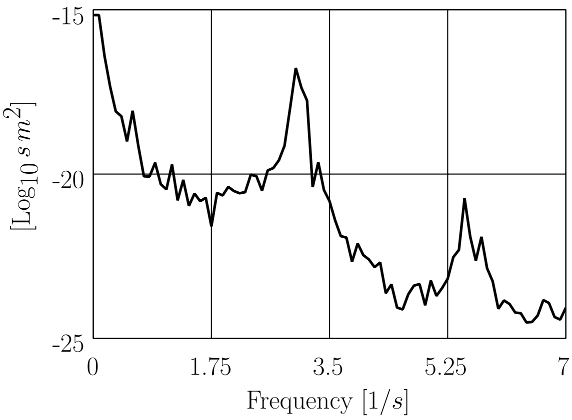

(b) Incorrectly decomposed displacement response with spurious peak

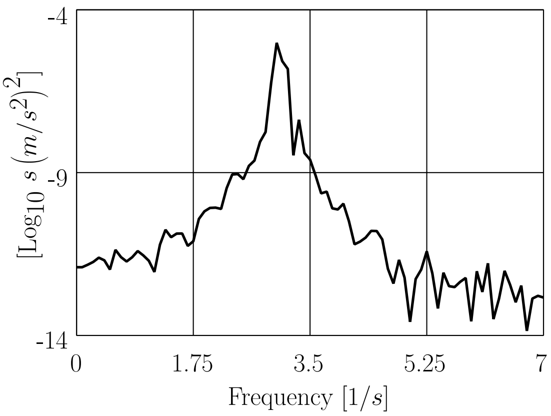

(c) Correctly decomposed acceleration response

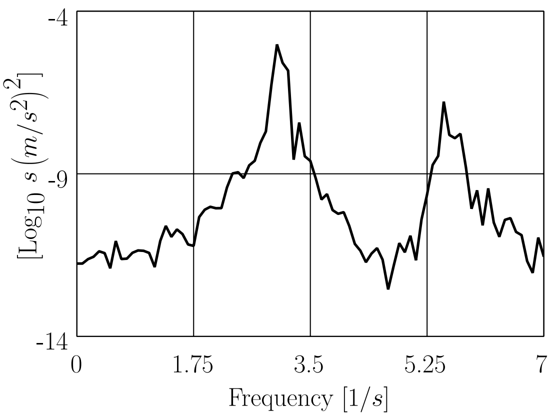

(d) Incorrectly decomposed acceleration response with spurious peak

Figure 3.3: The decomposed modal responses corresponding to the first vibration mode

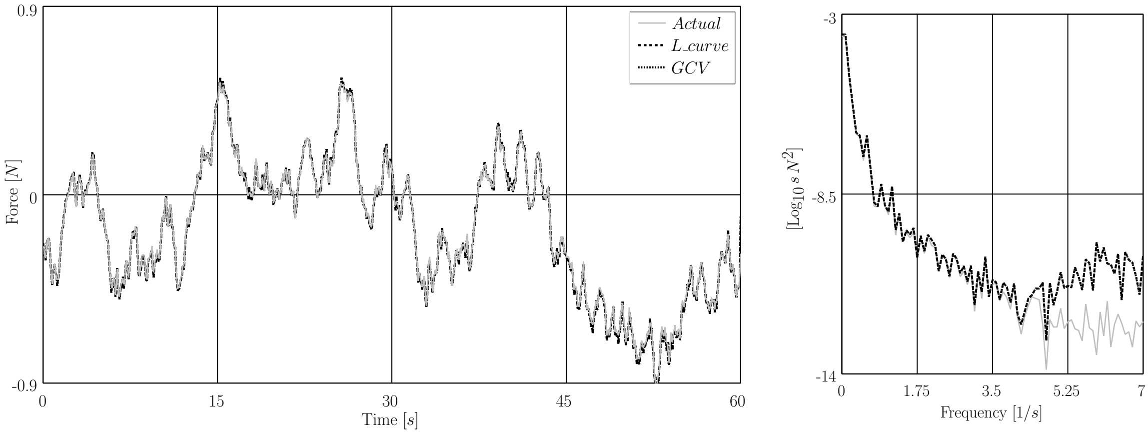

Noise level: $n_{lev} = 5\%$

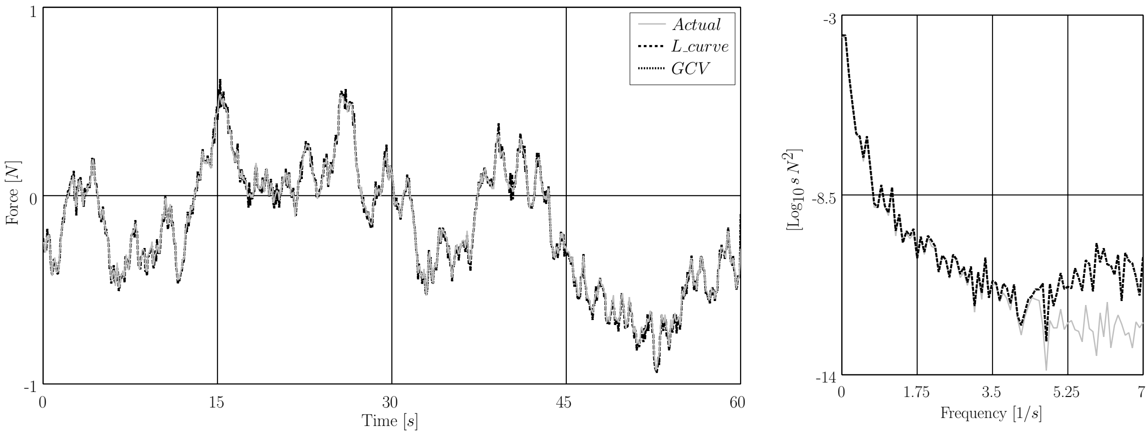

Noise level: $n_{lev} = 10\%$

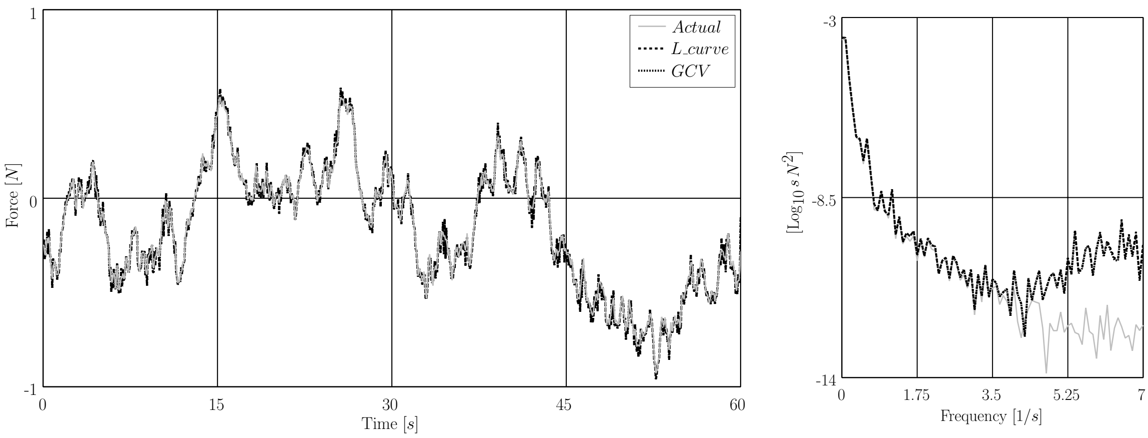

Noise level: $n_{lev} = 15\%$

Figure 3.4: Time history and power spectrum of the reconstructed first mode wind load from displacement response

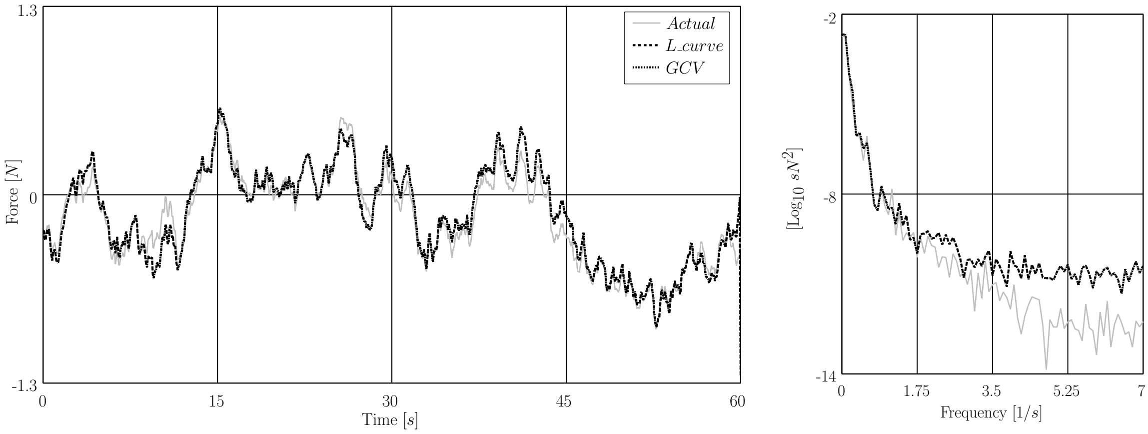

Noise level: $n_{lev} = 5\%$

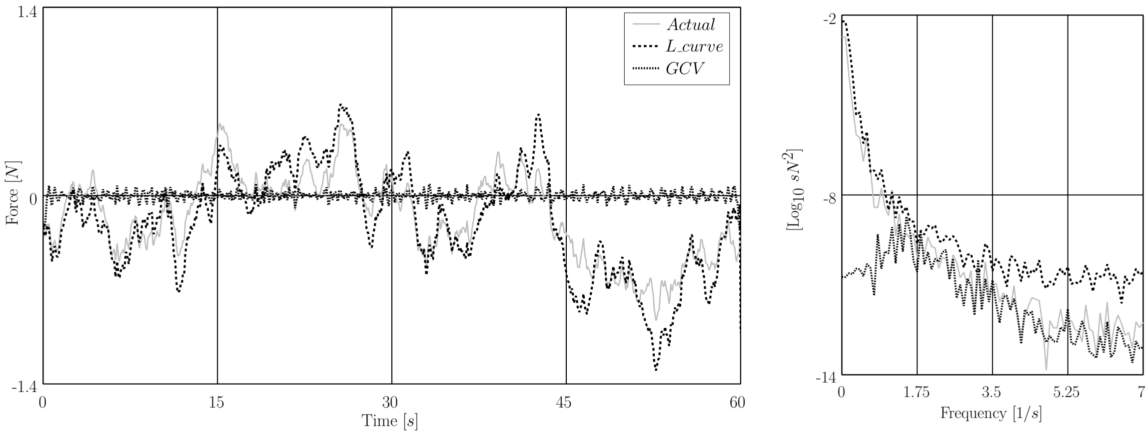

Noise level: $n_{lev} = 10\%$

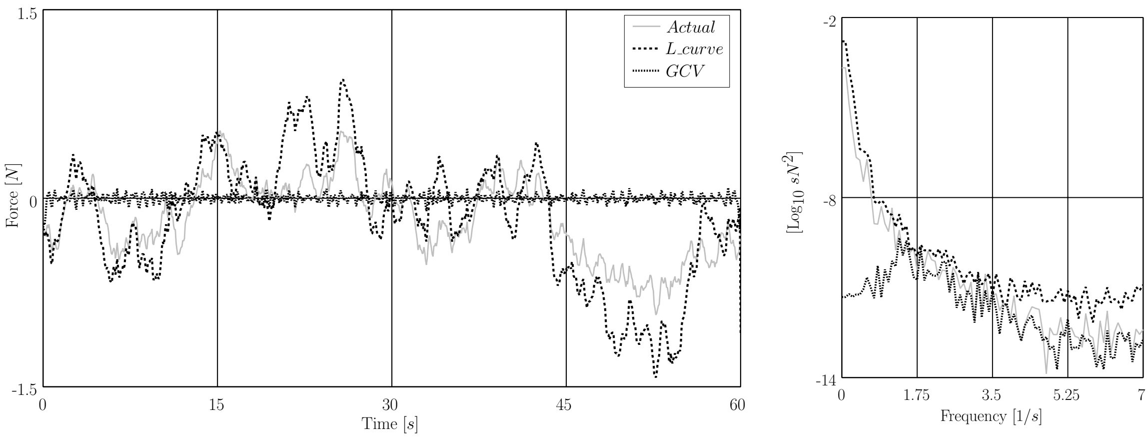

Noise level: $n_{lev} = 15\%$

Figure 3.5: Time history and power spectrum of the reconstructed first mode wind load from acceleration response

Table 3.2: Result analysis associated with the reconstructed modal wind loads from displacement response
ρ_c: Coefficient of correlation and R_e: Relative error (%)

Mode		$n_{lev} = 5\%$		$n_{lev} = 10\%$		$n_{lev} = 15\%$	
		L-curve	GCV	L-curve	GCV	L-curve	GCV
1st	ρ_c	0.9999	0.9990	0.9973	0.9974	0.9945	0.9949
	R_e	4.5	4.4	7.0	6.9	9.8	9.4
2nd	ρ_c	0.9993	0.9993	0.9988	0.9986	0.9976	0.9977
	R_e	3.6	3.6	4.8	4.8	6.8	6.8
3rd	ρ_c	0.9996	0.9997	0.9994	0.994	0.9988	0.9986
	R_e	2.5	2.5	3.1	61	4.4	4.4
4rth	ρ_c	0.9884	$-^*$	0.9810	$-^*$	0.9696	$-^*$
	R_e	18	$-^*$	20.1	$-^*$	24.1	$-^*$
5th	ρ_c	0.9831	0.9831	0.9799	0.9799	0.9776	0.9776
	R_e	27.6	27.6	29.5	29.5	29.7	29.7

* GCV failure in finding the optimal regularizion parameter

is indeed likely to fail in providing a proper regularization parameter, which is demanded for solving the Tikhonov inverse problem. Several runs of the load identification procedure confirm this statement, that is also observable as an example in Fig. 3.5 with with $n_{lev} = \{10\%, 15\%\}$. Consequently those results were not given in Table 3.3. The same occurred in some cases when the displacement response was utilized, which are marked by (*) in Table 3.2. Contrarily, L-curve usually located the the Tikhonov parameter correctly although the quality of its corresponding solution, depending on the measured response type or noise level, can vary.

Table 3.3: Result analysis associated with the reconstructed modal wind loads from acceleration response
ρ_c: Coefficient of correlation and R_e: Relative error (%)

Mode		$n_{lev} = 5\%$	$n_{lev} = 10\%$	$n_{lev} = 15\%$
		L-curve	L-curve	L-curve
1st	ρ_c	0.94	0.91	0.79
	R_e	31	47	58
2nd	ρ_c	0.97	0.95	0.87
	R_e	23	35	53
3rd	ρ_c	0.99	0.97	0.93
	R_e	16	26	35
4rth	ρ_c	0.94	0.81	0.68
	R_e	33	62	99
5th	ρ_c	0.98	0.91	0.8
	R_e	19	41	61

A great importance is attached to the point that the quality of displacement-based identified modal wind loads are less sensitive to the noise levels magnitude at different modes, that makes it more attractive and superior over acceleration-based wind load reconstruction. A closer attention was drawn to the comparison between the properties of the impulse response matrices (IRM) of the displacement and acceleration responses. Above all, the *condition number* (*Cheney and Kincaid* (2008); *Trefethen and*

Bau III (1997)), which is the ratio between the largest to the smallest singular values of a matrix, implies that how much the inverse solutions of the system of linear equations like in Eqs. 3.4 are sensitive to the perturbation or in other words to the non-system-generated components (noise).

In Fig. 3.6 the singular values of the displacement and acceleration augmented IRMs for the first vibration mode were demonstrated, which represent a gradual decay of the singular values due to the ill-conditioning of IRM. The smallest singular value of displacement IRM is approximately zero due to the zero initial conditions assumption. This assumption was also considered in derivation of the acceleration IRM, because usually during the data acquisition of the ambient vibration measurements, the initial conditions can not be readily determined, which is due to the fact that it would require to mount different types of response sensors (velocity, displacement) on the structure simultaneously, that is not normally of high interest in field measurement. Moreover the transient response, namely the contribution of the initial conditions in the vibration response of the civil engineering structures is insignificant as a result of damping. This contribution is negligible especially for the wind-induced vibrations, where the measurement time-length is relatively long of the order of minutes. Consequently for the sake of a clearer comparison, the condition numbers of the modal displacement and acceleration IRMs are presented in Table 3.4, ommiting the smallest singular value, which is less than the computer precision. This table also shows the condition number of the IRMs with 8400 time steps corresponding to 10 *min* response, in addition to the IRMs used in this study with 840 time steps (1 *min* response).

Given the condition numbers in Table 3.4, it was revealed that for the same structural system the condition numbers of the modal acceleration IRMs are considerably greater than those of the displacement IRMs. Moreover the condition number of acceleration IRM rises with a higher rate than that of displacement with the growth of problem size. Hence it is expected that the wind load reconstruction based on the measured acceleration response is more sensitive to noise and consequently less accurate. According to Table 3.4, from the relatively small condition number of displacement IRM, it can be also perceived that the introduced procedure is able to effectively relieve the existing ill-posedness, as reported in the literature pertaining to load identification. This is accomplished by implementing the wind load reconstruction in modal subspace through the modal displacement IRMs. Due to this fact, the load reconstruction remains highly accurate in wind load applications even for longer time-length and consequently this point is a remarkable strength of the introduced procedure in this study.

The displacement-based reconstructed modal wind loads have sufficient accuracy even for relatively high noise levels. In the frequency domain this good quality remains intact up until the corresponding mode's vibration frequency and afterwards deviates with an intensity depending on the noise level. Thus, unlike the acceleration-based case, this give rise to the identified loads with the correct background signals, composed of the lower frequency components at each mode (*see power spectra in Fig.* 3.4), what is indeed of high interest in wind induced vibration application.

Table 3.4: The condition numbers of the modal impulse response matrices

Mode		1	2	3	4	5	6
Displacement	1 *min*	226	190	172	24	23	20
	10 *min*	233	195	176	24	23	21
Acceleration	1 *min*	12538	10938	10136	2316	2083	1620
	10 *min*	12954	11259	10413	2334	2097	1629

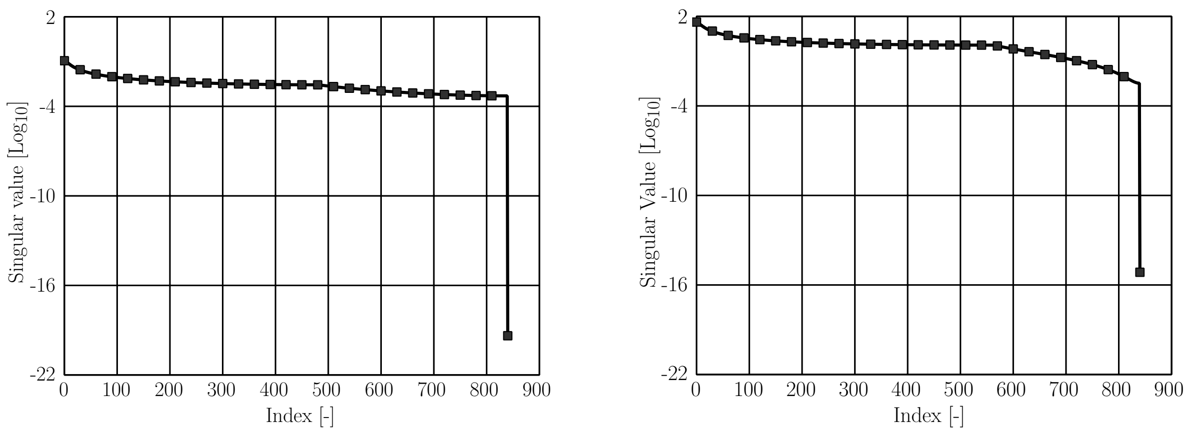

(a) Displacement

(b) Acceleration

Figure 3.6: Singular values of impulse responses matrices for the first mode

3.4 Conclusion

In this contribution a procedure for the inverse wind load reconstruction from measured structural responses of the large degrees of freedom structures was introduced. It was tried to keep the procedure practically applicable and solely based on the data that can be obtained via vibration response measurements, so that extra assumptions for unmeasured degrees of freedom responses or mass and stiffness matrix setup are not required. But instead just the modal properties of the structural system, which can be obtained directly from the vibration measurements are demanded, in order to generate the augmented impulse response matrix of the system and decompose the measured responses into the modal responses. The presented step-by-step procedure with a fairly comprehensive discussion explains different aspects of the provided wind load identification method for the real applications.

An important goal of the study concerns revealing the more consistent response type, i.e. displacement or acceleration, for the wind load recovery according to the provided procedure. It was found out that the measured displacement response is more appropriate for this purpose, due to the higher power of displacement signal in lower frequencies and the smaller condition numbers of the modal displacement impulse response matrix compared to those of the modal acceleration, which consequently makes the inverse problem less sensitive to the contained noise in the displacement data acquired from measurement setup.

The quality of the reconstructed modal wind loads based on both response types reduces as the noise level increases. But rather the modal wind load identification from the displacement response, especially by means of the L-curve method, remains sufficiently accurate even at 15% noise level. The background signal of wind load is correctly reconstructed from displacement response whereas the noise-related discrepancy emerges in the high frequency components of the identified load signal above the natural frequency of the corresponding mode.

Consequently according to the introduced procedure in this study, the modal wind loads can be recovered from the measured displacement response properly, without bearing substantial accuracy drop even in the presence of relatively high amount of noise in the measured signal for relatively long time-lengths.

Chapter 4

Identification of wind loads from structural responses through full-scale field measurements

This paper presents the field application of an introduced procedure for the wind load identification. The wind loads are inversely reconstructed in time domain by means of an augmented impulse response matrix from measured structural response. The inherent noise amplification arising from ill-posed inverse problem is resolved through Tikhonov regularization scheme. In order to increase the accuracy in solving the inverse problem along with the availability of the measured response just at a limited number of sensor locations, the problem is projected onto the modal coordinates. Consequently the modal wind loads are identified in modal subspace for several single degree of freedom systems, whose characteristic parameters are obtained by an operational operational modal analysis procedure. The structure under measurement is a 9.1 m (30 ft) tall guyed mast. Since the direct wind pressure/load measurements on the structural members are almost impossible in full-scale testing, numerical simulation was also implemented to verify the experimental results by analogy. The load identification results are provided in time and frequency domain. Numerical simulations, where actual loads are available, confirm the capability of the method in identification of modal wind loads. Then based on the existing analogy, the identified loads from field measurements are validated.

4.1 Introduction

Inverse identification of dynamic loads is a common problem in different fields of engineering like in engine-induced vibrations of vehicle chassis (*Hebruggen et al.* (2002); *Leclèrea et al.* (2005)), moving loads on bridges (*Zhu and Law* (2002); *Lee* (2014); *Law and Zhu* (2011)) or in wind-induced vibration of structures (*Kazemi-Amiri and Bucher* (2014); *Chen and Lee* (2008)). The load identification problem is generally an example of the inverse problems with application to structural dynamics and vibrations. Dynamic load identification becomes more appealing in the cases, where the excitation factor can not be directly observed through measurements. This could be due to either the nature of excitement cause or the restrictions of man-made apparatus. The dynamic wind load, as a consequence of the wind pressure with the continuous distribution on the structural elements, is a good example in this regard. Engineers can obtain plenty of advantages, if good knowledge on dynamic loads are available. Those advantages can be outlined from the design phase e.g. improvement of the loading codes of practice up to the post-analysis phase for instance in structural performance improvement or health monitoring of the in-service structures.

Design codes of practice for wind load provide useful information, most of which derived from wind tunnel test data (*Holmes* (2007); *Simiu and Scanlan* (1978)). However laboratory assisted simulation of a complex phenomenon like wind in wind tunnel, which is influenced by several parameters is prone to uncertainties. Therefore the information obtained by wind load identification from the field measurement data can be beneficial to verify the wind tunnel test data, as well. Identified wind load data can be also utilized for a realistic reliability and risk assessment of in-service structures, whereas usually numerical simulations are available for that purpose (*Bucher* (2009a); *Augusti et al.* (1984)).

A couple of studies in the area of load recovery from response measurements have recently dealt with the problem of wind load identification. However yet the number of those studies is not significant in comparison with the number of researches, generally conducted in structural dynamic load identification area. Hence there is a tangible need for more researches particularly on the wind load related issues from different aspects. The studies on the wind load reconstruction may be categorized with respect to the way they treat the input identification problem. For example *Law et al.* (2005) solves the problem, despite the insufficient number of measured point on the structure, in the physical domain in which measurement has been carried out. According to *Law et al.* (2005), the iterative simulations of wind speeds based on the identified wind characteristics of the structure's site, play an important role in order for wind load identification in physical subspace to provide structural response data for unmeasured points. Another approach is to transform the problem into another subspace (e.g. modal subspace) to truncate the unknowns to the number of equations, available from the measurement at sensor locations. *Hwang et al.* (2011) is an example of the latter, where the modal wind loads were recovered within the use of Kalman filtering scheme for state estimation of system. Nonetheless this approach does not directly tackle the noise magnification problem and instead suggests to additionally apply low-pass filter on the measurement data to remove noise in relatively higher frequencies. Here having a good knowledge on the noise properties is inevitable in order to set the cutoff frequency and filter type, which is usually out of reach due to different and variable noise sources. In *Lourens et al.* (2012) an augmented Kalman filter was introduced, trying to identify the load as input signal, while simultaneously tries to relieve the noise effect. However in that study it was demonstrated that still the Tikhonov type solutions are more robust in different situations. Recently *Azam et al.* (2015b) stated that by an expert guess on the covariance of the input and through a proposed dual Kalman filter, the drift effect in the estimated input load via implementing the augmented Kalman filter can be avoided. However the two latter studies have not been specialized for the inverse estimation of wind loads yet.

With respect to the above-mentioned points, in this contribution an approach for wind load identification is adopted, when the following conditions hold: *a*) Additional data or information on the wind characteristics of structure's site, acting wind load or noise nature is unavailable. *b*) Structural response just on a limited number of points can be measured. *c*) The noise effect within solving the inverse problem should be resolved. *d*) Only structural modal characteristics (Natural frequencies, mode shapes and damping ratios) through a system identification method and accordingly modal analysis are available.

Application of this procedure requires only the response data derived from the field measurement, for the structure undergoing wind vibration. The impulse response matrix, necessary to construct the input-output (dynamic load-response) relation, is generated based on a previous work of the authors (*Kazemi-Amiri and Bucher* (2015)) and the strength of the introduced procedure was investigated for inverse estimation of wind loads on large degrees of freedom structures based on numerical simulation (Chapter 3). The structure under study in this contribution is a 9.1 m (30 ft) tall guyed mast with tubular elements, which is serving as a weather station tower in the Hydrological Open Air Laboratory

Petzenkirchen, Lower Austria (*Blöschl et al.* (2016)). The operational modal analysis results of the structure is provided in section (4.3.2). The characteristics of the reconstructed modal wind loads have been inspected in time and frequency domain. As a matter of fact it is not feasible to measure the actual wind load in the field testing tasks. Consequently in order to verify the estimated experimental results, the numerical simulation of the same problem was implemented, which is assisted by the finite element model of the mast structure and digital simulation of the wind speed. The simulation results are studied in section 4.4. The analogy between the numerical simulation and practical field application results provides useful information on how to verify the correctly identified modal wind loads, which is discussed in section 4.4.1. According to the existing analogy it is concluded that the in-situ modal wind loads can be identified by applying the introduced procedure.

4.2 Wind load reconstruction procedure

It is briefly explained the wind load identification procedure within this section. Since this contribution is intended to more focus on the practical application of the proposed method and its corresponding details, thus the readers are referred to Chapter 3 for more information on the applied procedure itself.

Consider the equation of motion of a linear multiple degrees of freedom structure with mass $\mathbf{m}$, stiffness $\mathbf{k}$ and the classical damping $\mathbf{c}$ matrices. Those equations are decoupled into set of one degree of freedom systems in modal coordinates by the substitutions $\mathbf{u}(t) = \mathbf{\Phi}\mathbf{q}(t)$, in which $\mathbf{\Phi}$ is the matrices, collecting the mode shapes. Then premultiplication by $\mathbf{\Phi}^T$ (*Ziegler* (1998); *Chopra* (1995)) renders:

$$\mathbf{m}\ddot{\mathbf{u}} + \mathbf{c}\dot{\mathbf{u}} + \mathbf{k}\mathbf{u} = \mathbf{p}(t) \tag{4.1a}$$

$$\ddot{\mathbf{q}} + 2\ diag[\zeta_i \omega_i]\ \dot{\mathbf{q}} + diag[\omega_i^2]\ \mathbf{q} = \mathbf{P}(t) \tag{4.1b}$$

where $\mathbf{P} = \mathbf{\Phi}^T\mathbf{p}$ and ζ_i, ω_i denote the damping ratio and natural circular frequency at i^{th} mode respectively. Then the steps of the introduced procedure for wind load reconstruction are as follows:

1. Identify the structural modal parameters i.e. ω_i, $\mathbf{\Phi}_r$ and ζ_i.

   For this study those parameters were gained by means of an operational system identification. Hereafter the subscript r refers to the reduced set of identified mode shapes or measured response vectors, since those are just available at the sensor locations.
2. Decompose the measured responses acquired from different sensor channels mounted on the structure by means of the following equation:

   $$\tilde{\mathbf{q}}(t) = \mathbf{\Phi}_r^{\dagger}\mathbf{u}_r(t) \tag{4.2}$$

   in which $\mathbf{\Phi}^{\dagger} = \left[\mathbf{\Phi}_r^T\,\mathbf{\Phi}_r\right]^{-1}\mathbf{\Phi}_r^T$ and $\tilde{\mathbf{q}}(t)$ denote the pseudo inverse of the incomplete mode shapes matrix and the approximated modal response matrix, respectively.
3. Check the validity of the decomposed modal responses by means of its power spectrum or simply its Fourier transform; Such that each modal response must only have one dominant vibration frequency corresponding to the natural frequency of the system at that mode.

   To this end the contribution of all modes within the existing frequency range must be decomposed.
4. Given the modal parameters for a number of vibration modes, the modal impulse response matrix (IRM) of the system $\left[\bar{\mathbf{h}}_{d_i}\right]$ is generated for each mode (*Kazemi-Amiri and Bucher* (2015)).

The IRM together with the decomposed modal responses from step 2 are utilized to set up the input-output relation for the inverse identification of the acting modal wind load, that is $\mathbf{P}_i$, in the relation below:

$$\{\mathbf{q}_i\} = \left[\bar{\mathbf{h}}_{d_i}\right]\{\mathbf{P}_i\} \tag{4.3}$$

While l is equal to the total number of time steps, then $\left[\bar{\mathbf{h}}_{d_i}\right] \in \mathbb{R}^{l*l}$ stands for the modal displacement impulse response matrix at the ith mode, wherein $\bar{\mathbf{h}}_{d_i}$ is derived based on the displacement impulse response function $h_i(t) = \frac{e^{-\zeta_i \omega_i t}}{M_i \omega_{d_i}} sin\omega_{d_i} t$ for each mode (*Kazemi-Amiri and Bucher* (2015)).

5. Since Eq. 4.3 is derived by the Duhamel's integral (convolution), which is classified in the family of Fredholm integral equation of the first kind, matrix $\left[\bar{\mathbf{h}}_{d_i}\right]$ is ill-conditioned and consequently this equation can not be solved directly to find the estimated applied wind load $\tilde{\mathbf{P}}_i$ (*Jankowski* (2013); *Tikhonov and Arsenin* (1997)). Alternatively it is benefited from the Tikhonov regularization scheme in order to identify the modal wind loads (*Tikhonov and Arsenin* (1997)):

$$min\left\{\left|\left|\tilde{\mathbf{q}}_i - \bar{\mathbf{h}}_i \tilde{\mathbf{P}}_i\right|\right|^2 + \lambda_i^2 \left|\left|\tilde{\mathbf{P}}_i\right|\right|^2\right\} \tag{4.4}$$

Prior to solving the preceding optimization problem, λ_i the optimal regularization parameter, should be determined in conjunction with L-curve (*Hansen and O'Lary* (1993); *Hansen* (2007)) or generalized cross validation (GCV) (*Wahba et al.* (1979)).

6. If required the identified modal wind load can be transferred to modal subspace of the modified version of the actual structure for the post analyses. The actual and modified structures called primary and secondary, respectively. Therefore it is looked for a transfer matrix $\mathbf{T}$, so that the modal subspaces between two structures can be exchanged, considering that principally $\mathbf{P} = \mathbf{\Phi}^T \mathbf{p}$:

$$\mathbf{T}\tilde{\mathbf{P}}_{St_1} = \tilde{\mathbf{P}}_{St_2} \;\Rightarrow\; \mathbf{T}\mathbf{\Phi}_{St_1} = \mathbf{\Phi}_{St_2} \tag{4.5}$$

where $\tilde{\mathbf{P}}_{St_1}$ and $\tilde{\mathbf{P}}_{St_2}$ denote the wind loads in the modal subspace of the primary and the secondary structure. Note that the latter is unknown. Then right multiplication by $\mathbf{m}_{St_1}\mathbf{\Phi}_{St_1}$ and provided that $\mathbf{\Phi}_{St_1}^T \mathbf{m}_{St_1} \mathbf{\Phi}_{St_1} = \mathbf{I}$, it renders:

$$\mathbf{T} = \mathbf{\Phi}_{St_2}^T \mathbf{m}_{St_1} \mathbf{\Phi}_{St_1} \tag{4.6}$$

Usually the mass matrix of the primary structure could be not available, since just its modal parameters are identified, while e.g. mathematical model of the secondary structure and accordingly its mass matrix should exist for further analysis. In this situation the above transfer matrix can be derived in terms of the secondary structure's mass matrix. Therefore the same scheme as above is followed such that:

$$\tilde{\mathbf{P}}_{St_1} = \mathbf{T}^{'}\tilde{\mathbf{P}}_{St_2} \tag{4.7a}$$

$$\mathbf{T}' = \mathbf{\Phi}_{St_1}^T \mathbf{m}_{St_2} \mathbf{\Phi}_{St_2} \tag{4.7b}$$

The comparison with the left hand of Eq. 4.5 yields $\mathbf{T} = \mathbf{T}^{'-1}$.

In this contribution the modal subspace transferring corresponding to Step 6 was not implemented, since this work does not include post analysis on the secondary structure. However the required theory for this purpose was given as the complementary information.

4.3 Results

4.3.1 The structure and measurement setup

The structure is located in Petzenkirchen, Lower Austria and serves as a weather station tower for mounting the meteorological sensors in the Hydrological Open Air Laboratory (HOAL) (*Blöschl et al.* (2016)). The structural response was obtained as a result of the ambient wind-induced excitation. The structure is a 9.1 m (30 ft) tall guyed mast, consisted of three parts. Each part has an equilateral triangular cross section, whose dimensions respectively from bottom to top are [0.43, 0.34, 0.26] m (*see Fig*. 4.1*a*). Each part of the mast is composed of three main legs and horizontal as well as the cross bracing elements, which are all made up of aluminum alloy. Three cables from either side account for the additional lateral constraint on the upper part of the mast, in order to prevent the wind over load. Figure 4.1b shows an in-situ picture of the mast structure.

The wind-induced acceleration response of the structures is measured in horizontal plane of the mast via capacitive accelerometers, which are suitable for relatively low frequency vibration measurements. The specifications of measurement sensors, which are products of PCB Piezotronics, are given in Table 4.1. An almost evenly distributed configuration for the sensor locations was chosen, which are marked by [S1:S7] in Fig 4.1a. It was avoided to mount the sensors very close to the locations of guys connection, since the vibration intensity around those points is poor. The vibration responses were measured in two perpendicular direction (i.e. x and y) at locations [S1, S3, S5, S6, S7], but in the rest of the locations namely [S2, S4] the response was measured just in one direction (y) in order to deliver the additional lateral measurement. As a result, there are 12 measurement channels in total. Through this sensor configuration one can measure general motion of the structure for a proper system identification, especially to take into account the coupled bending-torsional modes. A representation of the measurement setup on the mast, where acceleration response is measured in three horizontal directions, is shown if Fig. 4.2.

Table 4.1: Sensors specifications

Sensor	Type	Sensitivity ($mV/(m/s^2)$)	Frequency range (Hz)
Accelerometer	MEMS DC 3713B	101.9	0-250

4.3.2 Operational modal analysis

The modal characteristics of the structure has been identified based on the stochastic subspace identification method (*Peter and Roeck* (1999); *Reynders and Roeck* (2008); *Reynders et al.* (2008)) by means of the Matlab toolbox, so-called “MACEC” (*Reynders et al.* (2014)). The sampling rate for data acquisition was set to 100 Hz. In order to get a clue about the eigenfrequencies of the system, firstly the acceleration power spectrum of different measured channels were observed. For instance in Fig. 4.3a the power spectrum of the sixth channel corresponding to location S4 in direction y is illustrated. For a better resolution in the frequency range of interest for the wind induced vibrations, the signals were decimated by factor 7, which consequently yields to the new measurable upper bound of 7.1 Hz with respect to the Nyqvist frequency. The power spectrum of the decimated signal is depicted in Fig. 4.3b. The signal processing including signal decimation and the offset removal should be also carried out before system identification. Following, the results of operational modal analysis, regarding the six identified modes are provided in Table 4.2 and Fig. 4.4. It should be noted that in Fig 4.3b the peak associated with the third of the first four modes is not observable well, as this figure shows the signal merely in direction y and this mode has higher energy in the other direction i.e. x.

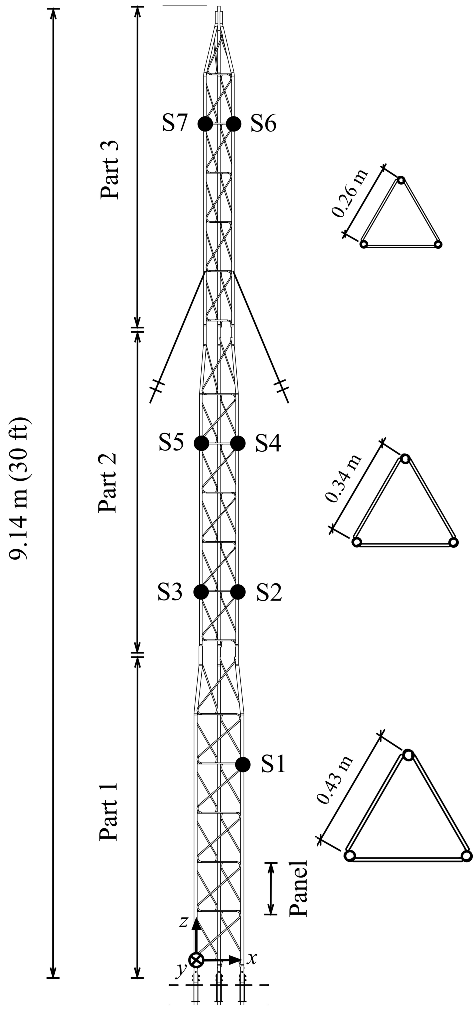

(a) Side view of the mast structure and response sensor locations

(b) Picture of the instrumented guyed mast

Figure 4.1: The representation of the mast structure and the response sensors configuration

(a) Picture of attached accelerometers on the mast

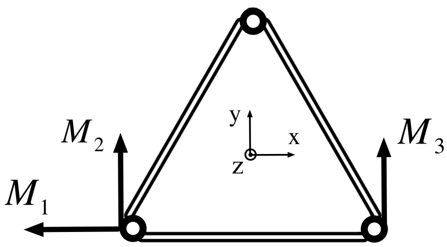

(b) Measurement arrangement of the corresponding sensors

Figure 4.2: View of response sensors on mast and measurement arrangement

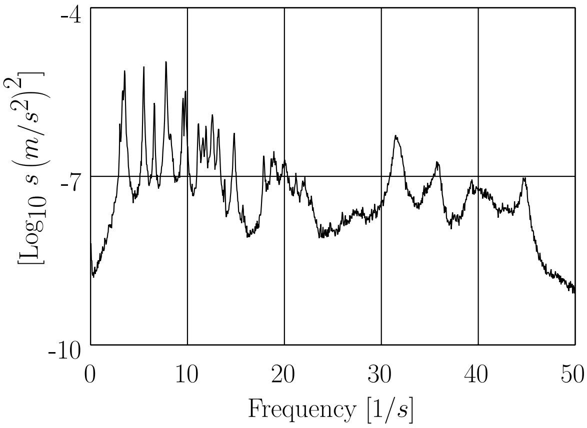

(a) Original measured signal

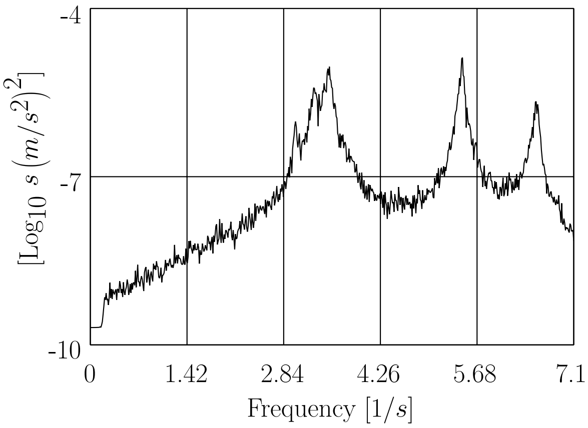

(b) Decimated signal

Figure 4.3: The measured signal power spectrum at sensor location S4 in direction *y*

Note that in reality the identified mode shapes from experimental vibration data are complex-valued vectors (*Mitchell* (1990); *Caughey and O'Klley* (1965)). As such the identified mode shapes were realized via the complex transformation matrix (*Niedbal* (1984); *Friswell and Mottershead* (1995)).

Table 4.2: The identified natural frequencies and damping ratios of the mast structure

Mode	1	2	3	4	5	6
Eigenfrequency (Hz)	3.03	3.31	3.44	3.53	5.49	6.58
Damping ratio (%)	0.52	1.36	0.9	0.91	0.44	0.56

4.3.3 Identification of the wind load

In this study solving the ill-posed inverse problem corresponding to Eq. 4.3 for fluctuating part of modal wind loads was accomplished by Tikhonov regularization scheme (*Tikhonov and Arsenin* (1997)). There are different methods dealing with the ill-posed inverse problems, to which the readers are referred for more information (*Hansen* (1987); *Klimer and O'Lary* (2001); *Varah* (1973)). The optimal regularization parameter, which is needed for solving the optimization problem of Eq. 4.4 has been determined by L-curve method as well as generalized cross validation (GCV).

The accuracy of the regularized solution is inversely proportional to the size of the problem, i.e. the dimensions of matrices in Eq. 4.3, which in turn depend on the time length and the system degrees of freedom (dofs). In *Kazemi-Amiri and Bucher* (2015), the augmented IRM was introduced and it was comprehensively explained how augmented IRM increases the accuracy of the input-output (force-response) relation, while keeping the problem size unchanged. Moreover by projecting the physical coordinates onto the modal subspace two advantages are achieved. Firstly the multiple dofs system reduces to one at each mode that gives rise to reduction of the problem size. Note that the single parameter Tikhonov regularization scheme treats the inverse problems with single dof much better than the case with multiple dofs. This is due to the fact that there might be different degrees of ill-conditioning with respect to each dof, while single regularization scheme cannot treat them individually but rather on average. There are methods developed based on the idea of multiple regularization levels like L-hypersurface (*Belge et al.* (2002)) and multiple GCV (*Modarresi* (2007)). Those methods are way more complex in

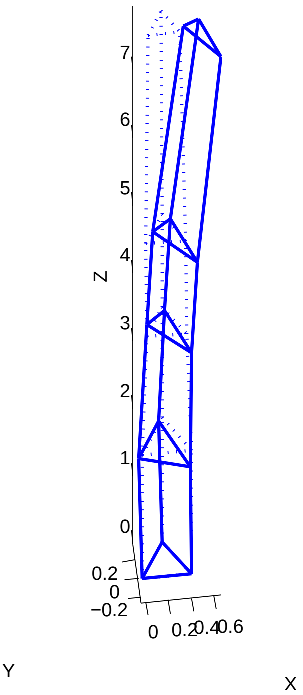

(a) 1st mode

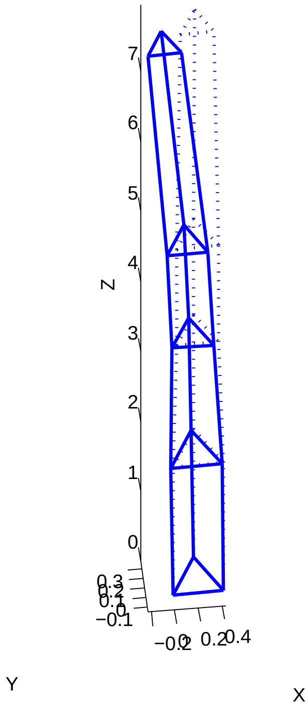

(b) 2nd mode

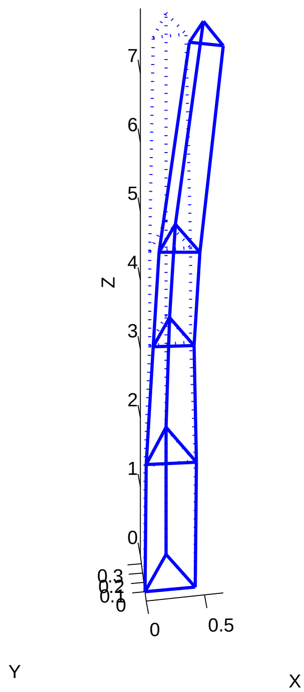

(c) 3rd mode

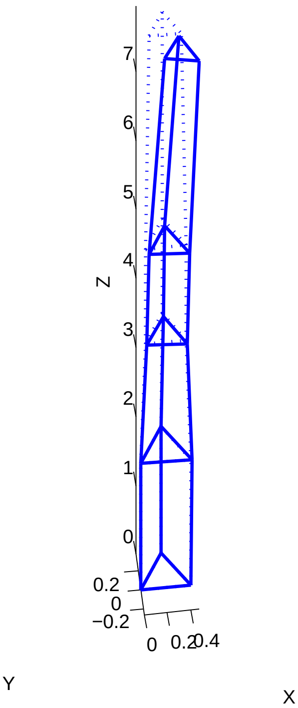

(d) 4th mode

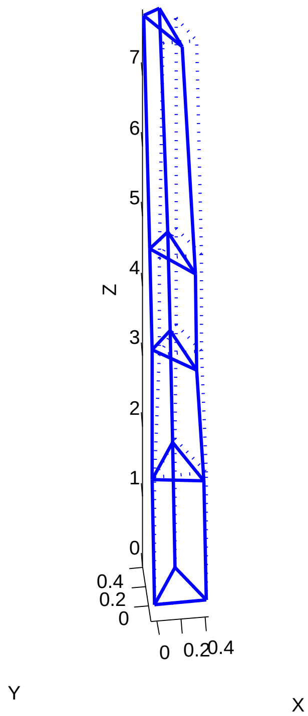

(e) 5th mode

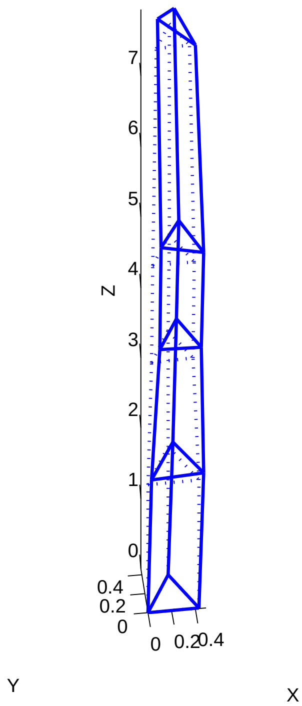

(f) 6th mode

Figure 4.4: Identified mode shapes

implementation than their single level counterparts and are usually more efficient for a few number of unknowns, which does not always hold for the case of wind load identification. The second advantage of modal projection is that the continuous quantity of wind pressure/load acting on the structural element is discretized in modal subspace as an equivalent single force. As a result of the latter, the underdetermined state of the corresponding inverse problem, with respect to a limited number of sensor locations, is also resolved. To sum up, the modal projection of the problem is effectively a good choice.

Afterwards, it should be decided, which response quantity is to be used for the wind load reconstruction. Importance is attached to the point that the response type is another influential factor on the accuracy of recovered load. According to author'e investigation (*Kazemi-Amiri and Bucher* (2015) and Chapter 3), the displacement response is more suitable over the acceleration in order to infer the wind loads. This is because of the condition number, which reflect the degree of instability of inverse problem response. The condition number of displacement IRM is considerably smaller than that of acceleration. It means that there is less sensitivity to the contained noise in the measured displacement signal and more accurate wind loads can be recovered.

4.3.3.1 Real application of the wind load identification

Acceleration and displacement are more common types of measured responses among others in structural vibration measurement tasks. However it was mentioned that the wind loads can be recovered more accurately based on the displacement response. But since the mast structure under measurement is relatively light-weight and on the other hand the accelerometers are also light-weight units, then accelerometers were used for the measurement purpose in order to avoid the drastic effect of sensor mass on the behavior of the structure. Consequently the displacement responses had to be derived from the measured acceleration. The acceleration signal is integrated twice in frequency domain according to integral property of Fourier transform to obtain the displacement responses (*Brandt and Brincker* (2014)). In order to prevent the drift phenomenon, which usually occurs due to integration, every time before integration the signal was windowed and also passed through high-pass Butterworth filter with cut-in frequency of 0.2 Hz.

As the multiple DOFs wind load identification is transformed to modal load reconstruction, the structural responses of the structure need to be decomposed into modal responses, once the system mode shapes are identified. The displacement signals were decomposed into their modal responses by means of the identified mode shapes, according to Eq. 4.2. In order to check the validity of the decomposed modal displacements responses, the power spectrum pertaining to the first six modes are plotted in Fig. 4.5. According this figure each signal features one dominant peak in the power spectrum corresponding to the modal natural frequency. This confirms that the displacement responses were correctly decomposed in the modal coordinates.

In the next step, the displacement modal impulse response matrices were constructed for 60 s according to the identified modal information in Table 4.2. To this end, with the time step equal to 0.07 s and based on the sampling rate of the decimated data i.e. 14.3 1/s, the size of the IRM should be set to $l = 857$ in Eq. 4.3 to have the desired time length. This equation was afterwards solved for the modal wind loads by means of the Eq. 4.4 through L-curve and GCV methods. The time history and power spectrum of the identified modal wind loads are given in Fig. 4.6. According to Fig. 4.6, the L-curve and GCV responses are almost the same in time history plots for the 1st to 4th modes. In Figs 4.7i and 4.7k corresponding to the 5th and 6th modes, GCV method (unlike L-curved) recovered the modal wind load just in the vicinity of the modal natural frequency. Consequently the identified wind loads by GCV have drastically small amplitudes in time history plots ($Figs.$ 4.7i and 4.7k) compared to those by L-curve.

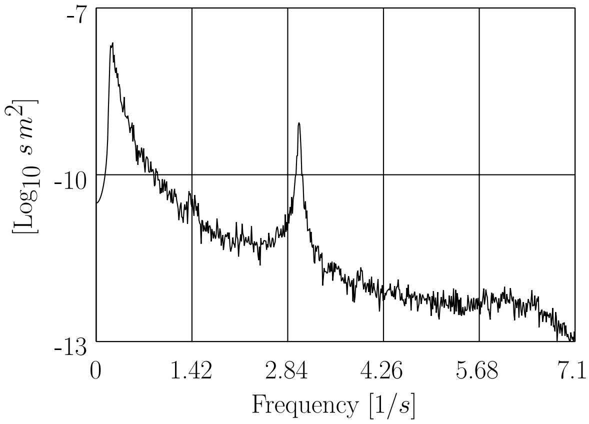

(a) 1st mode modal displacement

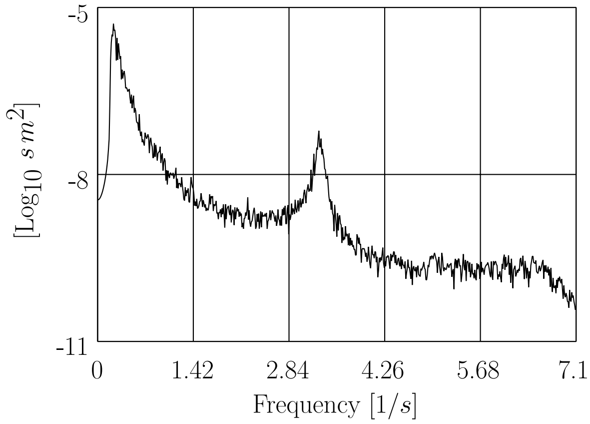

(b) 2nd mode modal displacement

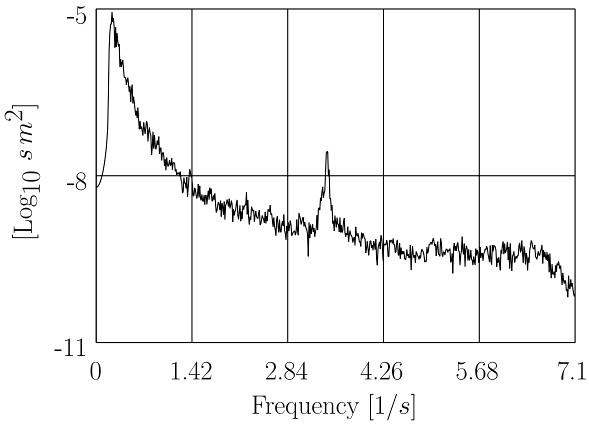

(c) 3rd mode modal displacement

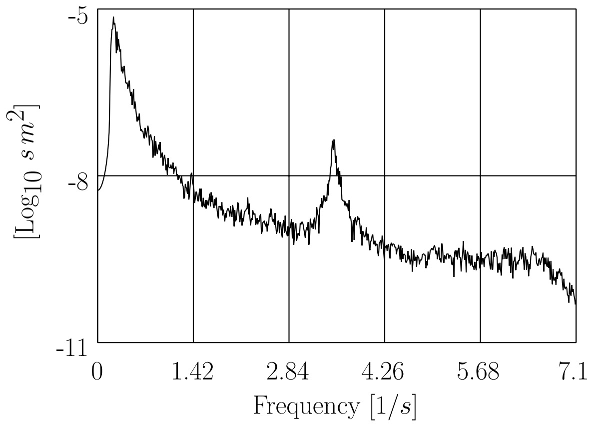

(d) 4th mode modal displacement

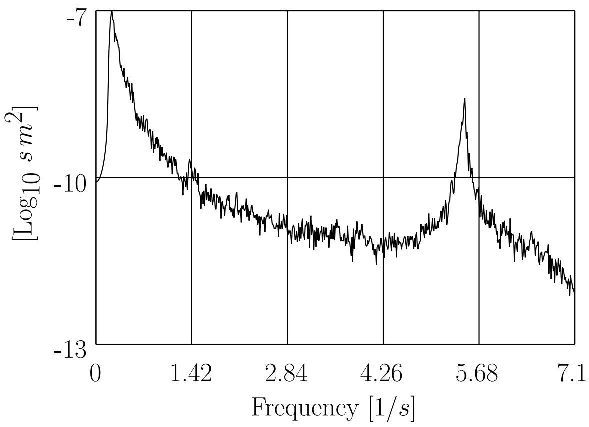

(e) 5th mode modal displacement

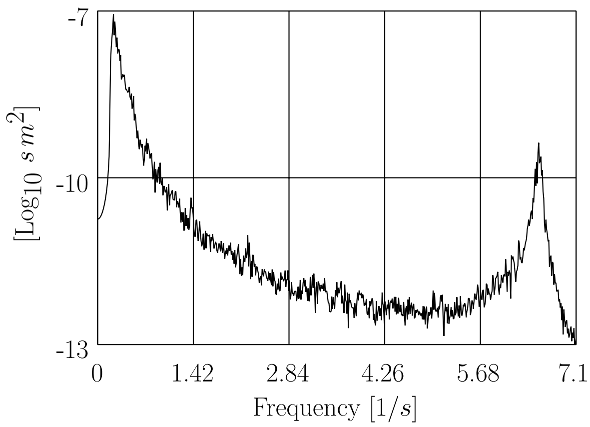

(f) 6th mode modal displacement

Figure 4.5: Power spectrum of the decomposed modal displacement responses

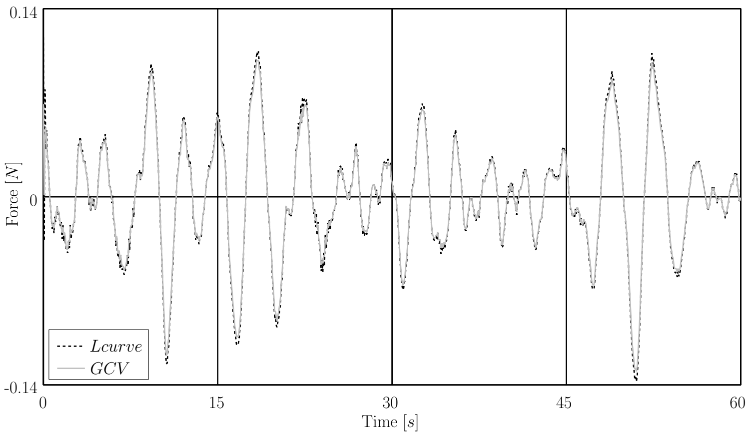

(a) 1st mode time history modal wind load

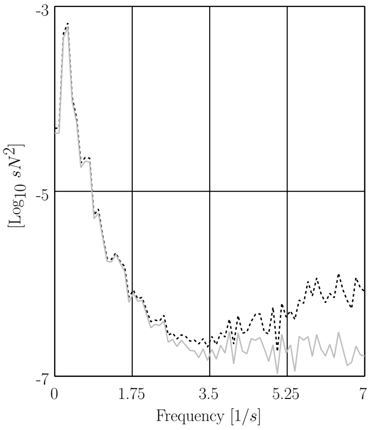

(b) 1st mode power spectrum modal wind load

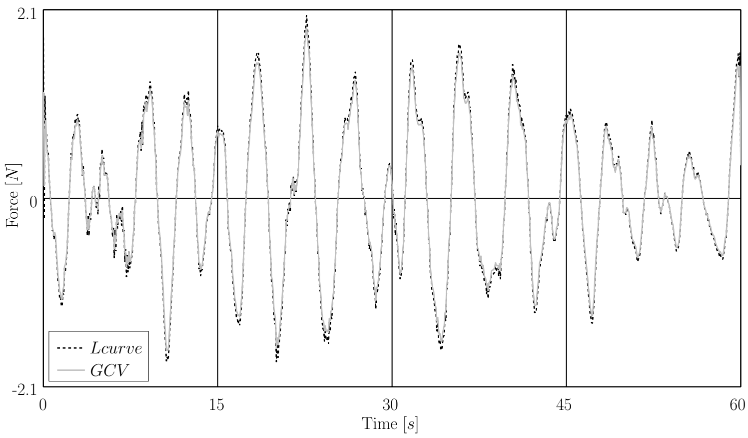

(c) 2nd mode time history modal wind load

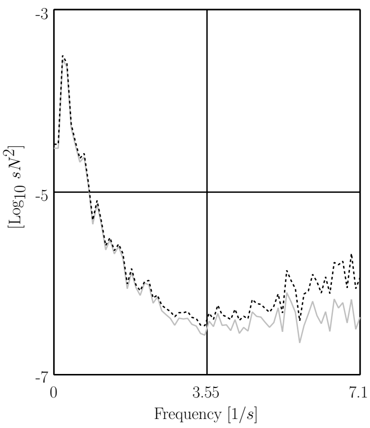

(d) 2nd mode power spectrum modal wind load

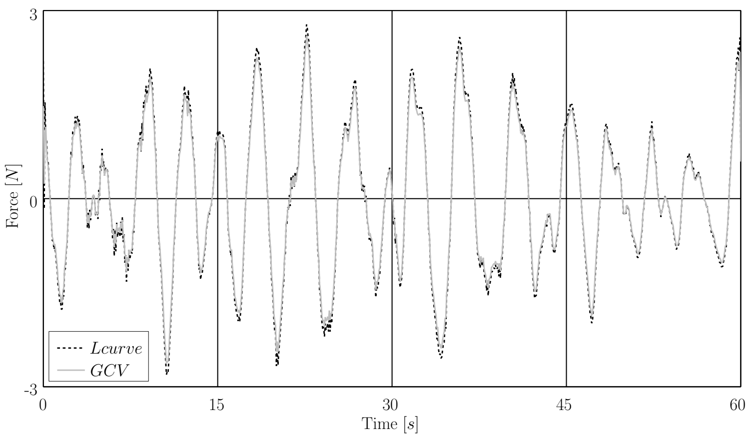

(e) 3rd mode time history modal wind load

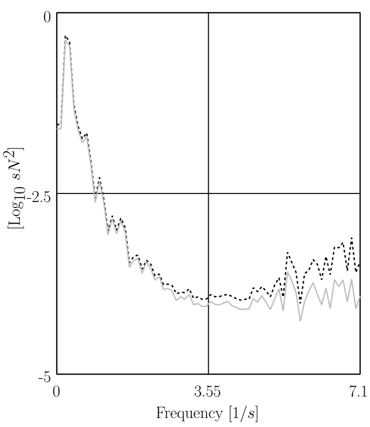

(f) 3rd mode power spectrum modal wind load

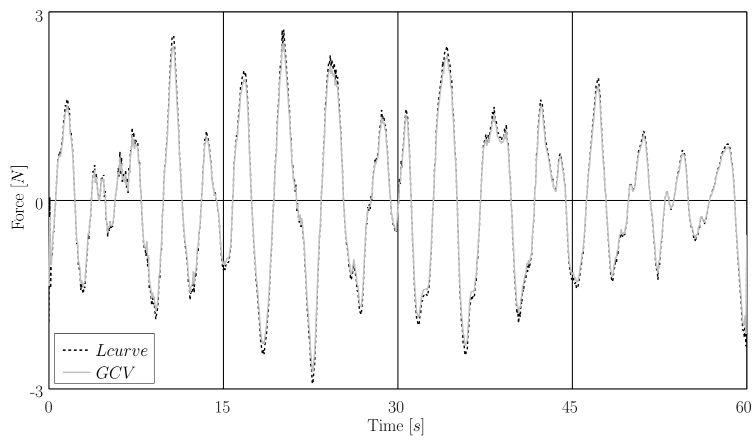

(g) 4th mode time history modal wind load

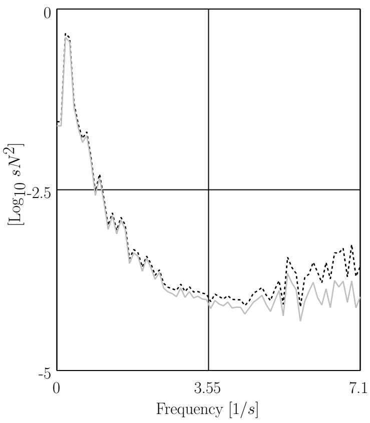

(h) 4th mode power spectrum modal wind load

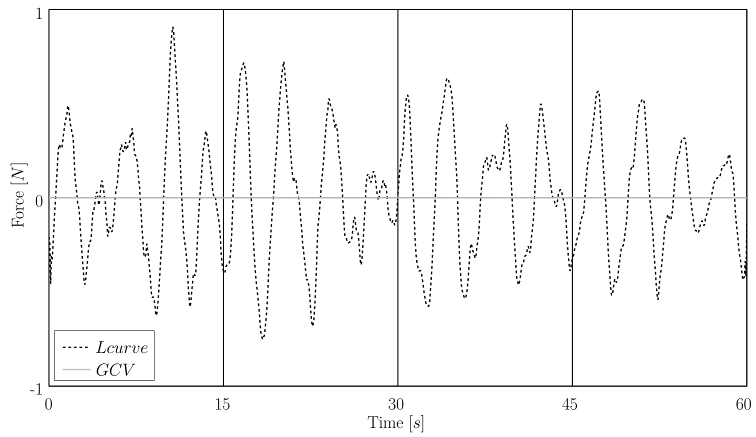

(i) 5th mode time history modal wind load

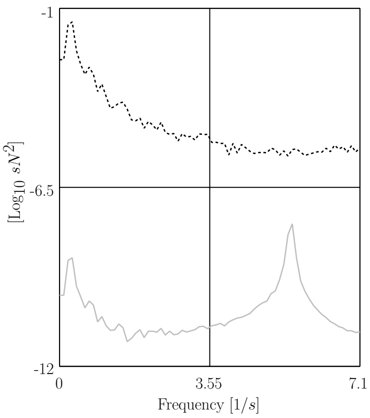

(j) 5th mode power spectrum modal wind load

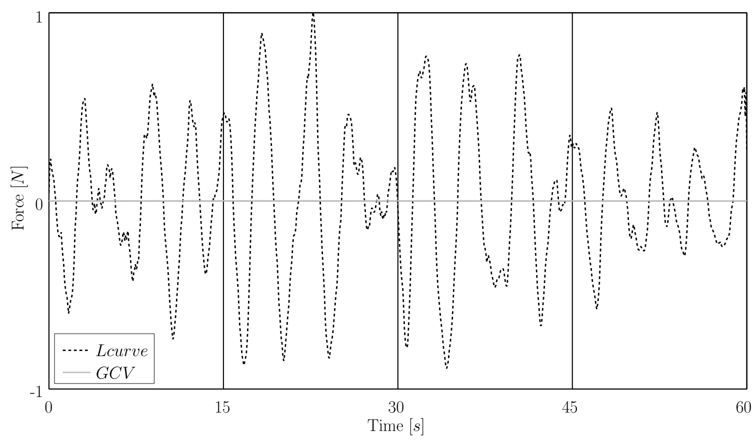

(k) 6th mode time history modal wind load

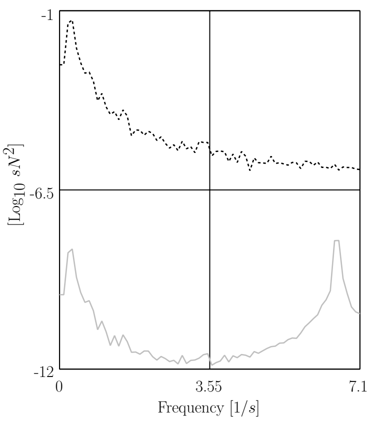

(l) 6th mode power spectrum modal wind load

Figure 4.6: Reconstructed wind loads from field measurement data

4.4 Verification of field application results

A procedure was sought for verifying the identified modal wind loads indirectly, since in contrast with the numerical simulation, the applied wind loads are not available in the full-scale testing. Some studies compare the retrieved responses from identified wind loads with the actual measured responses. However since Eq. 4.3 is derived based on the convolution integral, the IRM has smoothing effect on the applied load. It means that for a highly or slightly fluctuating identified load, apart from its validity, almost identical responses might be retrieved (*Hansen* (2007); *Groetsch* (1984)). As a result in this contribution, the results of the numerical simulation of the same problem is provided too.

Following, by inspection of the similarities in time and frequency domain between the features of the field and simulation reconstructed wind loads, the validity of the field results can be crosschecked.

4.4.1 Simulation of the wind load reconstruction

The full-scale finite element of the mast structure was created in SlangTNG (*Bucher and Wolff* (2013)). The acting wind loads along the structure were generated according to the digital simulation of the fluctuating part of wind speeds at different height levels, in two perpendicular horizontal directions independently. The correlated fluctuating wind speeds were simulated at 18 different heights corresponding to the panels of the mast with the assumption that wind speed is constant over one panel (*see Fig*. 4.1*a*). Then the resulted wind loads due to the action of wind pressure on the exposed area of mast elements, were considered as nodal forces on the nodes of mast cross sections.

The simulated noise polluted displacement response was achieved by adding the unit amplitude white noise with adjustable noise level to the displacement response, which is directly derived from solving the equation of motion . The noise was scaled with respect to the response standard deviation of the corresponding degree of freedom. The configuration of the virtual sensors as well as the measurement sampling rate are similar to the sensor configurations in Fig. 4.1a and the field measurement sampling rate, respectively.

The time history and the power spectrum of the reconstructed wind loads are illustrated in Fig. 4.7 for the first mode with the eigenfrequency equal to 3.03 Hz. The results obtained by L-curve and GCV are almost identical and of a high accuracy. The corresponding result of the fifth mode with the eigenfrequency of 5.69 Hz is also represented in Fig.4.7. Although GCV fails to find the optimal solution at this mode but L-curve provides a good quality recovered wind load signal. The noise level for the numerical simulation of the results was set to 10% of the response standard deviations of the responses at the location of the virtual sensors.

According to power spectrum plot in Figs.4.7b, it can be observed that a slight deviation of the identified signal power spectrum from that of the actual signal occurs only after the natural frequency of that mode and consequently the background signal is correctly identified. This leads to a negligible discrepancy between the identified and actual modal wind load signal in the time history plots. The validity of the experimental results corresponding to the first to fourth modes can be qualitatively verified by crosschecking with this set of simulation results. Analogous to the simulation results, the experimentally identified loads by GCV and L-curve are almost identical in time history with deviation of power spectrums after the natural modal frequencies. However less discrepancy is expected for the reconstructed loads by GCV since the deviation of the GCV-based identified loads power spectrum, after corresponding natural frequencies, are less compared to those recovered by L-curve. The next interesting analogy exist between the results of simulation in 5th mode and the real application in 5th and 6th modes. In simulation, GCV has obviously failed to recover the applied modal wind load except around related mode natural frequency (*Fig*. 4.7*d*). But rather L-curve could identify the wind load but relative inaccurately compared to the 1st to 4th modes result. As a result the validity of experimental results of the 5th and 6th modes can be verified but with a degree of uncertainty. Nevertheless, the higher the mode number the less contribution it has in the response to the input excitation.

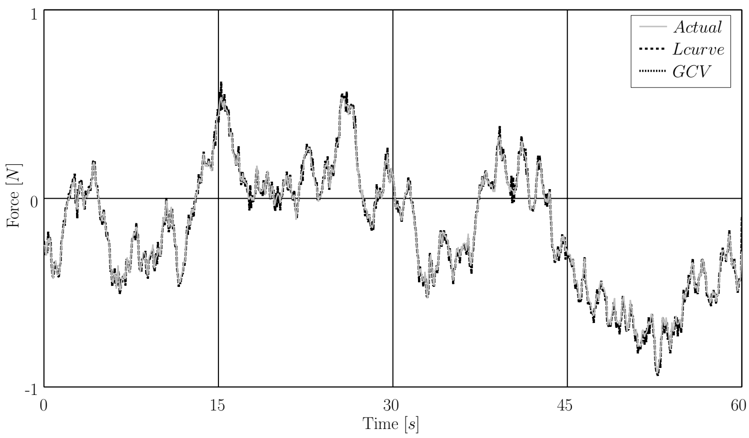

(a) 1st mode time history modal wind load

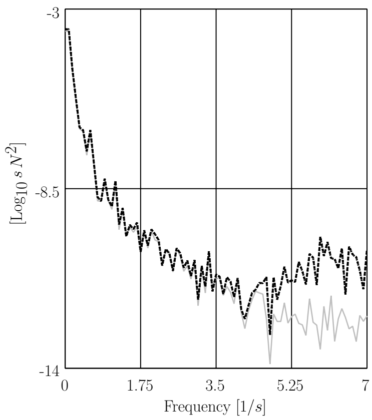

(b) 1st mode power spectrum modal wind load

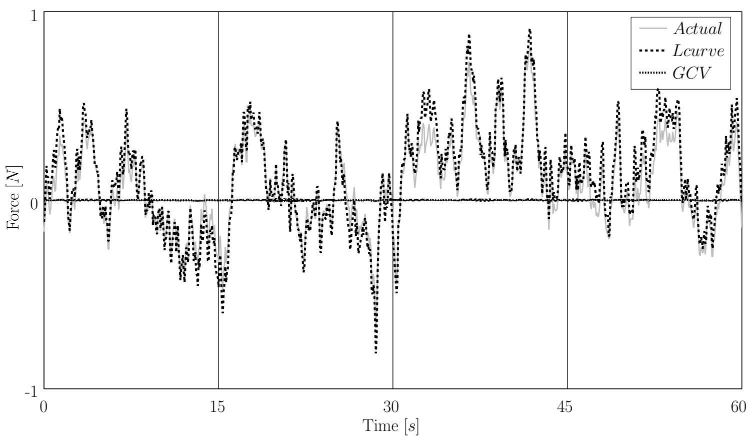

(c) 5th mode time history modal wind load

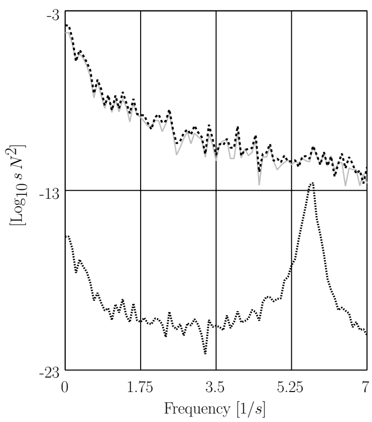

(d) 5th mode power spectrum modal wind load

Figure 4.7: Reconstructed wind loads from numerical simulation

4.5 Conclusion

In this contribution, it was dealt with the field application of an introduced procedure for modal wind load identification inversely from full-scale field measurement data of structural response. The major focus was drawn to the technical aspects of the practical application, including the case study, measurement setup, data processing and the utilized methods within the load identification procedure. It is important to note that all information needed for wind load identification was acquired solely based on the measurement data. In this regard, no additional assumptions were required to be made either on the structural properties e.g. assumptions on system mass or stiffness matrices or on the wind characteristics of the structure's site.

It was discussed profoundly, what are the advantages of wind load reconstruction in the modal subspace, use of displacement responses and utilizing the augmented modal impulse response matrices. The Tikhonov solution was utilized in conjunction with the methods of L-curve and GCV for tackling the inherent ill-posedness of the inverse load identification problem. The modal parameters (natural mode shapes and frequency and damping ratios) are required for the generation of the modal impulse matrices as well as decomposition of the measured displacement responses. The structural modal properties were obtained by means of operational modal analysis from the same ambient vibration testing data, which is used for inverse load identification.

It is not generally feasible in practice to measure the actual wind loads acting on the structural element, in order to verify the load identification results. It was described that there might not exist another solution for this purpose better than simulation of the problem and observation of the existing analogies. The numerical simulation of the same problem can demonstrate the strength or weakness of the introduced procedure for practical wind load identification. Consequently the validity or failure in the real application of the introduced procedure was verified by means of the analogy between the field and numerical simulation results. It was obviously observed that for a number of first vibration modes the experimental results are reliable. Last but not least, as the case study had the complexity and generality of an arbitrary structure sufficiently, this method can be applied for modal wind load identification of other structures too.

Chapter 5

Collaborative research contribution

Vienna doctoral program on water resource systems is a multidisciplinary program, which consists of several research clusters. Collaborative research works between and within clusters is one of the main focuses of the doctoral program. In this regard, every PhD candidate is encouraged to plan research projects with the collaboration of other candidates in the relevant research fields. The author's contribution to the collaborative research work includes two parts. section 5.1, entitled "Wind-induced stochastic response analysis from sparse long-term response data", is an interdisciplinary collaboration with Mr. Patrick Hogan, whose specialization is Astrophysics and Meteorology. Section 5.2 is comprised of a research project together with Dr. Franz Bamer in the same discipline as mine, entitled "A new model order reduction strategy adapted to nonlinear problems in earthquake engineering".

5.1 Wind-induced stochastic response analysis from sparse long-term response data

The main objective in this study is to develop methods for stochastic response analysis of structures under wind-induced excitation, when the discontinuous/sparse measured response (acceleration, velocity and strain/stress) is available. The measurement was carried out over one year according to predefined intervals (of orders of hours) between each triggering, which at least should have 10 minutes duration. In this regard it is of high interest to establish a mathematical relationship between structural response indicators and mean wind speed corresponding to the measurement sets. Hence wind speed data is an underlying key factor of the introduced methods and makes this contribution an interdisciplinary work between structural mechanics and meteorology. Those response indicators dealt with here are response standard deviation, response threshold passage counts as well as moments of area of the stress power spectral density (PSD) used for stress cycle counting that is an inevitable item in wind fatigue evaluation. The mentioned relationship with mean wind speed assists to interpolate the missing data corresponding to the gaps in the measurement data.

By application of the mentioned idea the amount of measurement data is considerably reduced, which in turn raises the computational efficiency for long term wind stochastic response analysis. This efficiency is considered to be beneficial for structural monitoring in initial in-service ages of structure. For the sake of design, usually through a large simulation process, the dynamic response analysis of the structure to wind excitation with different direction and mean wind speed must be carried out. However it is well-known that the structural behavior can be notably different after construction due to several resons including the assumptions made in modeling of structure and surrounding ambient effects as well as imperfections and manmade errors during the construction phase. As a result this study aims to provide a fast, efficient and especially realistic methodology, working based on discontinuous vibration measurement under wind excitations. Furthermore the proposed method also assists to fill the measurement gaps, which usually occurs even within any long-term continuous monitoring program, as it is quite likely that measurement gaps exist due to different reasons e.g. defects/crashes of the sensors, data acquisitions, storage equipments or power outage etc.

5.1.1 Introduction

Wind effects on the structure can be seen from different aspects. For example in the sense of building energy and thermal performance of buildings wind can cause heat loss through increasing the infiltration rate and surface heat transmission (*Arens and Williams* (1977)). Wind can disturb the occupants comfort due to imposing uncontrolled accelerations on tall buildings (*Melbourne and Palmer* (1992); *Kareem* (1983)). Excessive wind-imposed structural displacement can also cause destruction on the mechanical installations or on architectural elements. In addition to the above mentioned issues, wind can affect a wide range of structures including ordinary buildings, high-rise buildings and towers, overhead power lines, on/offshore wind turbines, cranes and industrial chimneys etc (*Huang* (2016); *Nateghi-A* (1996); *Yeter and Soares* (2013)). In this sense the wind loading accounts for the destructive effects on the structures, which depending on the particular case can be due to wind overloads in storm events (e.g. hurricanes, typhoons), aeroelastic stability issues, architectural damages due to sudden change in wind pressure gradients or cumulative fatigue damage in structural elements etc. As a result wind loading of structures has received substantial research effort within the last decades in many countries (*Holmes* (2007)). A breakthrough in wind engineering was the introduction of wind tunnel testing. Wind tunnel tests try to simulate the wind turbulence caused by different regimes in atmospheric boundary layer (*ASCE* (2012)). Plenty of useful benefits were achieved by wind tunnel tests in wind engineering. Wind tunnel tests also assisted to codify many aspects of wind loading. However the wind tunnel tests are also prone to uncertainty since the exact simulation of a natural phenomenon might be impossible. Nowadays in addition to the wind tunnel tests, which usually are performed before construction, in-situ structural health monitoring is also implemented. Many structures which serve as lifelines e.g. important bridges, main power lines or power plants according to their degree of importance might experience structural health monitoring from beginning of their service life. The outcomes of this contribution tries to provide an efficient and fast method for stochastic wind response analysis of structures by linking structural response and wind speed data, that can be achieved through field measurement. Since whole data will be obtained from field measurements at least over one year, then the realistic wind mechanism of the site as well as changes in structural properties due to meteorological and seasonal changes are considered. However it is self-evident that in order to capture the effects of extreme events, data corresponding to a much longer time period is required. Fortunately nowadays long term wind data is available due to the presence of numerous weather stations around the world. Therefore the extreme events wind data corresponding to the structure's site can be corrected by means of the existing data from the weather station at another similar site in the neighborhood.

In this study the stochastic structural response of a mast structure which serves as a weather station in conjunction with the associated wind speed data is analyzed. The weather station belongs to the Hydrological Open Air Laboratory (HOAL) of Vienna Doctoral Program on Water resource systems. The structural acceleration of the mast was measured within one year according to an 18-hour automatic triggering, that records data for a duration of 30 minutes. The wind speed, whose data analysis is relatively cheaper, was continuously measured in parallel. The one year ten-minute mean wind data was processed to detect the predominant wind direction at the structure's site. Thereby histogram and accordingly the mean wind speed probability distribution function of different blowing directions were obtained. Every triggered structural data was tagged by its associated mean wind speed data. Then the mathematical relationships between mean wind speed data and response standard deviation, displacement response threshold passage counts and moments of area of the stress power spectral density was sought, in order to retrieve the missing data corresponding to the unmeasured ten-minute time intervals. The first two mentioned indicators are used for the purpose of the structural vibration control under wind, while the latter is used for frequency domain fatigue damage estimation.

5.1.2 Wind-induced stochastic response analysis

5.1.2.1 Theoretical background

Consider the classically damped equation of motion for a single degree of freedom (SDOF) linear system under arbitrary dynamic load $f(t)$ as input:

$$m\ddot{u} + c\dot{u} + ku = f(t) \tag{5.1}$$

In the above relationship u, m, c, k denote the displacement, mass, damping and stiffness of the system. The equation of motion can be solved by means of convolution (Duhamel) integral as follows (*Clough and Penzien* (1995); *Maia et al.* (1998)):

$$u(t) = \int_0^t f(\tau)\, h(t-\tau)\, d\tau \tag{5.2}$$

in which $h(\tau)$ is the so-called impulse response function. Applying the Fourier transform on both sides of Eq. 5.1 and solving for $U(\omega)$, which is the system response in frequency domain, yields(*Maia et al.* (1998)):

$$U(\omega) = H(\omega).F(\omega) \tag{5.3}$$

while $H(\omega)$ is the response transfer function. Comparison of Eqs.5.2 and 5.3 shows that those are respectively time and frequency domain pairs such that (*Clough and Penzien* (1995); *Maia et al.* (1998)):

$$H(\omega) = \int_{-\infty}^{\infty} h(t)\, e^{-i\omega t}\, dt \tag{5.4}$$

In order to analyze the stochastic response of the system, the ensemble average of response, that is $E\left[u(t)\, u(t+\tau)\right]$, should be evaluated. It has been illustrated (*Clough and Penzien* (1995)), that if the input is a zero mean stationary process, then the response is also stationary with the autocorrelation function equal to:

$$R_u(\tau) = E\left[u(t)\, u(t+\tau)\right] = \iint_0^{\infty} R_p(\tau - \theta_2 + \theta_1)\, h(\theta_1)\, h(\theta_2)\, d\theta_1\, d\theta_2 \tag{5.5}$$

where $\theta_1 = t - \tau_1$ and $\theta_2 = t + \tau - \tau_1$ are expressed in terms of dummy time variables τ_1 and τ_2 corresponding to two fictitious time instants. The power spectral density (PSD) function of the response S_u is related to the response autocorrelation function through the Fourier transform as follows (*Clough and Penzien* (1995); *Bucher* (2009a)):

$$S_u(\omega) = \frac{1}{2\pi} \int_{-\infty}^{\infty} R_u(\tau)\, e^{-i\omega\tau}\, d\tau \tag{5.6}$$

Substituting Eq. 5.5 and after some computations, above relationship reduces to the following (*Clough and Penzien* (1995); *Bucher* (2009a)):

$$S_u(\omega) = |H(\omega)|^2 \, S_f(\omega) \tag{5.7}$$

In order to find the response variance firstly the inverse pair of Eq. 5.6 is considered:

$$R_u(\tau) = \int_{-\infty}^{\infty} S_u(\omega) \, e^{i\omega\tau} \, d\omega \tag{5.8}$$

By means of the latter and Eq. 5.7, as the process is zero mean, then the response variance is derived:

$$\sigma_u^2 = R_u(\tau = 0) = \int_{-\infty}^{\infty} |H(\omega)|^2 \, S_f(\omega) \, d\omega \tag{5.9}$$

The above derivatives can be extended to the case of lightly damped linear multiple degrees of freedom (MDOF) system by means of modal analysis, where the set of uncoupled modal equations of motion is given below:

$$\ddot{\mathbf{q}} + 2 \, diag[\zeta_i \omega_i] \, \dot{\mathbf{q}} + diag[\omega_i^2] \, \mathbf{q} = \mathbf{P}(t) \tag{5.10}$$

in which $\mathbf{P}(t) = \boldsymbol{\Phi}^T \boldsymbol{p}(t)$ denotes the generalized dynamic loads in modal coordinates. Any response quantity $z(t)$, e.g. shear force, moment at a section or response at a degree of freedom, can be obtained by linear combination of the modal responses $z(t) = \sum_n B_n \, q_n(t)$. For instance if $z(t)$ corresponds to the response at a degree of freedom j then $B_n = \phi_{jn}$, or if $z(t)$ denotes the base shear of a building, then $B_n = [1 \ldots 1] \, \mathbf{f_n} = \omega^2 \, [1 \ldots 1] \, \mathbf{M} \boldsymbol{\phi}$ (*Clough and Penzien* (1995)). In the latter $\mathbf{f_n} = \omega^2 \mathbf{M} \boldsymbol{\phi} q_n$ is the equivalent modal static external load in terms of modal responses which is used for structural analysis at each time step (*Chopra* (1995)).

Similar to SDOF case the autocorrelation function can be written, that yields (*Clough and Penzien* (1995)):

$$R_z(\tau) = E\left[z(t) \, z(t+\tau)\right] = \sum_m \sum_n R_{z_m z_n}(\tau) \tag{5.11}$$

while (*Clough and Penzien* (1995))

$$R_{z_m z_n}(\tau) = \iint_0^{\infty} B_m \, B_n \, R_{P_m P_n}(\tau - \theta_2 + \theta_1) \, h_m(\theta_1) \, h_n(\theta_2) \, d\theta_1 \, d\theta_2 \tag{5.12}$$

In case of civil engineering structures with low damping, whose mods are not closely spaced, the responses of m^{th} and n^{th} mode are approximately uncorrelated, which simplifies the autocorrelation function of a MDOF system (Eq. 5.11) to the following (*Clough and Penzien* (1995)):

$$R_{z_m}(\tau) \approx \sum_m R_{z_m z_m}(\tau) \tag{5.13}$$

which immediately gives rise to the following relationship for variance of the response quantity:

$$\sigma_z^2 = \sum_i \sigma_{z_i}^2 \tag{5.14}$$

The PSD for the response $z(t)$ of a MDOF system is computed by taking the Fourier transform from Eq. 5.11 (*Clough and Penzien* (1995)):

$$S_z(\omega) = \sum_m \sum_n S_{z_m z_n}(\omega) = \sum_m \sum_n B_m \, B_n \, H_m(-\omega) H_n(\omega) \, S_{P_m P_n}(\omega) \tag{5.15}$$

where $H_i(\omega)$ stands for the frequency response function at i^{th} mode and $S_{P_mP_n}$ is the cross spectral density function for the modal load processes P_m and P_n. Integrating Eq. 5.15 from $-\infty$ to ∞ gives the variance. Again the modal cross contributions can be neglected, which simplifies the response PSD to:

$$S_z(\omega) \approx \sum_m S_{z_m z_m}(\omega) = \sum_m B_m^2 \, |H_m(\omega)|^2 \, S_{P_mP_m}(\omega) \tag{5.16}$$

It was mentioned before, that the generalized modal load at m^{th} mode is given by $P_m(t) = \boldsymbol{\phi}_m^T \boldsymbol{p}(t)$. Consequently if each individual load at i^{th} dof is defined by $S_{p_i}(\omega)$ (or equivalently $R_{p_i}(\omega)$), then the covariance function and cross spectral density of modal loads P_m and P_n can be derived as follows (*Clough and Penzien* (1995)):

$$S_{P_mP_n}(\omega) = \sum\sum \phi_{im}\,\phi_{kn}\,S_{p_ip_k}(\omega) = \boldsymbol{\phi}_m^T \mathbf{S}_p(\omega)\boldsymbol{\phi}_n \tag{5.17}$$

and

$$R_{P_mP_n}(\tau) = \sum\sum \phi_{im}\,\phi_{kn}\,R_{p_ip_k}(\tau) = \boldsymbol{\phi}_m^T \mathbf{R}_p(\tau)\boldsymbol{\phi}_n \tag{5.18}$$

where m, n correspond to mode number and i and k denote the degree of freedom and $\mathbf{R}_p$ and $\mathbf{S}_p$ are the covariance and PSD matrices of external dynamic loads, with matrix components $R_{p_{ij}}$ and $S_{p_{ij}}$ respectively. The power spectral density S_z can be also derived, similar to Eq. 5.15, but rather directly in the physical coordinates without modal expansions.

According to Davenport (*Davenport* (1961b, 1963)), conceptually wind speed can be treated as a stationary random process by summation of the time-averaged (mean) $\bar{X}$ and the fluctuating part $x(t)$.

$$X(t) = \bar{X} + x'(t) \tag{5.19}$$

Consequently the preceding analysis method applies to wind vibration analysis and as a result the above definition for $X(t)$ also applies to the wind pressure/force as well as different types of structural response (*Holmes* (2007)). Hereafter the wind effect is confined just to the along-wind (so-called drag) force, without loss of generality though. If variable $X(t)$ is replaced by $V(t)$, which is to stand for the wind speed, by quasi-steady assumption of the wind flow, the drag force is derived such that (*Simiu and Scanlan* (1978)):

$$F_D(t) = \frac{1}{2}\rho_{air}V^2AC_D = \underbrace{\frac{1}{2}\rho_{air}\bar{V}^2A\,C_D}_{\bar{F_D}} + \underbrace{\rho_{air}A\,C_D(\bar{V}v'(t) + v'(t)^2/2)}_{f'_(t)} \tag{5.20}$$

where the frontal area $A = B\,l$ consist of the breadth of structure/element, B, normal to the wind with length l, and C_D is the so-called drag coefficient. In the right hand side of Eq. 5.20, the second order term of fluctuating wind speed is usually neglected (*Simiu and Scanlan* (1978)).

In order to be able to evaluate Eq. 5.16, the wind load PSD matrix must be known. The wind load PSD can be determined by means of Fourier transform of the wind load autocorrelation function and using the linear part of $f'(t)$ (*Holmes* (2007)):

$$S_{F_D}(\omega) = \frac{4\bar{F_D}^2}{\bar{V}^2}\chi^2 S_v(\omega) = \rho_{air}^2\bar{V}^2A^2C_D^2\chi^2 S_v(\omega) \tag{5.21}$$

in which $S_v(\omega)$ is the wind speed power spectrum and χ, so-called aerodynamic admittance, accounts for adjustment of the non-stationary effects. There are different functions suggested in literature (*Simiu* *and Scanlan* (1978); *Holmes* (2007)) for wind speed power spectrum (e.g. see Eq. 3.14). Principally, the square of the reference mean wind speed appears in wind speed power spectrum. Therefore the relationship between mean wind speed and wind speed power spectrum is nonlinear of second order.

For two different physical points $i(y_1, z_1)$ and $k(y_2, z_2)$, located on a line perpendicular to the wind direction the wind cross spectral density is given by (*Simiu and Scanlan* (1978)):

$$S_{V_iV_k}(\omega) = \sqrt{S_{V_iV_i}(\omega)S_{V_kV_k}(\omega)}exp\left[-\omega\,\frac{\sqrt{C_z^2(z_1-z_2)^2+C_y^2(y_1-y_2)^2}}{2\pi(\bar{V}_{z_i}+\bar{V}_{z_k})}\right] \tag{5.22}$$

while C_z and C_y are exponential decay coefficient and are determined experimentally. Considering Eq. 5.22, the cross spectral density of wind load becomes:

$$S_{f_if_k}(\omega) = \rho_{air}^2\bar{V}_i\bar{V}_kA_iA_kC_{D_i}C_{D_k}\chi_i\chi_kS_{V_iV_k}(\omega) \tag{5.23}$$

By means of the above function the elements of wind load PSD matrix $\mathbf{S}_f$ is calculated. This matrix and its associated covariance matrix can be used in Eqs. 5.17 and 5.18, respectively.

5.1.2.2 Stochastic response analysis from sparse response measurements

It is quite useful in many fields of wind engineering to divide the wind, blowing in a site, into a couple of identical angular spacings, where each spacing represents the blowing direction and then within each direction the histogram of the mean wind speed can be obtained. This is done in order to identify the predominant wind directions and obtaining the probability density function of the mean wind speed. It is common practice to consider, that structural response sets under different excitations corresponding to the wind of a specific direction and mean wind velocity, have the same statistical properties and this assumption is also used in the simulations for evaluation of wind fatigue (*Jia* (2011)). This is due to the fact that they belong to the ensemble of the random processes with similar wind load PSD (see Eq. 5.21). It is investigated in this study how the wind response statistics can be obtained if solely the discontinues/sparse measured response data of the fluctuating part of wind load over a long period of time is available. Consequently, the mathematical relationship between the mean wind speed in a specific wind direction and the response standard deviation of the zero mean fluctuating structural response is sought. According to definition standard deviation is the second root of variance, which can be found by integrating Eq. 5.15:

$$\sigma_z^2(\omega) = \sum_m\sum_n\int_{-\infty}^{\infty}S_{z_mz_n}(\omega)\,d\omega = \sum_m\sum_n B_mB_n\int_{-\infty}^{\infty}H_m(-\omega)H_n(\omega)S_{P_mP_n}(\omega)\,d\omega \tag{5.24}$$

In above relation, the response variance is a function of response transfer function, $H(\omega)$, and PSD of the modal wind loads, i.e. $S_{P_mP_n}$. The response transfer function is the structure's property, while the PSD of the modal wind loads are dependent on the external excitation. More inspection by considering Eqs. 5.17 and 5.21, and the fact that the square of the reference mean wind speed appears in wind speed power spectrum, reveals that the relationship between the PSD of modal wind loads (or response variance) and the reference mean wind speed must be of fourth order. Consequently the response standard deviation is function of the square of the reference mean wind speed. When the measured wind excitation response exists, this second order relationship can be found experimentally from the pairs of the discontinuous response data versus different wind speeds by means of a second order polynomial curve fitting.

Another objective is seeking the relationship between mean wind speed at a reference height and the number of data points corresponding to the absolute value of responses at a structural point that are larger than a certain threshold (*threshold passage counts*). This relationship can be also established experimentally according to the data of discontinuous response measurement at different mean wind speeds over one year, which turns out to be a linear relationship.

The mathematical expression for both response standard deviation and threshold passage probability can be used for in-service structural vibration control and failure probability estimation related to risk analysis under random excitations.

5.1.3 Fatigue analysis

Structural or mechanical components are frequently subjected to repeated loads. The resulted cyclic stresses, even at levels well below the given material's ultimate strength, cause microscopic damages in those components (*Dowling* (2013)). Accumulation of the microscopic damage leads into crack nucleation, short and long crack growth and final fracture, due to which failure of the element occurs (*Lee et al.* (2005)). This whole process is called *fatigue*. At present there are three main approaches to estimating fatigue life (namely total time/cycles under cyclic load until failure), including stress-based, strain-based and fracture mechanics approach. In this contribution the traditional stress-based approach is dealt with. According to the stress-based method, a fatigue cumulative model is used in order to accumulate the amount of damage associated with the number of cycles under different stress levels. The cumulative models are comprised of the nonlinear, bilinear and finally the linearized model (Palmgren-Miner). The simplicity and relative accuracy of the latter (Palmgren-Miner) made it the most popular one among other models. Unlike the latter, the two former are indeed complicated in real applications.

According to Palmgren-Miner rule, if a certain stress level σ_i is applied for a number of cycles N_i, the fraction of the used life (damage), which is independent of the cycles under another stress level, is N_i/N_{f_i}. Obviously N_{f_i} is the number of stress cycles to failure at a certain stress level. Consequently the failure is expected when the sum of fatigue damage fractions equals unity (*Dowling* (2013); *Lee et al.* (2005)):

$$\sum_i \frac{N_i}{N_{f_i}} = 1 \tag{5.25}$$

In order to be able to calculate the cumulative damage, N_i and N_{f_i} need be determined. In the subsequent chapter, different techniques for counting the number of cycles of various stress levels within a loading block will be described. The number of stress cycles to failure N_{f_i} is usually determined according to the *stress-life* or $S-N$ curves, which are derived based on fatigue tests for different metals.

It was mentioned that the stress cycles are responsible for the cyclic loading damage. One stress cycle corresponds to a closed loop, with maximum and minimum stress respectively σ_{max} and σ_{min} respectively, in the stress hysteresis plot of the loading block. The number of cycles to failure is then calculated as follows (*Dowling* (2013); *Lee et al.* (2005)):

$$N_f = \frac{1}{2}\left(\frac{\sigma_a}{\sigma_f' - \sigma_m}\right)^{\frac{1}{b}} \tag{5.26}$$

where σ_f' and b are obtained from the S-N curve of a certain material and the stress amplitude σ_a and mean stress σ_m are determined by the following definitions:

$$\sigma_a = \frac{\sigma_{max} - \sigma_{min}}{2}, \quad \sigma_m = \frac{\sigma_{max} + \sigma_{min}}{2} \tag{5.27}$$

5.1.4 Cycle counting Techniques

For fatigue damage estimation the number of cycles of different stress levels must be counted. The cycle counting, depending on the loading type, can be easy or indeed complicated. If the loading is made up of a couple of consecutive harmonics then the cycles are easily countable. But instead, for an irregular loading history a more sophisticated technique should be adopted. Generally there are time and frequency domain approaches in cycle counting for fatigue analysis.

Usually the features of loading history must be considered, whether the structural element undergoes the uni- or multi-axial loading. For the uni-axial loading there is the efficient cycle counting method, called rainflow cycle counting (*Matsushi and Endo* (1968); *Dowling and Socie* (1982)). The cycle counting will become even more difficult in case of an element undergoing variable multi-axial loads. For the multi-axial loading with purely in or out of phase loading in each axis (proportional loading), there exist just one principle stress plane throughout the loading history. Thus by means of the signed version of *Von Mises* or *Tresca* stress, an equivalent stress time history can be generated. Afterwards the traditional rainflow count algorithm is applied. It was shown in (*Sines* (1955)) that the mean torsional stress does not affect fatigue life. Consequently if the stress signal can be separated into mean and fluctuating parts, as in wind vibration response, the equivalent torsional stress history can be generated just from the fluctuating part of the response for fatigue estimation without taking the presence of mean stress into account.

The most complicated case is the stress/strain cycle counting of non-proportional multi-axial loading histories, in which the angle of the principal stress plane changes during the loading history and consequently just the introduction of the equivalent Tresca or Von Mises stress is not enough. There are plenty of different methods developed for cycle counting of non-proportional multi-axial loading. Above all the critical plane approach (*Bannantine and Socie* (1991)) and Wang and Brown's approach (*Wang and Brown* (1996)), both of which are strain-based methods, can be mentioned. Recently two stress-based methods were introduced, which both define an equivalent uniaxial stress function. The first is an empirical method (*Anes et al.* (2014)) and the second (*Irvine* (2016)) defines a hypersphere equivalent stress function. It should be noted that the methods developed for non-proportional multi-axial loading, are either pretty complicated in implementation or are not global to handle cases with different loading features or materials.

Fortunately in structural mechanics the contribution of the normal stresses are dominant over that of the torsional or shear stresses. As a result in most of the cases, the multiaxial fatigue estimation problems reduce to the class of uniaxial normal stress fatigue estimation. Hence the traditional rainflow cycle counting in time or frequency domain fatigue analysis applies.

5.1.5 Frequency domain fatigue estimation

Contrary to the time domain where the stress cycles are identified and counted from stress time history, in frequency domain the probability density function of stress cycles $p(\sigma_a)$ is used to estimate the expected value of the fatigue damage associated with a loading block. The density function of stress cycles $p(\sigma_a)$, which plays the key role in frequency domain fatigue estimation, is a function of moments of area of the stress PSD and can be adopted according to different methods. For more information the reader is referred to the literature *Mršnik et al.* (2013). Afterwards without taking the mean stress into account (i.e. $\sigma_m = 0$ in Eq. 5.26) and considering that Eq. 5.26 can generally be written in form of $N_f = C/\sigma_a^m$, fatigue can be expressed in terms of expected damage in time T under Palmgren-Miner rule (Eq. 5.25) (*Benasciutti and Tovo* (2005)):

$$E[D] = \frac{\nu_p T}{C} \int_0^{+\infty} \sigma_a^m \, p(\sigma_a) \, d\sigma_a, \tag{5.28}$$

in which ν_p is the expected number of peaks occur in the stress signal per unit of time and the number of cycles at certain stress levels, which are in the stress bin $[\sigma_{a_i}\ \sigma_{a_j}]$, is considered as follows:

$$N(\sigma_{a_x}) = \nu_p T \int_{\sigma_{a_i}}^{\sigma_{a_j}} p(\sigma_a)\, d\sigma_a\,, \quad \sigma_{a_i} \leq \sigma_{a_x} \leq \sigma_{a_j} \tag{5.29}$$

Studies showed that the probability density function of stress cycles $p(\sigma_a)$ suggested by Dirlik delivers well-estimated results, when compared to results of the reference time domain rainflow method (*Kemper and Feldmann* (2011); *Halfpenny* (1999)). Dirlik's function is an empirical expression and derived based on Monte Carlo simulations (*Dirlik* (1985)). Following, the proposed Dirlik's function is expressed in terms of moments of stress PSD, that is M_i:

$$p(\sigma_a) = \frac{1}{\sqrt{M_0}} \left[\frac{G_1}{Q} e^{\frac{-Z}{Q}} + \frac{G_2 Z}{R^2} e^{\frac{-Z^2}{2R^2}} + G_3 Z e^{\frac{-Z^2}{2}} \right] \tag{5.30}$$

where the i^{th} moment of area under the stress PSD, i.e. M_i, is defined by:

$$M_i = \int_0^\infty f^i\, G_{\sigma\sigma}(f)\, df \tag{5.31}$$

in which $G_{\sigma\sigma}(f)$ denotes the stress PSD at frequency f. The other parameters, used in Eq. 5.30, are given below:

$$G_1 = \frac{2(x_m - \alpha^2)}{1+\alpha^2} \qquad G_2 = \frac{1-\alpha-G_1+G_1^2}{1-R} \tag{5.32}$$

$$G_3 = 1 - G_1 - G_2 \qquad R = \frac{\alpha - x_m - G_1^2}{1-\alpha-G_1+G_1^2} \tag{5.33}$$

$$Q = 1.25\frac{(\alpha - G_3 - G_2 R)}{G_1} \qquad Z = \frac{\sigma_a}{\sqrt{M_0}} \tag{5.34}$$

$$\alpha = \frac{M_2}{\sqrt{M_0 M_4}} \qquad x_m = \frac{M_1}{M_0}\left(\frac{M_2}{M_4}\right)^{0.5} \tag{5.35}$$

Finally the expected peak numbers, used in Eq. 5.28, is also given in terms of the stress PSD moments i.e. $\nu_p = \sqrt{M_4/M_2}$.

5.1.6 Wind fatigue life estimation

In order to be able to apply Eq. 5.28, the stress PSD at the critical point of structure is required. The stress PSD can be obtained either from finite element model or directly from the measured stress data. The one from a finite element model is usually used in the simulation analyses, while the other is demanded in in-situ fatigue estimation. Since this contribution concentrates on the practical wind fatigue estimation, the latter is dealt with. For this purpose one method could be extraction of the the stress response PSD from continuous measured stress data for example over one year, similar to the rainflow time domain approach to cycle counting. However the introduced method in this study is frequency fatigue estimation from the discontinuous/sparse measured response (stress) data. It means that the continuous record of stress response is not available, but instead a relatively lower number of ten-minute records at different mean wind speed over one year exists.

According to the following expression one year expected fatigue damage can be computed in frequency domain (*Benasciutti and Tovo* (2005); *Kemper and Feldmann* (2011)):

$$E[D] = \sum_{i}^{n_d} \left[\frac{T_{1\,year}}{T_{ref}} \frac{\sigma^m}{C} \int_0^{+\infty} \int_0^{\bar{V}_{Tar}} \sqrt{\frac{M_4(\bar{V})}{M_2(\bar{V})}}\, p(\sigma_a, \bar{V})\, f(\bar{V})\, d\bar{V}\, d\sigma_a \right] f_{d_i} \Delta d_i \tag{5.36}$$

where $f(\bar{V})$ is the mean wind probability density function, usually of type of Weibull distribution function, derived from the mean wind histogram data. The mean wind speeds are calculated with respect to time period T_{ref} and the maximum mean wind speed (target speed) assumed to be $\bar{V}_{Tar}$. The summation accounts for adding up the damages corresponding to winds that blow from different directions. Therefore f_{d_i} denotes the normalized probability of blowing wind in the direction spacing i, whose angular length equals $\Delta d_i = 2\pi/n_d$. The number of identical angular spacings is n_d.

An innovative method is introduced in this study for evaluation of Eq. 5.36. The first link to this method is that the wind speed data is classified by the wind direction spacing and mean wind speed (as mentioned in Sec. 5.1.2.2). The advantage of this classification is that firstly the expected damage associated with each wind direction can be evaluated separately. Secondly in each direction the expected damage corresponding to a loading block can be calculated for the duration T_{ref} with mean wind speed $\bar{V}_{T_{ref}}$ and then being accumulated over one year by means of the mean wind speed probability density function, which returns the relative time duration of different mean wind speeds. As a result the stress PSD moments $M_i(\bar{V})$ and consequently the probability density function of stress amplitude cycles cycles $p(\sigma_a)$ should be attributed to mean wind speed as well. Up to this stage, the functions that express $M_i(\bar{V})$ in terms of mean wind speeds are unknown.

The second link in the introduced method reveals how to achieve the unknown functions for finding the values of moments of stress PSD in terms of mean wind speed. Attention is drawn to the fact that the moments of stress PSD are functions of stress response PSD. The PSD of the stress response at a point p of an n dofs system, $G_{\sigma\sigma}(\omega) = 2S_{\sigma\sigma}(\omega)$, can be generally expressed, as follows (*Mršnik et al.* (2013); *Halfpenny* (1999)):

$$S_{\sigma\sigma}(\omega) = \sum_{i}^{n} \sum_{j}^{n} H_{\sigma_i}(\omega) H_{\sigma_j}(-\omega) S_{f_i f_j}(\omega) \tag{5.37}$$

where $H_{\sigma_i}(\omega)$ and $H_{\sigma_j}(\omega)$, which are the structure's properties, denote the stress response transfer functions that relate stress at point p respectively to the wind loads at dof i and j. $S_{f_i f_j}(\omega)$ is the ij^{th} element of wind load PSD matrix. An element of wind load PSD matrix is dependent on the wind speed at the reference point with second order of power and on the element of wind speed PSD matrix (eq. 5.22). An element of wind speed PSD matrix is in turn function of mean wind speed at the reference point, of second order of power (see eq. 5.21). Consequently the moments of stress PSD are functions of mean wind speed of fourth order. According to Hooke's law for a structure experiencing deformations in linear elastic region, the stresses are derived from deformations by linear mathematical operations. Civil engineering structures are usually designed to function linearly under target loads and it is common in literature to assume linear elastic behavior of material for structures fatigue estimation (*e.g. see Jia* (2011)). Hence the relationship between the moments of stress PSD and the mean wind speed will be of fourth order of power in the linear region of deformations.

The turbulence transport depends on several factors. Wind speed is one of the dominant factors among others. However at the very low wind speeds the local mechanisms, like heat flux in the site, are more influential on the turbulence transport than wind speed. As a result, there is still turbulence at those low wind speeds, which excites the structure, while is not observed by mean wind speed. This fact is illustrated in Fig. 5.1, where the turbulence intensity increases disproportionately in the lower wind speed (say less than $1.5\,m/s$). This leads to the fact that the response indicators, such as standard deviation or moments of strain PSD etc, do not tend to zero in the vicinity of zero mean wind speed. Consequently, the curve fitting model, which applies better to the moments of strain PSD is a fourth order binomial of form $M_i(\bar{V}) = a_i \bar{V}^4 + b_i$, in which the constants a_i and b_i are found by means of curve fitting and b_i accounts for the non-zero values in the vicinity of zero mean wind speed.

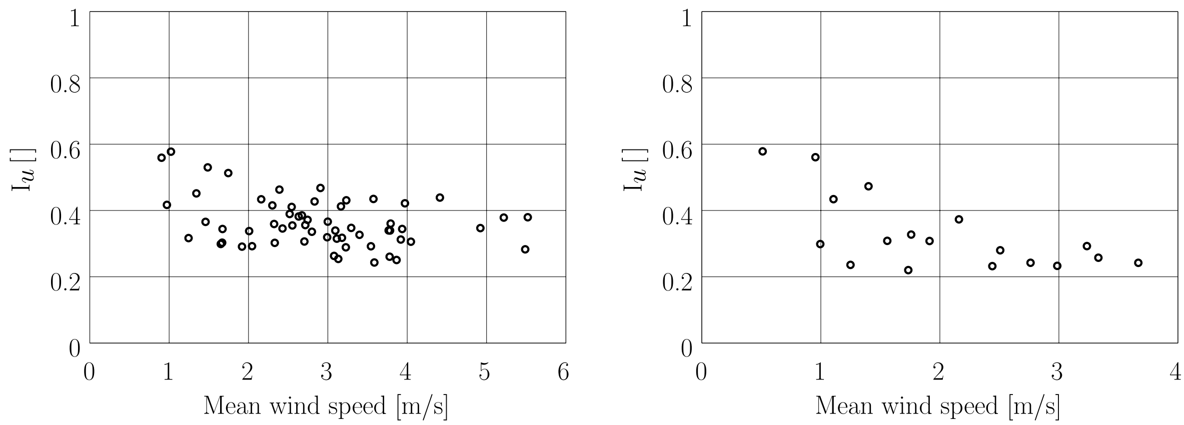

(a) Wind direction WSW (b) Wind direction W

Figure 5.1: The seasonal turbulence intensity

The above mentioned explanation also holds for the responses standard deviation, but rather in that case the algebraic model is of second order of power.

5.1.7 Results of method application to real measurement data

In this section firstly the details of the setup for wind speed and structural response measurement are described. Then the analysis of wind speed data is provided and afterwards the results corresponding to analyses of displacement response standard deviation and threshold passage counts are presented. Finally the application of the introduced method to spectral wind fatigue analysis is dealt with.

5.1.7.1 Measurement setup description

The measurement is carried out on a guyed mast which serves as a weather station for meteorological observations in the Hydrological Open Air Laboratory in Lower Austria (*Blöschl et al.* (2016)). The structure is 9.1 m (30 ft.) tall and consists of tubular elements (Fig. 5.2).

The wind speed is measured continuously over one year with a frequency of ten samples per second by means of sonic anemometers in three perpendicular directions. Due to the technical restrictions the anemometer was installed at the height of three meters above the ground. The wind speed data corresponding to two perpendicular horizontal directions, namely in *x*-*y* plane (see Fig 4.1a), are used in this study, by which the relative wind angle can be instantaneously identified too.

The structural acceleration response is measured at several points on the structure, among which the one on the top of the mast is used in this study. The acceleration response is measured in two perpendicular horizontal directions by capacitive accelerometers, suitable for registering the relatively low frequency vibrations similar to that which occurs due to wind-induced excitation, with a sampling

Figure 5.2: Picture of structure, on which the wind speed and structural response is measured

rate of 100 Hz. The acceleration measurement is triggered automatically every 18 hours and the data was recorded for 30 minutes, then the middle ten-minute data was adopted for response analysis. The total amount of measured data, due to the gaps between consecutive triggering, is far less than the case of continuous measurement.

5.1.7.2 Wind speed data analysis

From the horizontal components of the wind speed data, the ten-minute mean value and standard deviation of the resultant wind speed were computed. The mean wind speed was then classified according to the blowing directions. For this purpose 16 wind directions, each with $\Delta d_i = 2\pi/16$ degrees, were considered. Fig. 5.3 shows the normalized probability density of mean wind directions f_{d_i} in polar coordinates, which is calculated as follows:

$$f_{d_i} = \frac{n_i}{n_{Tot}\,\Delta d_i} \tag{5.38}$$

in which n_i and n_{Tot} denote the number of mean wind speed located in angular spacing i and the total number of ten minutes mean wind data over a year, respectively. Hereafter the analysis of results corresponding to directions W, WSW is focused on, as either the probability of blowing in other directions is negligible or their wind speeds are so low such that they do not excite the structure considerably. In Table 5.1 the relative values of probability density of wind directions, i.e. $F_{d_i} = n_i/n_{Tot}$ are presented.

The next step is to process the wind speed data. As the sonic anemometer devices can measure at even very low speed winds speed and since those low speed winds correspond to local wind mechanisms, the mean wind speed lower than 0.8 m/s were removed from the wind data. The histogram of the mean

Table 5.1: Probability density of wind directions

	N	NNE	NE	ENE	E	ESE	SE	SSE
F_{d_i} (%)	2	4	8	6	5	5	2	1
	S	SSW	SW	WSW	W	WNW	NW	NNW
F_{d_i} (%)	2	3	9	24	15	7	4	3

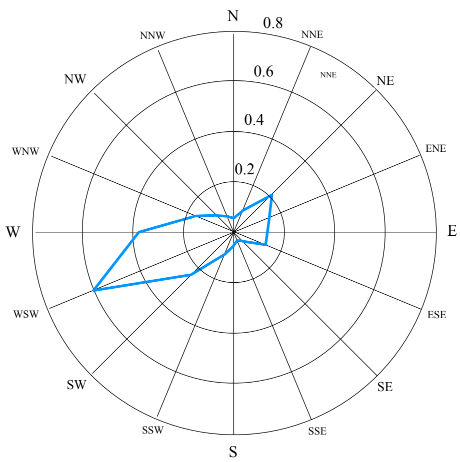

Figure 5.3: One year distribution of mean wind speeds according to blowing direction

wind speed in each direction spacing can then be generated. The mean wind speed histogram is used to estimate the parameters of Weibull distribution, given below (*Garcia et al.* (1998); *Seguro and Lambert* (2000); *Dorvlo* (2002)):

$$P(\bar{V}) = \frac{k}{c}\left(\frac{\bar{V}}{c}\right)^{k-1} exp\left[-\left(\frac{\bar{V}}{c}\right)^{k}\right] \tag{5.39}$$

in which c and k are the scale and shape parameters of Weibull distribution. The histograms and fitted Weibull distributions corresponding to major wind directions are represented in Fig. 5.4.

5.1.7.3 Wind stochastic response and fatigue damage analysis

The acceleration horizontal components corresponding to the fluctuating part of the wind response, in other words $x'(t)$ in Eq. 5.19, on the top of the structure is measured. Each time series of ten-minute triggered acceleration data (see section 5.1.7.1) is tagged by its associated ten-minute mean wind speed. The acceleration signals are decimated by factor 7, which consequently yields to the new measurable upper bound of 7.1 Hz with respect to the Nyqvist frequency. The displacement response from the acceleration is derived by double integration in frequency domain (*Brandt and Brincker* (2014)). In order to prevent the drift phenomenon due to integration, every time before integration the signal was windowed and also passed through high-pass Butterworth filter with cut-in frequency of 0.2 Hz.

Firstly it is dealt with the standard deviation of displacement response as an important stochastic response indicator. As it was described in section 5.1.2.2, the goal is to find a second order polynomial

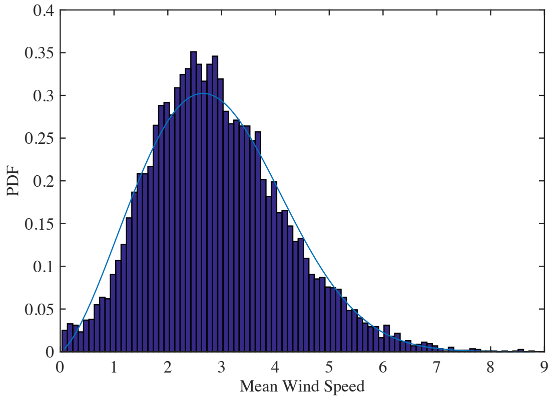

(a) Wind direction WSW, Weibull parameters: $c = 3.283$, $k = 2.45$

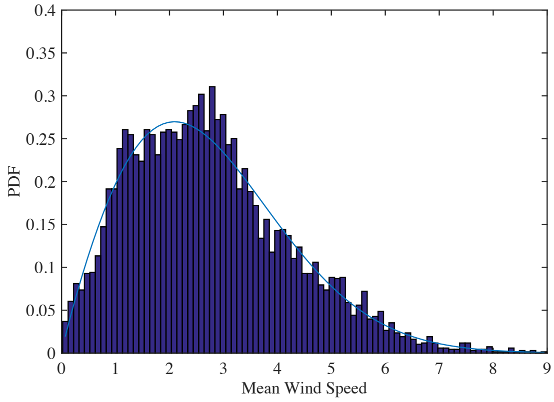

(b) Wind direction W, Weibull parameters: $c = 3.088$, $k = 1.910$

Figure 5.4: Mean wind speed histogram and fitted Weibull distribution

from sparse measurement data, which returns the response standard deviation at any mean wind speed. Figure 5.5 represents the plot of standard deviation of displacement components versus the mean wind speed as well as the fitted second order polynomial according to the triggered data over one year. This figure corresponds to measured data in wind direction WSW. The R-squared measure of goodness of fit (R^2) in x and y direction is respectively 0.60 and 0.62.

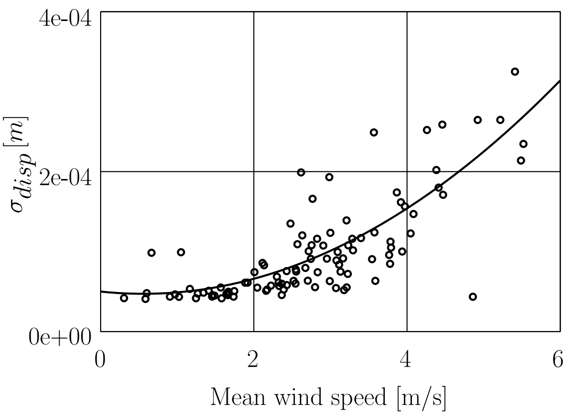

(a) x component

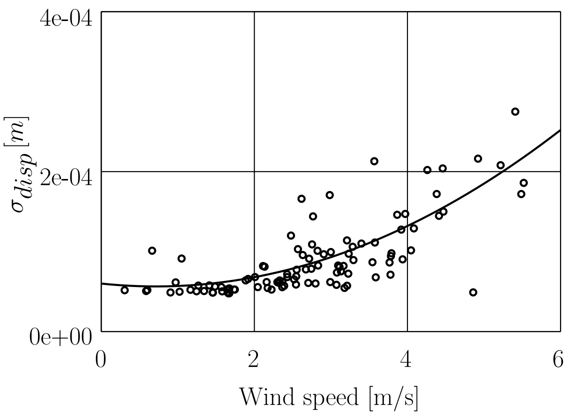

(b) y component

Figure 5.5: One year scatter and fitted second order polynomial corresponding to standard deviation of horizontal displacement response components

Figures 5.6 provides the decomposed seasonal subsets of x component one year data in wind direction WSW, corresponding to Fig. 5.5a. The seasonal subsets are called winter (October-March) and summer data (April-September). The R^2 values associated with fitted second order polynomial for winter and summer displacement standard deviation are respectively 0.83 and 0.54. The significantly smaller R^2 for summer data is due to large dispersion of data, which states that unlike winter data, relationship between mean wind data and displacement response standard deviation is weak.

The structural behavior, other than small changes in natural frequencies does not change substantially over a year, thus to find the reason for the above mentioned weakness of the relationship between mean

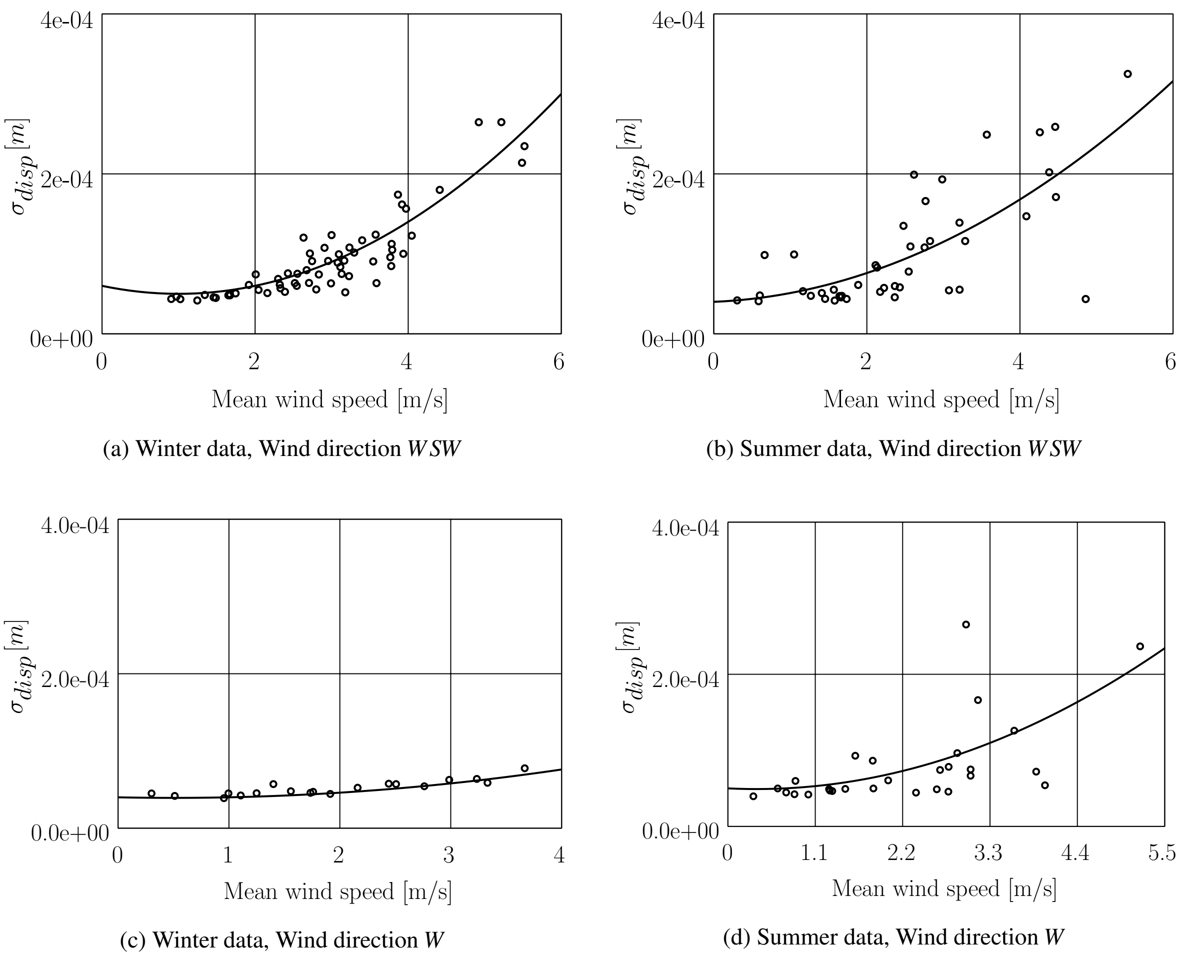

(a) Winter data, Wind direction *WSW*

(b) Summer data, Wind direction *WSW*

(c) Winter data, Wind direction *W*

(d) Summer data, Wind direction *W*

Figure 5.6: Seasonal scatter and fitted second order polynomial corresponding to standard deviation of displacement response *x* components

wind speed and response data in summer, the wind properties should be inspected. Predominantly the wind blows from WSW and W, this means the wind in these directions is generated by the large scale wind mechanisms in the region, where the structure is located. As mentioned before the structure is located between the farms. As a result in summer the large scale mechanism is influenced by the local airflow, especially locally generated winds due to convection effects and changes in surface roughness by vegetation. In this regard the turbulence intensity for the resultant of the horizontal ten-minute mean wind speeds was according to the following equation calculated:

$$I_u = \frac{\sigma_u}{\bar{V}} \tag{5.40}$$

where σ_u is the ten-minute standard deviation of the resultant horizontal mean wind speed. Figures 5.7 represents the plots of winter and summer wind turbulence intensity for wind direction WSW, which evidently shows that in summer the turbulence intensity, unlike in winter, does not follow a constant trend. Consequently it is wise and conservative to select the relationships between wind mean speed and response indicators from winter data and utilize them for the whole year analysis. Consequently, hereafter just the winter results are represented. By this, the amount of data, which must be processed is considerably reduced, too.

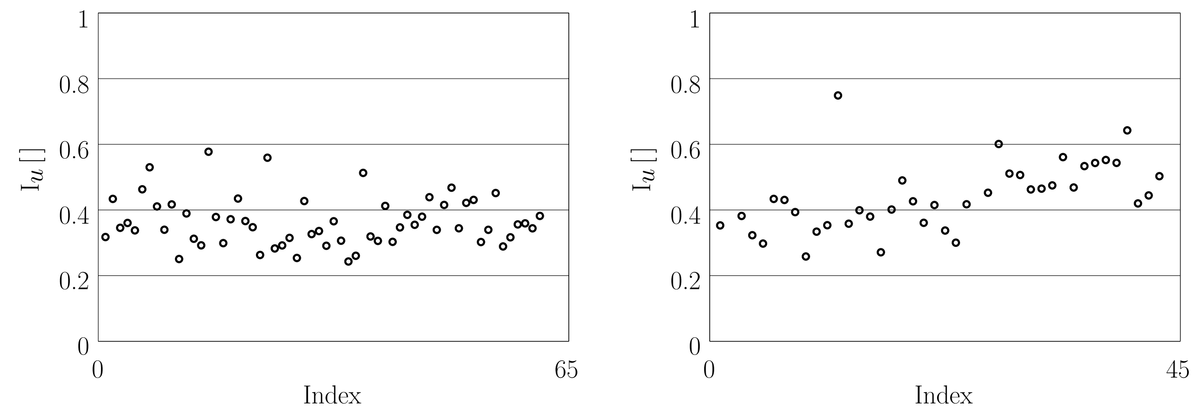

(a) Winter data

(b) Summer data

Figure 5.7: Seasonal turbulence intensity

The next response indicator, which is dealt with in this contribution, is the number of threshold passages $n_{d_{Th}}(\bar{V})$, whose relationship with mean wind speed is investigated. To the knowledge of the authors, this relationship has not been mathematically expressed yet. However it possible to find this relationship statistically by means of observation. For this purpose the resultant of x and y displacement components at each time step is computed and the number of data points, which are larger than the displacement threshold of $d_{Th} = 1e-4\ m$ is counted. It has been observed that the relationship between threshold passage counts and mean wind speed is linear. Thereby this relationship can be expressed by a line whose equation can be derived by curve fitting. For instance figure 5.8 provides the data of displacement threshold passage counts and the corresponding fitted lines with R^2 values 0.81 and 0.74 for directions WSW and W, respectively.

Once the mathematical expression of displacement threshold passage counts in terms of mean wind speed is known, the expected value of probability of threshold passage over one year, i.e. $P_{d_{1\,year}}$, can readily be calculated too. To this end, the expected probabilities of passage threshold are computed similar to Eq. 5.36 for the two predominant wind directions WSW and W:

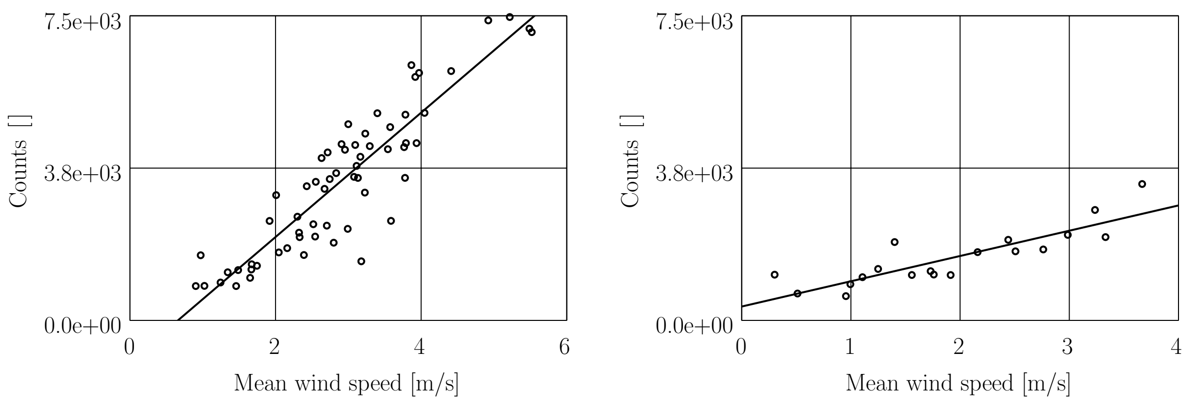

(a) Wind direction WSW (b) Wind direction W

Figure 5.8: Winter scatter and fitted trend-line corresponding to displacement threshold passage count

$$E[P_{d_{1year}}] = \sum_{i=1}^{2}\left[\int_0^{\bar{V}_{Tar}} \frac{n_{d_{Th}}(\bar{V})}{n_{10min}} f(\bar{V})\,d\bar{V}\right] f_{d_i}\Delta d_i \tag{5.41}$$

in which $n_{10min} = 600 * \nu_s$ is the number of data points in 10 minutes (ν_s denotes data sampling rate). By mean of the above equation, the total expected value of probability of threshold passage over one year was found to be $P_{d_{1year}} = 10.97\%$. In Table 5.2, the details for computations regarding Eq. 5.41 is provided.

Table 5.2: Computation details of one year threshold passage probability

Wind direction	f_{d_i} (%)	$n_{d_{Th}}(\bar{V})$	$P_{d_{1year_i}}$ (%)
WSW	60.73	$1531\bar{V} - 1008.9$	8.94
W	38.24	$622.3\bar{V} + 341.5$	2.03

In the last part, the results applicable to fatigue damage estimation are presented. It was earlier explained in section 5.1.6, that wind fatigue damage can be estimated from discontinuous/sparse measured response (stress) data by means of Eq. 5.36, provided that one can find the mathematical expressions of moments of stress PSD (i.e. $M_i(\bar{V})$) in terms of mean wind speed. In the same section it was discussed that these expressions are in form of $M_i(\bar{V}) = a_i\bar{V}^4 + b_i$.

Once such expressions exist, the expected damage can be computed by implementing a numerical integration scheme to evaluate Eq. 5.36, as follows: Above all, the increment rates of mean wind speed $d\bar{V}$ and stress amplitude $d\sigma_a$ are selected. Then at each mean wind speed bin, the values of $M_i(\bar{V})$ are obtained from the equation of the fitted curves (section 5.1.6). It should be noted that different stress amplitudes occur at a certain mean wind speed bin. When $M_i(\bar{V})$ are known, for each of stress amplitude bins, which occur at a certain mean wind speed bin, the value of stress amplitude cycles probability density function, $p(\sigma_a)$, can be computed. As a result, a vector of the numerical values of the integrand, associated with the representative stress amplitudes of the bins, at each mean wind speed bin is evaluated. Afterwards the integration can be numerically evaluated by means of the matrix of integrand values corresponding to the stress amplitude and mean wind speed bins. By this the expected damage of all predominant wind directions can be summed.

Unfortunately in this work the measured stress data is not available. However the introduced approach can be qualitatively evaluated for displacement data, with respect to the point that for structures with linear elastic behavior, the stress field is achieved from displacements linearly. As a result it is assumed that the displacements data is in this sense (its relationship with mean wind speed) equivalent to stress responses data. Then the relationship between mean wind speed and moments of displacement response PSD over oner year is sought. To this end, the displacement-based values of $M_i(\bar{V})$ associated with the ten-minute triggered data over one year were numerically evaluated from the definition $M_i = \int_0^\infty f^i G_{\sigma\sigma}(f)\,df$. In order to find the values of $M_i(\bar{V})$, the displacement response PSDs, $S_{zz}(f)$ or its stress counterparts $G_{\sigma\sigma}(f)$, can be obtained directly from measured response data for instance through *Welch* method and then the integrals are computed numerically. Figure 5.9 represents the moments of response PSD versus mean wind speed and the corresponding fitted curves of form $M_i(\bar{V}) = a_i\bar{V}^4 + b_i$, over one year. From the fitted curves, the values of stress PSD moments for any desired ten-minute data with mean wind speed $\bar{V}$ can be achieved.

Table 5.3 provides the R^2 values corresponding to fitted curves in Figure 5.9.

Table 5.3: R^2 measure of goodness of fit

Wind direction	M_0	M_1	M_2	M_4
WSW	0.83	0.82	0.82	0.82
W	0.94	0.94	0.93	0.93

5.1.8 Conclusion

In this contribution the wind stochastic response of a real structure from sparse measurement data over one year was analyzed. The main focus was drawn to the point of, how the mean wind speed data can be of benefit, in order to fill the structural response measurement gaps. For this purpose the wind speed was measured continuously over one year and predominant wind directions as well as mean wind probability density functions based on ten-minute averaging were obtained. The ten-minute structural responses were recorded according to an 18-hour automatic triggering within one year. Then every ten-minute data was tagged by its corresponding mean wind speed.

It was comprehensively discussed how to recover the structural response indicators associated with those unmeasured ten-minute time intervals between two consecutive triggering. In this contribution two response indicators, i.e. displacement response standard deviation and threshold passage counts, were targeted. These indicators are important for the sake of structural vibration control under long term random excitations like wind. It was shown that from the sparse response data the mathematical relationship between response indicator and mean wind speed data can be achieved.

In this study an efficient procedure for frequency domain wind fatigue estimation was also introduced. To this end merely the moments of stress PSD are required, in order to calculate the density function of stress amplitude cycle counts. It was described that in the presence of wind probability density function associated with each predominant blowing direction, the values of the moments of stress PSD at different mean wind speeds corresponding to unmeasured ten-minute time intervals can be interpolated from the sparse measurement data. Once the moments of stress PSD are known, the expected one year damage due to wind vibration can readily be calculated. Since in this work the measured strain/stress data did not exist, the introduced approach for estimation of expected one year wind fatigue damage was qualitatively evaluated for displacement data.

The mathematical relationships between mean wind speed and displacement response standard

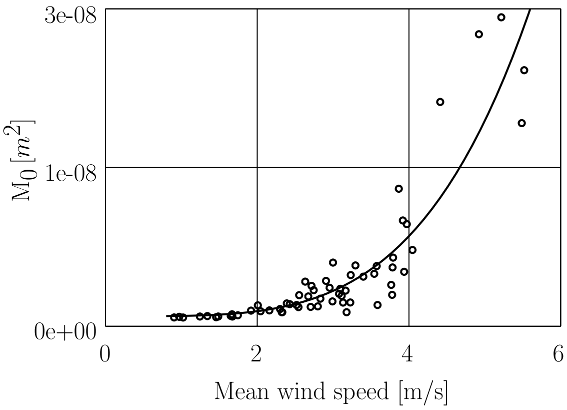

(a) M_0, Wind direction WSW

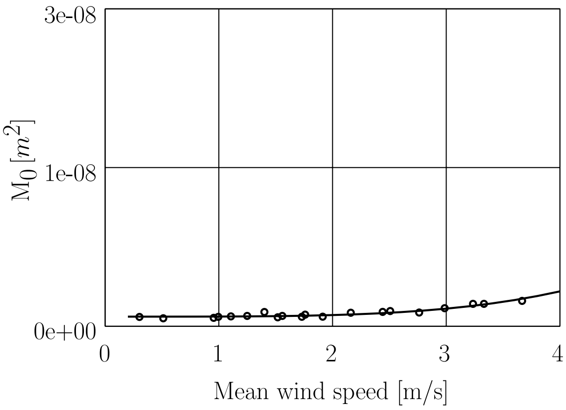

(b) M_0, Wind direction *W*

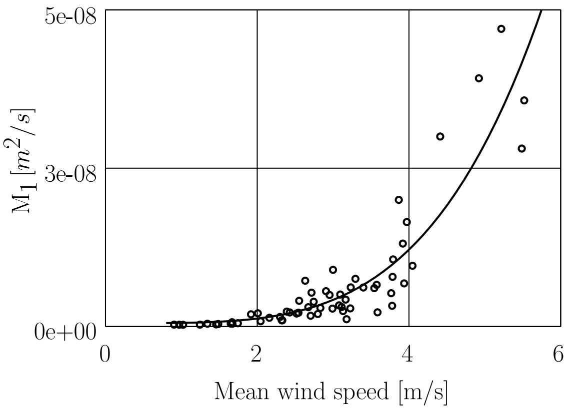

(c) M_1, Wind direction WSW

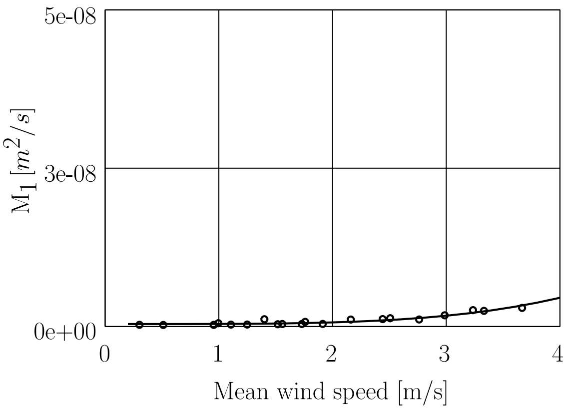

(d) M_1, Wind direction *W*

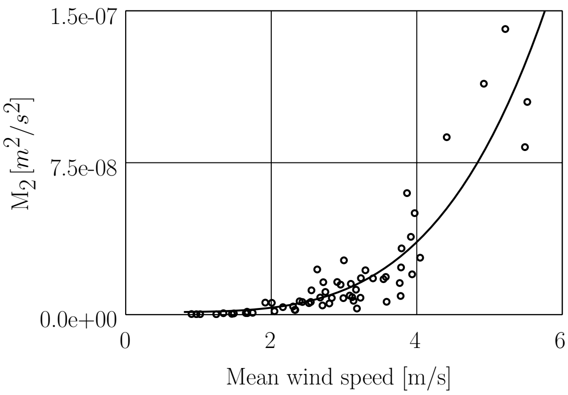

(e) M_2, Wind direction WSW

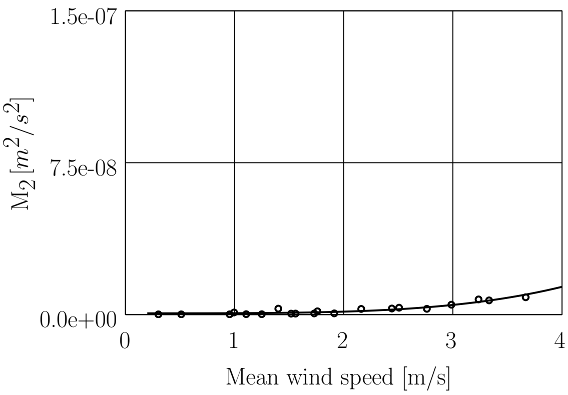

(f) M_2, Wind direction *W*

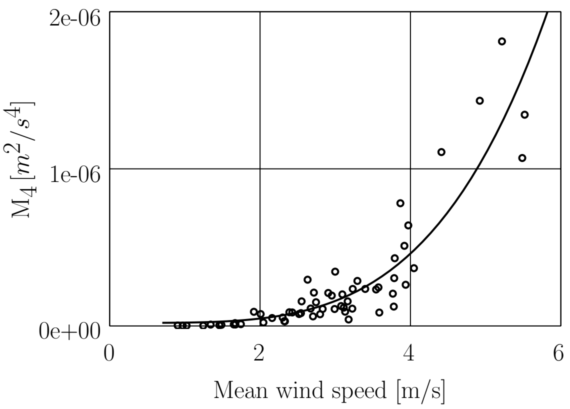

(g) M_4, Wind direction WSW

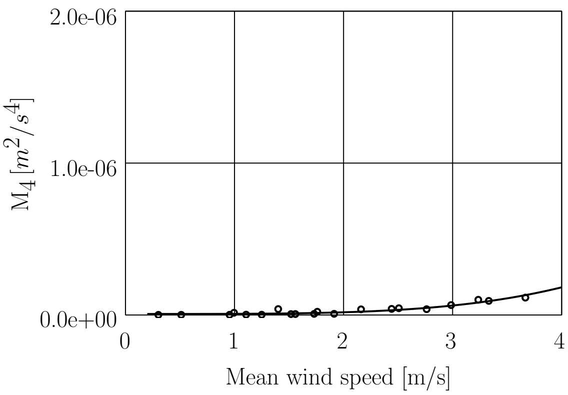

(h) M_4, Wind direction *W*

Figure 5.9: Winter scatter and fitted second order polynomial corresponding to displacement displacement PSD moments

deviation as well as mean wind speed and moments of stress (displacement) PSD were selected according to the presented theoretical background.

5.2 A new model order reduction strategy adapted to nonlinear problems in earthquake engineering

Earthquake dynamic response analysis of large complex structures, especially in the presence of nonlinearities, usually turns out to be computationally expensive. In this paper, the methodical developments of a new model order reduction strategy (MOR) based on the proper orthogonal decomposition (POD) method as well as its practical applicability to a realistic building structure are presented. The seismic performance of the building structure, a medical complex, is to be improved by means of base isolation realized by frictional pendulum bearings. According to the new introduced MOR strategy, a set of deterministic POD modes (transformation matrix) is assembled, which is derived based on the information of parts of the response history, so-called snapshots, of the structure under a representative earthquake excitation. Subsequently, this transformation matrix is utilized to create reduced-order models of the structure subjected to different earthquake excitations. These sets of nonlinear low-order representations are now solved in a fractional amount of time in comparison to the computations of the full (non-reduced) systems. The results demonstrate accurate approximations of the physical (full) responses by means of this new MOR strategy if the probable behavior of the structure has already been captured in the POD snapshots.

5.2.1 Introduction

The evaluation of the response history of a structure in the time domain is one of the main topics in earthquake engineering and structural dynamics. It is common practice to create simple structural models, e.g. multistory shear frames, which should be able to describe the structural behavior and peculiarities of the real structure. This approach leads to useful results for the investigation of rather simple and uniform structures in order to come to meaningful engineering decisions regarding structural resistance. On the contrary, the analysis of complicated systems can require the application of nonlinear high-order systems, as a characterization by a low dimensional structural model could lead to an oversimplification, i.e. important motion patterns could be ignored. Therefore, an effective strategy is to obtain a set of a low number of "important" equations of motion that approximates the high-dimensional nonlinear dynamical system as accurately as possible, that is, model order reduction (MOR).

The solution of the nonlinear set of equations of motion in the time domain is realized by numerical algorithms, which require computational effort if the number of degrees of freedom (DOF) is high. Even the response calculation of linear systems can be expensive, as a factorization of the stiffness matrix is necessary to solve the eigenvalue problem and calculate the natural modes of vibration.

An alternative is to replace a high-dimensional nonlinear set of equations of motion with a reduced set, providing the main dynamic behavior of the system to reach the required level of accuracy. MOR methods are used in many fields of research, where high-dimensional systems are dealt with. Some review papers of MOR, especially for structural dynamic applications, are presented by Rega and Troga (*Rega and Troger* (2005)) and Koutsovasilis and Beitelschmidt (*Koutsovasilis and Beitelschmidt* (2008a)). The classical but also effective method of modal truncation is well-known in the field of earthquake engineering, which is however mainly applicable to linear systems.

This paper concentrates on a new MOR strategy based on the proper orthogonal decomposition (POD) method. The POD provides a low dimensional uncorrelated description (basis vectors), by which a high-dimensional correlated process, e.g. structural response, is spanned. Firstly, it was used as a statistical formulation in the papers of Kosambi (*Kosambi* (1943)), Karhunen (*Karhunen* (1947)) and (Loeve *Loeve* (1946)).

The first paper regarding the field of structural dynamics was written by Cusumano et al. (*Cusumano and Kimble* (1993)) in the early 1990's, who presented an experimental study of dimensionality in an elastic impact oscillator. In the papers of Feeny and Kappagantu (*Feeny and Kappagantu* (1998), *Kappagantu and Feeny* (1999)) a relation of the proper orthogonal modes to normal modes of vibration is investigated. Then they used the POD as they so call optimal modal reduction and exploit the benefits of the application of these modes in comparison to the linear natural modes. Furthermore, Kappagantu and Feeny (*Kappagantu and Feeny* (2000a), *Kappagantu and Feeny* (2000b)) investigated the dynamics of an experimental frictionally excited beam and they verified that the proper orthogonal modes are efficient in capturing the dynamics of the system. Liang et. al. (*Liang et al.* (2002)) discuss the realizations of the POD, i.e. Karhunen-Loeve Decomposition, principal component analysis and singular value decomposition and compare these three methods. Kerschen and Golivani (*Kerschen and Golivani* (2002)) analyze the physical interpretation of the POD modes and its relation to the singular value decomposition and they investigated POD based on auto-associative neural networks (*Golivani* (2003)).

The necessity to describe a high dimensional set by a small set of equations of motion, i.e. MOR, has aroused interest mainly in the last two decades in the field of earthquake engineering (*Qu et al.* (2001), *Schemann and Smith* (1998)). Krysl et al. (*Krysl et al.* (2001)) deal with nonlinear MOR in FE analysis. They introduce the POD for low-order representations and point out the benefits concerning numeric integration, optimality and robustness. Tubino et. al. (*Tubino et al.* (2003)) investigated the seismic ground motion of the support points of a structure and classify the POD as a very efficient tool to simulate multi-variate processes. Bucher (*Bucher* (2001)) examined the stabilization of explicit time integration methods for analysis of nonlinear structural dynamics by modal reduction. Gutierrez and Zaldivar investigated in *Gutierrez and Cela* (1998) how to handle the stability problem of explicit time integration by modal truncation methods more related to problems in earthquake engineering and structural dynamics and they applied the Karhunen-Loeve Decomposition, which is formally identical to the POD analysis, to capture the essential characteristics of nonlinear systems and provide experimental examples conducted on a shaker table (*Gutierrez and Zaldivar* (2000)). Bamer and Bucher (*Bamer and Bucher* (2012)) developed a MOR strategy applying the POD method for transient excited structures resting on one-dimensional friction elements. This study presented a powerful combination of the POD and explicit time integration schemes.

The current work investigates the extension of the POD-based MOR strategy, which is applicable to nonlinear systems in contrast to the method of modal truncation. The new strategy pursues the following objective: a low number of deterministic nonlinear modes (i.e. set of POD modes) is determined that defines a representative characterization of the structural behavior. Therefore, due to the information content of the full (or a part of the) time response of the structure to one representative excitation a set of deterministic modes, i.e. POD modes, is evaluated. Subsequently, this set of modes is utilized to project the equations of motion of a structure under different earthquake excitations onto POD coordinates and thereafter an order truncation is performed in a similar manner to the application of modal truncation to linear systems. The presentation of the novel MOR approach is accompanied by an explanatory and illustrative example, which supports basic understanding and visual insight into the method as well as an application to a realistic building structure.

It is essential to demonstrate this new strategy and its advantages by means of a practical application. Related to the first explanatory example this application differs in complexity and the type of nonlinearities. The method is applied to the dynamic model of a realistic building structure. The building is erected on friction pendulum bearings for the sake of seismic isolation to minimize the transferred acceleration to the building during an earthquake. A three-dimensional dynamic model of the base isolated structure is derived by implementing the finite element model of the structure and the bi-directional friction pendulum systems. The paper then deals with the nonlinear dynamic model of the base-isolated structure. Thereafter, the new POD-based MOR strategy and the example of its practical application is provided. Finally, the results and conclusions are outlined.

5.2.2 Earthquake excitations

Within the presentation of the new strategy and the application to a realistic building structure, a set of six earthquake excitation records is chosen for the numerical demonstrations. The earthquake records are applied in fault-parallel and fault-normal directions. The excitation set includes the Bam earthquake (2003) in Iran and the following five representative events in California, US: Northridge Rinaldi (1994), Imperial Valley (1979), Landers (1992), Loma Prieta (1989), North Palm Springs (1986). Table 5.4 presents a list of the events taken from the Pacific Earthquake Engineering Research Center (PEER) (*Pacific Earthquake Engineering Research Center* (2016)). Fault-parallel is defined in x- and fault-normal in y-direction. Concerning the Bam event only a one-dimensional record is available, therefore, an excitation attack angle of 30 degrees with respect to the x-axis is chosen.

Event	year	location	n_t	T	d	M	PGA
Bam	2003	Iran	1995	19.95	-	6.6	7.16
Imperial Valley	1979	California / Huston Road	3905	39.05	10	6.5	4.79
Landers	1992	California / Barstow	4932	49.32	36	7.3	4.13
Loma Prieta	1989	California / Gilroy	2507	25.07	12	7.0	9.51
North Palm Springs	1986	California / Palm Springs	6009	60.09	6.7	6.0	9.99
Northridge Rinaldi	1994	California / Newhall	1200	12.00	6.7	6.7	5.23

Table 5.4: Earthquake excitation list; n_t $[-]$ number of time steps, T $[s]$ duration of the record, d $[km]$ distance from epicenter, M moment magnitude, PGA $[\frac{m}{s^2}]$ peak ground acceleration

5.2.3 Nonlinear model order reduction and the POD - mathematical formulation

The n-dimensional set of equations of motion of a structure with nonlinear material behavior excited by horizontal components of ground acceleration is expressed as (cf. *Chopra* (1995))

$$\mathbf{M}\ddot{\mathbf{x}} + \mathbf{C}\dot{\mathbf{x}} + \mathbf{R}(\mathbf{x}) = -\mathbf{M}\left(\mathbf{f_x}\ddot{x}_g + \mathbf{f_y}\ddot{y}_g\right) \ , \tag{5.42}$$

where $\mathbf{M}$ and $\mathbf{C}$ are mass- and damping square matrices of order n and $\mathbf{R}(\mathbf{x})$ is the nonlinear internal restoring force vector dependent on the displacement $\mathbf{x}$ with the dimension $n \times 1$. The right hand side of the set of equations of motion describes the earthquake excitation term, while $\ddot{x}_g$ and $\ddot{y}_g$ denote the ground acceleration in x- and y-direction and $\mathbf{f}_j, (j = x, y)$ are the influence vectors in the corresponding direction, that is,

$$\mathbf{f_x}(x_i) = 1 \ , \quad \mathbf{f_y}(y_i) = 1 \ , \quad i = 1 \ldots n \ , \tag{5.43}$$

at the global x and y DOF of all nodes, whereas the other components of $\mathbf{f_x}$ and $\mathbf{f_y}$ are zero. Thus, i describes the number of nodes of the FE discretized structure. This general approach indicates that in this paper the ground acceleration in the corresponding direction, i.e. x- and y-direction, is equal in all structural support points. In the following equations the term on the right hand side of the set of equations of motion (5.42) is denominated by $\mathbf{F}(t)$, which has the unit of a force.

Nonlinear systems, as they are depicted in Equation (5.42), have generally to be solved by the application of a numerical algorithm, that is, a step by step procedure in the time domain in order to obtain the response of the structure as a function of time. The application of a numerical method inevitably leads to the existence of computational effort if n is a large number. Therefore, the approximation by a low-dimensional description of the system seems to be useful, namely the application of MOR.

The main goal of MOR techniques is primarily to define a transformation matrix $\mathbf{T} \in \mathbb{R}^{n\times m}$, $m \ll n$ to approximate the displacement vector $\mathbf{x} \in \mathbb{R}^n$ through a reduced coordinate vector $\mathbf{q_r} \in \mathbb{R}^m$ by the relation (cf. Koutsovasilis and Beitelschmidt *Koutsovasilis and Beitelschmidt* (2008b))

$$\mathbf{x} = \mathbf{T}\mathbf{q_r} \,, \tag{5.44}$$

such that the dynamic properties of the system are preserved and the error is small. The notation of the variable $m \in \mathbb{N}$ is the dimension of the reduced subspace.

The projection of the nonlinear system defined by Equation (5.42) onto that subspace leads to another second-order ordinary differential equation (cf. Koutsovasilis and Beitelschmidt *Koutsovasilis and Beitelschmidt* (2008b))

$$\mathbf{m_r}\ddot{\mathbf{q}}_\mathbf{r} + \mathbf{c_r}\dot{\mathbf{q}}_\mathbf{r} + \mathbf{r} = \mathbf{f_r} \,, \tag{5.45}$$

where $\mathbf{m_r} = \mathbf{T^T M T}$, $\mathbf{c_r} = \mathbf{T^T C T} \in \mathbb{R}^{m\times m}$ are mass- and damping matrix and $\mathbf{f_r} = \mathbf{T^T F}(t) \in \mathbb{R}^{m\times 1}$ is the force vector in the reduced subspace. It should be noted that the reduced system matrices $\mathbf{m_r}$ and $\mathbf{c_r}$ are generally not diagonal. The vector of the restoring forces in the reduced subspace is

$$\mathbf{r} = \mathbf{T^T R}(\mathbf{x}) = \mathbf{T^T R}(\mathbf{T}\mathbf{q_r}) \,. \tag{5.46}$$

Consequently, one necessity of nonlinear MOR is the evaluation of the vector of the restoring forces in the physical (full) coordinate at every time step.

Modal truncation is a widely-used tool and an effective method for order reduction of linear systems in the field of earthquake engineering. An accurate approximation of the response history is achieved by applying a small number of lower structural modes proportional to the number of DOF. An early and successful application of modal truncation to problems involving small local nonlinearities is presented in *Wilson* (1990) and *Ibrahimbegovic and Wilson* (1992). In this work, the objective is to find a new strategy that is applicable to nonlinear systems in a similar manner to modal truncation. The approach is to define a set of deterministic modes that can be evaluated from the information of an existing response history of the structure. Consequently, this set of modes contains nonlinear motion patterns if the structure shows nonlinear response behavior to the excitation.

The proposed strategy is established based on the theory of the POD method. Generally, the POD (c.f. *Liang et al.* (2002), *Chatterjee* (2000), *Holmes et al.* (1996)) is a straightforward approach to obtain a low-dimensional uncorrelated process from a correlated high dimensional or even infinite-dimensional process. Holmes et al. (*Holmes et al.* (1996)) examined the theoretical background of the POD and its properties profoundly. In the following, the mathematical basics of the POD are discussed shortly, but as the paper is more targeted to the strategic approach in earthquake engineering, the attention to the mathematical background and the numerical problems are limited to an essential minimum.

The aim of the POD is to find a set of ordered orthonormal basis vectors in a subspace so that samples in a sample space are expanded in terms of l basis vectors in an optimal form. This means that the POD is able to find an orthonormal basis, which describes an observation vector in a subspace better than any other orthonormal basis can do. A measure for this problem is the mean square error (cf. Qu *Qu* (2004))

$$E\left\{\|\mathbf{x} - \mathbf{x}(l)\|^2\right\} \leq E\left\{\|\mathbf{x} - \hat{\mathbf{x}}(l)\|^2\right\} \,, \tag{5.47}$$

where $\mathbf{x} \in \mathbb{R}^{n \times 1}$ is the random vector, $\mathbf{x}(l)$ is the approximation of this random vector in an l-dimensional POD subspace and $\hat{\mathbf{x}}(l)$ is the approximation of the random vector by any other possible orthonormal basis. Therefore, the random vector can be expressed as (cf. Qu *Qu* (2004))

$$\mathbf{x} = \boldsymbol{\Phi}_{\boldsymbol{p}} \mathbf{q_p} \; , \quad \boldsymbol{\Phi}_{\boldsymbol{p}} = [\varphi_{\mathbf{p,1}}, \varphi_{\mathbf{p,2}}, ..., \varphi_{\mathbf{p,s}}] \quad \text{and} \quad \mathbf{q_p} = [q_{p,1}, q_{p,2}, ..., q_{p,s}] \; , \tag{5.48}$$

where $\varphi_{\mathbf{p,i}}$ are the POD modes and $q_{p,i}$ denote the coordinates in the POD subspace and s is the number of realizations of the random vector (also called snapshots). This leads to an optimization problem with the following objective function (cf. Qu *Qu* (2004))

$$\varepsilon^2(l,t) = E\left\{\|\mathbf{x} - \mathbf{x}(l)\|^2\right\} \rightarrow min \tag{5.49}$$

subject to the orthonormality condition (cf. Qu *Qu* (2004))

$$\varphi_{\mathbf{p,i}}^{\mathbf{T}} \varphi_{\mathbf{p,j}} = \delta_{ij} \; (i,j = 1,2,...,s) \; . \tag{5.50}$$

The transformation into the l-dimensional POD subspace is a truncation of the first l lower POD modes (cf. Qu *Qu* (2004))

$$\mathbf{x}(l) \approx \boldsymbol{\Phi}_p q_p \; , \quad \boldsymbol{\Phi}_p = [\varphi_{\mathbf{p,1}}, \varphi_{\mathbf{p,2}}, ..., \varphi_{\mathbf{p,l}}] \; , \quad l < s \ll n \; . \tag{5.51}$$

5.2.4 The new approach

In this section the reader's attention is drawn to the methodical approach. Therefore, a simple and illustrative two-dimensional structural example subjected to a set of ground motions goes along with the presentation of the new MOR strategy. Earthquake excitation records are presented in section 5.2.2, respectively in Table 5.4.

The academic example concerns a two-storey frame system as an academic example modeled by nonlinear elasto-plastic (bilinear) beam elements. The geometrical discretization is shown in Figure 5.10. The frame span is $l = 6$ $[m]$ and the height of it is $h = 4$ $[m]$, consequently the total height is eight meters. The columns as well as the beams of the frame structure are discretized by five elements, which leads, under consideration of the boundary conditions shown in Figure 5.10, to a total number of 86 DOFs. Elasto-pasticity is realized by a bilinear stress-strain curve with kinematic hardening in axial beam direction as shown in Figure 5.11. Fictitious material parameters are assumed in this accademic example to induce large plastic deformations in order to illustrate a clear visualization of the nonlinear behavior and accordingly a good insight into the nonlinear MOR procedure. The paramters of the elasto-plastic (bilinear) material are: Young's modulus $E = 2.1 \times 10^{11}$ $\left[\frac{N}{m^2}\right]$, Poisson's ratio 0.3 $[-]$, elastic yield limit 2.4×10^7 $\left[\frac{N}{m^2}\right]$, with 5% post-yielding stiffness ratio. The cross section of the column is quadratic (0.1×0.1 $[m^2]$) and the cross section of the beam is rectangular (0.1×0.3 $[m^2]$).

In addition to the presented nonlinear system with hysteretic material behavior, the equivalent structure with linear material parameters is presented. The linearized material parameter is equal to the initial stiffness of the elasto-plastic material model presented in Figure 5.11, i.e. Young's modulus: $E = 2.1 \times 10^{11}$ $\left[\frac{N}{m^2}\right]$.

The extended approach of the new MOR strategy is based on the mathematical formulations of the POD in Eqs. (5.47) - (5.51). In structural dynamics, systems are discretized in space and time, therefore, the numerical realization of the proposed strategy is implemented based on the following straightforward algorithm.

Firstly, an a priori response identification, i.e. the realization of a random vector $\mathbf{x}(t)$, is evaluated, where t is in a limited time interval $t_0 \leq t \leq t_1$. Therefore, the response to one excitation in the specific

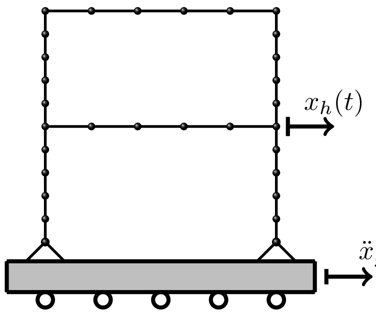

Figure 5.10: Test example: two-story frame structure subjected to ground motion

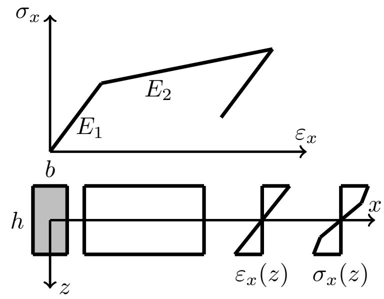

Figure 5.11: Elasto-plastic stress strain relation of the beam in local element coordiates

time period is computed, i.e. Eq. (5.42) is solved numerically in the defined time period. This analysis is performed in the physical coordinate **x**. Consequently this constitutes, dependent on the size of the time period $t_1 - t_0$ (snapshot time period) and the number of DOFs of the system, the most time consuming part of the procedure. According to the actual example, for the linear as well as the nonlinear system, the Bam earthquake in Table 5.4 is chosen as the representative event. The snapshot time period is here limited by $t_1 = 0\ [s]$ and $t_2 = 12\ [s]$. This means that the largest possible time window for the snapshot response identification is chosen, therefore, the maximum possible response information is captured here. Although, in order to increase effectivity of the algorithm a representative deterministic basis can be obtained by concentrating on the strong-motion phase of the earthquake since the relevant nonlinearities will be activated during that phase, but then it is more likely that insufficient POD response bases for MOR transformation matrix for the upcoming analyses are acquired. The time history of the excitation is shown in the left subplot of Figure 5.12.

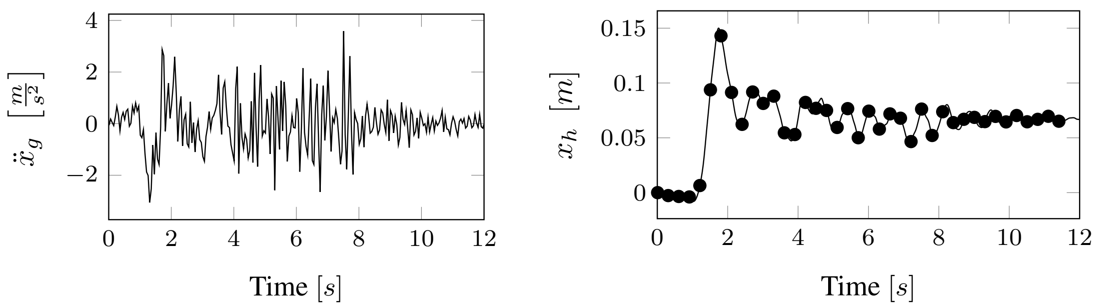

Figure 5.12: left side: Bam earthquake excitation, excitation function in the snapshot time period; right side: Snapshot response function $x_s(t)$ of the nonlinear system (solid line), snapshots (dots)

The snapshot response function $\mathbf{x_s}(t)$, i.e. the random vector, is realized by s observations (snapshots) at different time instances (cf. Han and Feeny *Han and Feeny* (2003)) within the snapshot time period

$$\mathbf{X_s} = [\mathbf{x_{t_1}}, \mathbf{x_{t_2}}, ..., \mathbf{x_{t_s}}] = \begin{pmatrix} x_1(t_1) & \cdots & x_1(t_s) \\ \cdots & \cdots & \cdots \\ x_n(t_1) & \cdots & x_n(t_s) \end{pmatrix} . \tag{5.52}$$

It is of utmost importance to capture nonlinear deformation patterns in order to create the possibility to depict possible nonlinear reactions in forthcoming calculations. In the specific example, 40 observations (snapshots) in equidistant time instances are taken into account from the snapshot response function for the a priori identification of the overall response behavior. Those observations of the nonlinear system are specified by dots in the right subplot of Figure 5.12, to be distinguished from the overall response within the time period of analysis. According to the linear system, the computation of the snapshots is realized by the same procedure. As a result, it is also necessary here to capture the main motion patterns according to possible future response histories. However, it can be observed that for the system identification of the linear response, the required number of snapshots is considerably smaller than for the nonlinear system response.

If $\boldsymbol{\mu}$ is the expectation of all observations, then the sample covariance matrix $\boldsymbol{\Sigma_s}$ of this random vector, which is realized by the observation matrix, is defined by (cf. Kerschen et. al. *Kerschen et al.* (2005))

$$\boldsymbol{\Sigma_s} = E\{(\mathbf{x}-\boldsymbol{\mu})^T(\mathbf{x}-\boldsymbol{\mu})\}\ . \tag{5.53}$$

The POD modes and the POD values are defined by the eigensolution of the sample covariance matrix. If the data have zero mean, the covariance matrix is (cf. Kerschen et al. *Kerschen et al.* (2005))

$$\boldsymbol{\Sigma_s} = \frac{1}{s}\mathbf{X_s}^T\mathbf{X_s} \tag{5.54}$$

and the POD is realized by the singular value decomposition (SVD) of the observation matrix $\mathbf{X_s}$. The POD modes $\varphi_{\mathbf{p,i}}$ are equal to the left singular vectors and the POD values $\lambda_{p,i}$ to the singular values of $\mathbf{X_s}$, which are all real and positive and arranged in a rectangular diagonal matrix in descending order. The energy, which is contained by the snapshot matrix, is defined by the summation of the POD values, i.e. $V = \sum_{i=0}^{s}\lambda_{p,i}$. As a consequence, the energy ratio of the i_{th} POD mode is (cf. Kerschen et al. *Kerschen et al.* (2005))

$$V_i = \frac{\lambda_{p,i}}{\sum_{i=0}^{s}\lambda_{p,i}}\ . \tag{5.55}$$

In structural dynamics applications the sum of only a few POD values often captures the main part of the total energy included in the observation matrix, which reflects the big advantage of the POD, i.e. the property of optimality with respect to energy in a least square sense. In the present demonstration, 99 percent of the total energy is captured by only two deterministic modes. The first two evaluated POD modes of the nonlinear system are depicted in Figure 5.13. In comparison, the natural modes of vibration, which create the basis for the classical modal truncation method are shown in Figure 5.14. They are computed according to the eigenvalue problem $\left(\mathbf{K}-\omega^2\mathbf{M}\right)\Phi = \mathbf{0}$, where $\mathbf{K}$ is the linearized initial stiffness matrix according to the assumption above.

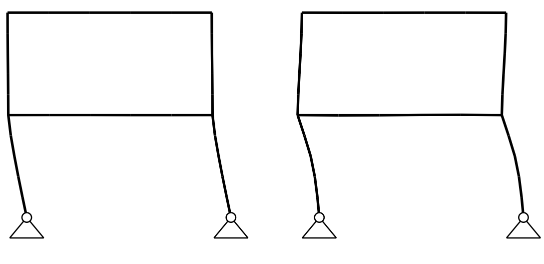

Figure 5.13: First two Pod modes

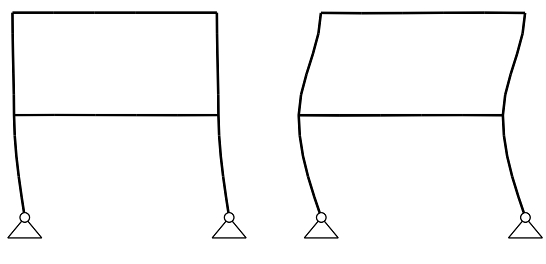

Figure 5.14: First two natural modes

As depicted in Figure 5.13, the POD modes can obviously represent nonlinear displacement patterns, which are expected to occur in this illustrative example, i.e. plastic deformation areas around the joints of the frame system. But rather these deformation patterns are not representable by the first two linear natural modes of vibration depicted in Figure 5.14. Therefore, according to the nonlinear response, an accurate representation of the snapshot response function $x_s(t)$ is expected by the representation of only the two deterministic POD modes, but a significant error by the representation of the first two natural modes of vibration is expected.

Following, the transformation into the reduced subspace is performed in the same manner, as if the classical method of modal truncation would be applied to linear systems. The low-order set of equations of motion is then

$$\widetilde{\mathbf{M}}\ddot{\mathbf{q}}_{\mathbf{P}} + \widetilde{\mathbf{C}}\dot{\mathbf{q}}_{\mathbf{P}} + \widetilde{\mathbf{R}} = \widetilde{\mathbf{F}}\,, \tag{5.56}$$

where $\widetilde{\mathbf{M}} = \mathbf{\Phi}_P^T\mathbf{M}\mathbf{\Phi}_P$ and $\widetilde{\mathbf{C}} = \mathbf{\Phi}_P^T\mathbf{C}\mathbf{\Phi}_P$ are mass- and damping matrices and $\widetilde{\mathbf{F}} = \mathbf{\Phi}_P\mathbf{F}$ is the excitation vector in the POD reduced subspace. The reduced vector of the inner restoring forces $\widetilde{\mathbf{R}}$ is still dependent on the displacement in the physical coordinate $\mathbf{x}$,

$$\widetilde{\mathbf{R}} = \mathbf{\Phi}_P^T\mathbf{R}(\mathbf{\Phi}_P\mathbf{q}_P) = \mathbf{\Phi}_P^T\mathbf{R}(\mathbf{x})\,. \tag{5.57}$$

Therefore, the vector of the inner restoring forces $\mathbf{R}(\mathbf{x})$ has to be evaluated from the physical model in the full-order coordinates in every calculation time step. According to the linear POD reduced system, the vector of the inner restoring forces is described by the relation $\widetilde{\mathbf{R}} = \widetilde{\mathbf{K}}\mathbf{q}_{\mathbf{P}}$, where $\widetilde{\mathbf{K}} = \mathbf{\Phi}_{\mathbf{P}}^T\mathbf{K}\mathbf{\Phi}_p$ is the stiffness matrix in the POD reduced subspace. In this case, no updating in every time step of the inner restoring forces has to be performed. Furthermore, the equations of motion in the reduced-order set are not decoupled and have to be solved numerically. Finally, after the time integration is finished, the solution vector $\mathbf{q}_{\mathbf{P}}$ dependent on time is transformed back into the physical coordinate $\mathbf{x}$. Concerning the representative excitation, a comparison of the full benchmark solution (snapshot response function $x_s(t)$) makes sense in order to verify the quality of the low-dimensional representation of the POD modes. If the approximation of the benchmark solution (in this example: Bam earthquake response) is satisfactory, then the reduced solution to the whole set of the remaining earthquakes is calculated by application of these deterministic modes. If the approximation is not sufficient, one possibility is to increase the number of snapshots within the snapsthot time period, another one is to change the start and end time instances t_0 and t_1 of the snapshot response function in order to improve the response information quality of the snapshot matrix (remark: in this paper t_0 and t_1 are already the beginning and end time step of the Bam excitation record). The visualization of the novel approach is depicted in Figure 5.15.

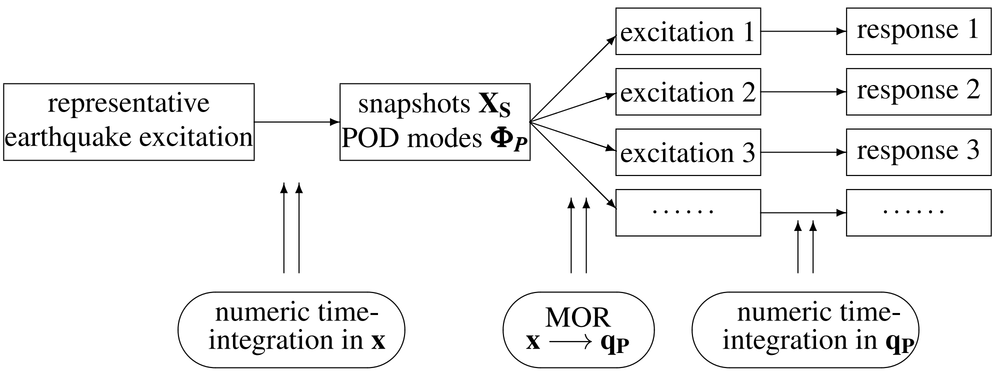

Figure 5.15: Approach of the new strategy

All computational results according to the whole excitation set presented in Table 5.2.2 are depicted in Figures 5.16 - 5.21. Within each of the response computations of the linear, as well as the nonlinear

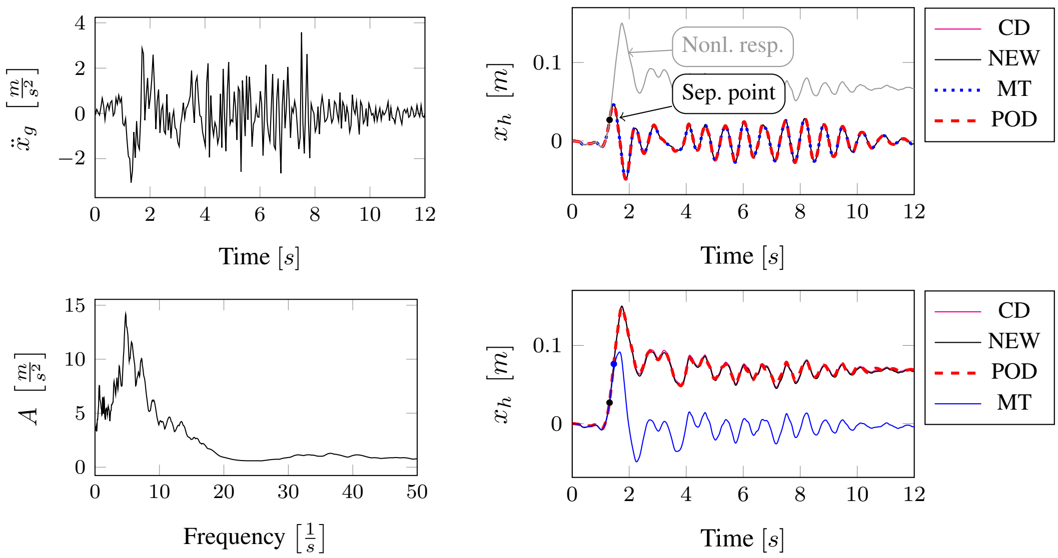

Figure 5.16: Results Bam earthquake. Top left: Bam earthquake time history; bottom left: peak acceleration response spectrum $\zeta = 0.04$; top right: linear response functions; bottom right: nonlinear response functions

system, two different integration algorithms were chosen for the integration procedure in the physical (full) coordinate (86 DOFs), i.e. the implicit Newmark integration (NEW) and the explicit central difference scheme (CD). They serve as reference solutions to the suggested new POD strategy (POD), which is compared to the classical modal truncation method (MT). In each Figure on the top right, the nonlinear response is also for the sake of comparison plotted. All time response functions are compared according to the horizontal displacement in the right corner of the first floor of the frame structure, $x_h(t)$, depicted in Figure 5.10. For the reduced computations, 2 DOFs concerning the new POD strategy (99.9 % of the total energy of the snapshots is captured) and 4 DOFs concerning the classical MT strategy (according to an assumed cut-off frequency of 30 Hz dependent on a qualitative investigation of the fourier transforms of the events (mode 1: 1.46 [Hz], mode 2: 6.45 [Hz], mode 3: 20.38 [Hz], mode 4: 23.65 [Hz], mode 5: 40.15 [Hz]) are considered.

According to the proposed strategy in Figure 5.15, the Bam earthquake serves as the representative event (Figure 5.12). A test run of the reduced order model over the time period of the representative Bam earthquake shows that the deterministic POD modes can represent the nonlinear (elasto-plastic) response time history. This is shown in the top right and the bottom right subplot in Figure 5.16. According to Figure 5.16, both the linear and the nonlinear POD response functions approximate the full reference solutions (NEW and CD) accurately. Therefore, the deterministic set of POD modes is able to represent nonlinear (plastic) deformation patterns. Consequently, the chosen number of 40 snapshots within the chosen snapshot time period (see Figure 5.12) is apparently sufficient for this example. Figures 5.17 - 5.21 present the numerical evaluation of the rest of the earthquake set shown in Table 5.2.2, i.e. the comparison of the reduced order models with the full benchmark solutions. In each of the linear and nonlinear response evaluations it is shown that the POD responses provide reliable approximations of the benchmark solutions (response functions are overlapping with each other). This underlines the robustness of the new strategy according to changes in the excitation if the deterministic POD modes are evaluated based on a different excitation history (see Figure 5.12).

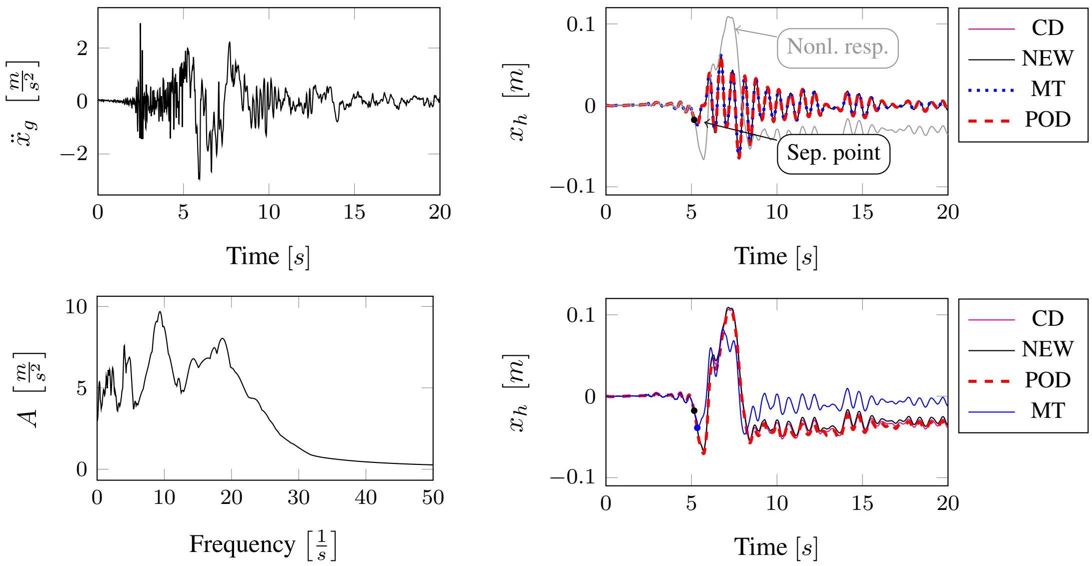

Figure 5.17: Results Imperial Valley earthquake. Top left: Imperial Valley earthquake time history; bottom left: peak acceleration response spectrum $\zeta = 0.04$; top right: linear response functions; bottom right: nonlinear response functions

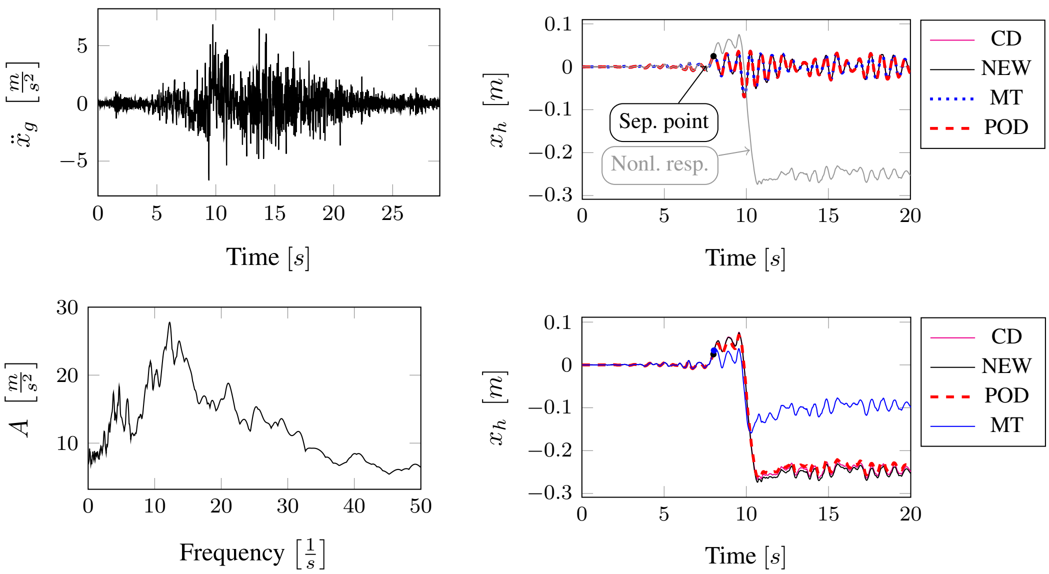

Figure 5.18: Results Landers earthquake. Top left: Landers earthquake time history; bottom left: peak acceleration response spectrum $\zeta = 0.04$; top right: linear response functions; bottom right: nonlinear response functions

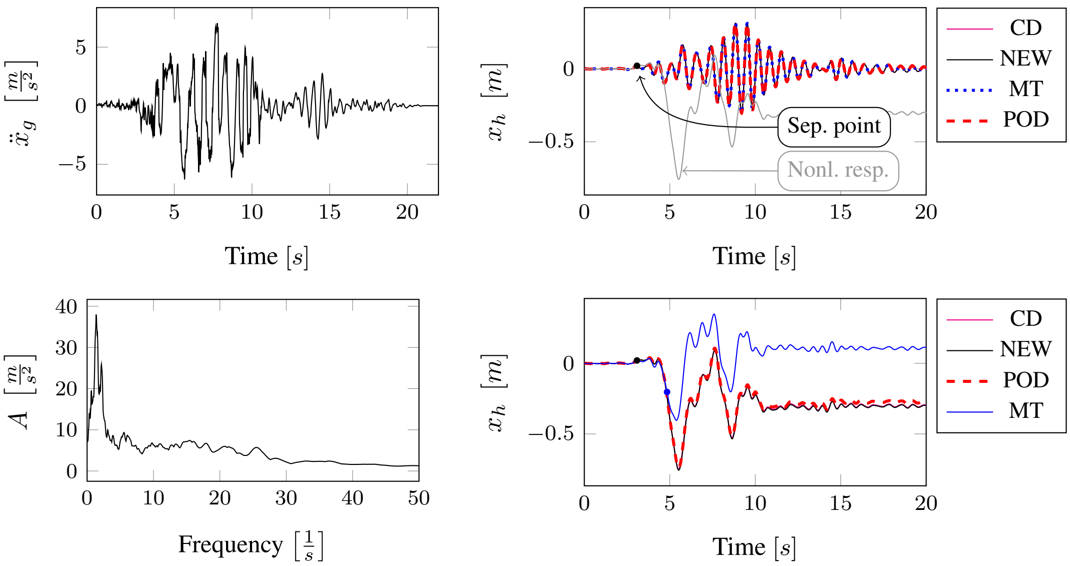

Figure 5.19: Results Loma Prieta earthquake. Top left: Loma Prieta earthquake time history; bottom left:peak accleration response spectrum $\zeta = 0.04$; top right: linear response functions; bottom right: nonlinear response functions

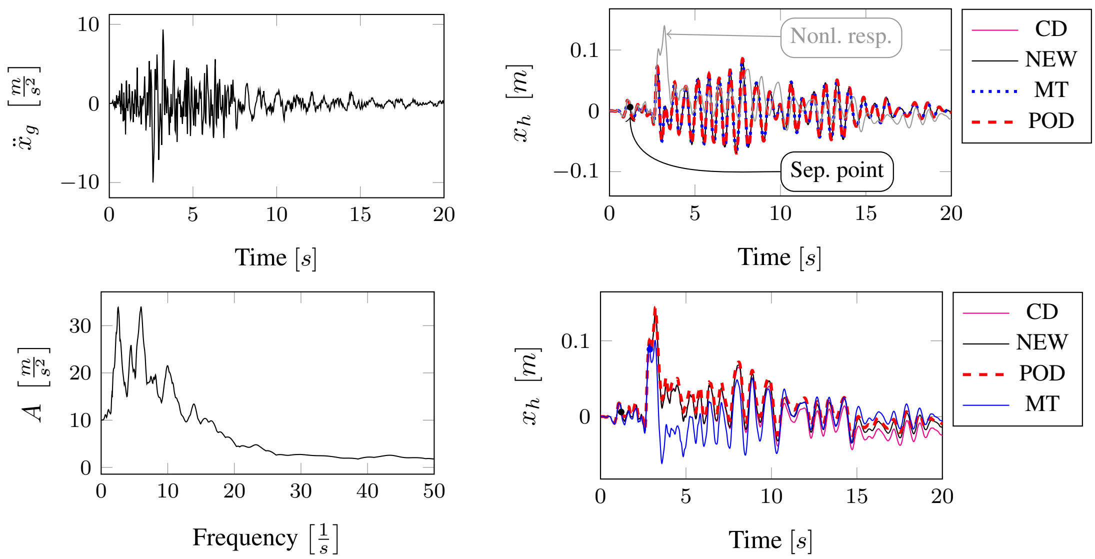

Figure 5.20: Results North Palm Springs earthquake. Top left: North Palm Springs earthquake time history; bottom left: peak acceleration response spectrum $\zeta = 0.04$; top right: linear response functions; bottom right: nonlinear response functions

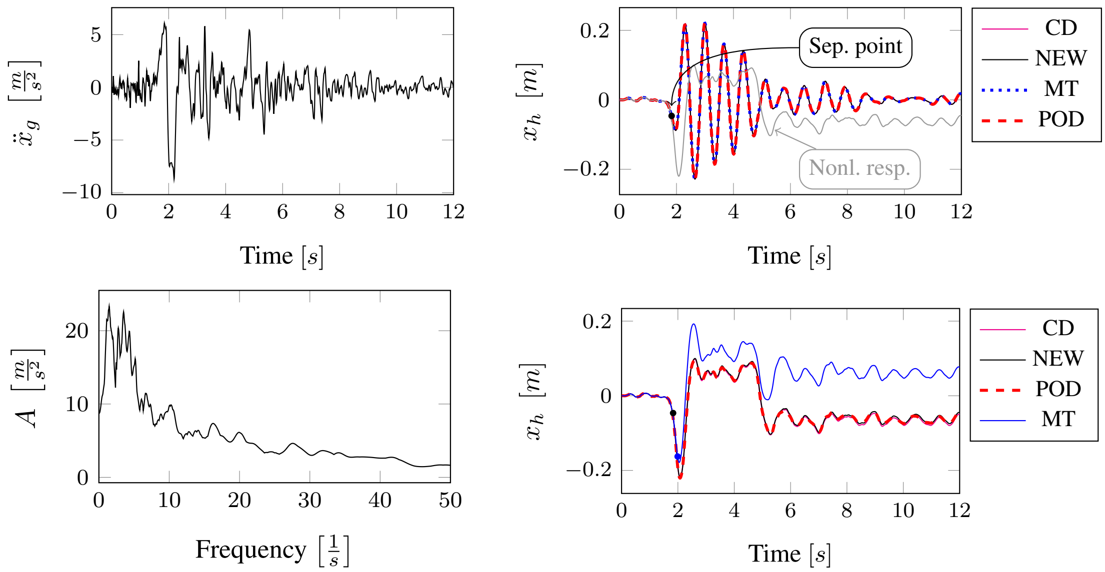

Figure 5.21: Results Northridge earthquake. Top left: Northridge earthquake time history; bottom left: peak acceleration response spectrum $\zeta = 0.04$; top right: linear response functions; bottom right: nonlinear response functions

According to the linear computations, both strategies show accurate results (see the top right subplots of Figures 5.16 - 5.21). In this special linear elastic case, the method of modal truncation shows slight advantages, which is not surprising as no snapshot response function in the physical coordinate must be evaluated. However, a distinct advantage is that the POD strategy does not require an investigation of the Fourier transform of the excitation in order to determine the cut-off frequency for estimating the truncation of the natural basis modes. On the contrary, the POD method fulfills the requirement in Eq. (5.47) and (5.2.3), where an optimally truncated basis is defined. Therefore, dependent on the required level of accuracy, an automatic truncation based on the energy content per mode is performed (see Eq. (5.55)). According to the nonlinear system (see the bottom left subplots of Figures 5.16 - 5.21), the modal truncation responses show a severe deficit with respect to the exact solution, since the natural modes (as earlier presented within the Figures 5.13 and 5.14) cannot detect the nonlinear deformation patterns. On the contrary, the POD strategy, as already discussed above, shows reliable approximations. Therefore, in the presence of strong nonlinearities, the new POD strategy has sizeable advantages over the classical method of modal truncation. However, within a limited range, the modal truncation method is reliable. In the top right subplots of Figures 5.16 - 5.21 the separation point (sep. point, black mark) defines the time instant, when, according to Figure 5.11, the first nonlinear effect occurs (yielding of the material). Before this time instant, each response line (CD, NEW, POD, MT) is the same. This is not surprising, because this is the simple linear-elasic solution. Afterwards, as presented in the top right subplots of Figures 5.16 - 5.21, the nonlinear yielding effect is shown by the drift-off of the light gray nonlinear reference responses in these subplots (nonl. resp.), which is equivalent to the nonlinear Newmark response of the bottom right subplots of these Figures. Here, the black mark also shows the separation point of the linear and the nonlinear response and, additionally, the qualitative separation point of the modal truncation solution (blue mark), i.e. where the modal truncation solution drifts off. Therefore, it is clearly shown that there is a limited range of nonlinearity, where the modal truncation response also presents useful results - after the modal truncation separation point, a severe drift-off of this solution function is observed.

The first substantial numerical benefit of the proposed strategy arises from the combination of the MOR and the application of an explicit time integration method, such as the second order central difference scheme. The time consuming part of the computation is the evaluation of the inner restoring force vector, which has to be evaluated in every time step on Gauss integration point level in the physical (full) coordinate according to Eq. (5.57). This recalculation cannot be avoided. The application of an explicit time integrator to the full system leads inevitably to considerably small integration time steps, which have to be smaller than a certain value (critical time step for the central difference scheme $\Delta t_{cr} = \frac{2\pi}{\omega_n}$, where ω_n is the highest eigenfrequency). Therefore, a huge number of time steps has to be processed within one integration run and, consequently, a high number of the expensive recalculations of the inner restoring force vector $\mathbf{R}(\mathbf{x})$. For the integration in the POD reduced subspace the critical time step is considerably larger (according to this example in the paper even larger than the measurement time step of the earthquake data), which leads to a stabilization of the procedure and, as a consequence, to approximately a 500-fold increase of speed compared to the full central difference integration method (CD). These numerical issues are discussed in a similar manner by Gutierrez and Zaldivar (*Gutierrez and Cela* (1998)) applied to modal truncation. For the numerical benefit of the combination of the basic POD method with explicit numeric time integration, the reader is referred to Bamer and Bucher (*Bamer and Bucher* (2012)). It would also be possible to implement an implicit integration scheme (i.e. the Newmark method with constant acceleration assumption) in the reduced subspace, which is under special circumstances convergent for all possible time steps. However, the application of this integration scheme requires the iterative Newton Raphson procedure, following, in each timestep of the reduced system, the restoring force vector R must be computed several times (modified Newton Raphson method). If the classical (not modified) Newton Raphson method is applied the number of iterations is minimized, but then in every iteration procedure the tangential stiffness matrix in the full space is to be evaluated, which has then again transformed into a tangential stiffness matrix in the reduced supspace. Therefore, the explicit central difference scheme is chosen, which is stabelized by the model order reduction process. Generally, each integration scheme can be applied for the realization of the POD reduced strategy and, of course, the choice of the integration scheme is also dependent on the level of high dimensionality, type of nonlinearity, etc.

The second big numerical advantage of the new strategy is that the actual time consuming process, which is the evaluation of the snapshot matrix, is only executed once at the beginning of the whole calculation procedure. This a priori assumption of nonlinear mode patterns makes sense if the excitations show physical "similarities", which is the case in earthquake analysis, where a considerably small number of low frequency modes is mainly affected.

The practical application of this novel approach in earthquake engineering analyses can be realized in a straightforward manner. Earthquake design codes frequently specify the earthquake loading in terms of response spectra rather than actual acceleration records, but this is directly usable only in the case of linear system behavior. For the analysis of nonlinear systems, several response spectrum compatible artificial earthquake accelerations (as specified e.g. in Eurocode 8) can be generated, see e.g. *Giaralis and Spanos* (2009). Based on these artificial accelerations the proposed model order reduction approach is carried out exactly as described in this section.

5.2.4.1 Error evaluation

For the sake of accuracy evaluation a posteriori error analysis is presented. As reference solution to the reduced response functions, i.e. solutions by POD reduction and modal truncation, the solution of the

Central Difference algorithm in the physical coordinate is chosen. The error indicators are

$$x_{r,POD}(t) = |x_{h,CD}(t) - x_{h,POD}(t)| \tag{5.58a}$$
$$x_{r,M}(t) = |x_{h,CD}(t) - x_{h,M}(t)| \ , \tag{5.58b}$$

where $x_{h,CD}(t)$, $x_{h,POD}(t)$ and $x_{h,M}(t)$ are the response functions of the Central Difference, the POD and the Modal Truncation responses of the node shown in Figure 5.10. Figure 5.22 represents the absolute error of the reduction methods corresponding to analyses provided in Figures 5.16 to 5.21 as defined in Eq. (5.58).

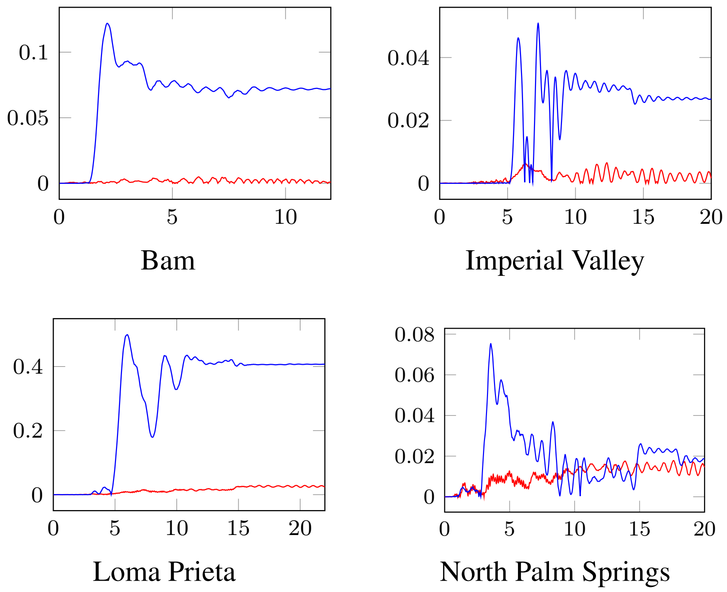

Figure 5.22: Error evaluation; x-axes ... time $[s]$, y-axes ... POD error function $x_{r,POD}(t)$ $[m]$ (red) and modal truncation error function $x_{r,M}(t)$ $[m]$ (blue)

As depicted in Figure 5.22, the error by application of the classical modal truncation method is much more considerable than the error produced by the approximation through the POD strategy. Especially, if the structure responds nonlinearly, that is, plastic deformation patterns occur, a huge difference by application of the modal truncation method is observed. Figure 5.22 provides evidence of the inability of the linear modes to represent elaso-plastic displacement patterns shown in Figure 5.13 and 5.14. Additionally, the applicability and accuracy of the proposed POD strategy seems not to be remarkably sensitive to differences of the peak acceleration response spectra of the excitation time histories in the presented examples. This is seen in the peak acceleration response spectra in the bottom left plot of the Figures 5.16 to 5.21 and the related error functions in Figure 5.22, where a correlation between those parameters cannot be detected directly. One noticeable point is here that the error functions of the Landers and the Northridge response in Figure 5.22 seem to be in similar ranges, but the characteristics of the response spectra show considerable differences. Therefore, the proposed strategy demonstrates a high robustness with regard to time history analysis in earthquake engineering and should be of great value in this field.

However, a more extensive evaluation of direct correlations between changes in the spectra of the excitation histories and the quality of the outcome of the POD response is beyond the scope of this chapter. Additionally, future research should also include a priori error estimations based on wavelet transformations of the excitation functions. The underlying idea is that earthquake records with similar intensities and frequency contents activate the same nonlinearities and consequently lead to the same POD basis. A publication concerning this strategy appeared quite recently (*Podrouzek et al.* (2014)).

5.2.5 Practical application of the new approach

In addition to dealing with the development of the introduced novel POD-based MOR approach, it is within this section to represent the application of the new proposed MOR strategy on a realistic example. For this purpose, a dynamic structural model of a medical complex, according to its constructional plan, was derived. A schematic three-dimensional sketch of the building is depicted in Figure 5.23.

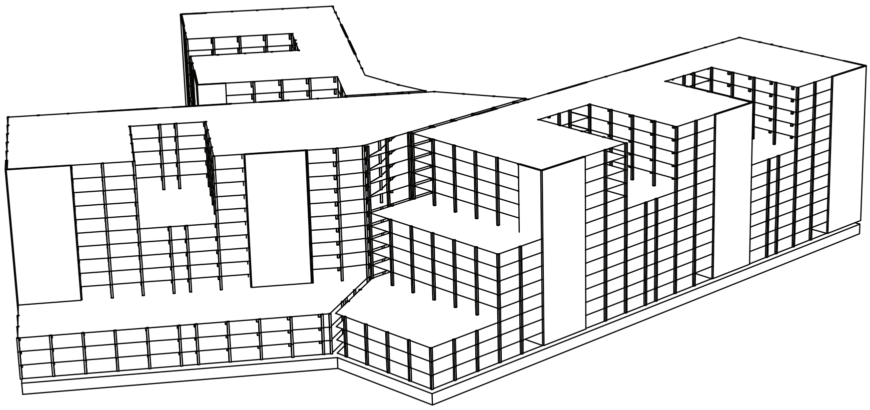

Figure 5.23: Three-dimensional visualization of the building structure

As shown in Figure 5.23, the building structure exhibits complex geometries. As a result, it seems to make sense to discretize the geometry by a finite element model in order to capture the main dynamic specifications.
If such a structure with medical function is located in an earthquake prone region, one way to improve its seismic performance can be realized through base isolation by means of frictional pendulum bearings. Consequently, the analytical simulations demand large computational time and storage due to the presence of nonlinearity imposed by those frictional isolators. In the following, firstly, the structural system specifications and implementation of frictional bearings are presented. Then, the displacement responses to the set of the six earthquake events presented in Table 5.2.2 are evaluated. The numerical evaluations compare the new introduced strategy, as an alternative means, with the iterative Newmark integration scheme, which is known as an efficient and exact method.

5.2.5.1 Structural system and model specifications

The building structure consists of three wings, referred to as wing I, II and III. Figure 5.24 shows a schematic sketch of the ground plan of the building containing the basic dimensions. The floor slabs of each wing are separate from the others except for the basement slab, which is indiscrete over all three wings. This means that all three wings are coupled through this slab and they work all together during the earthquake excitations. However, the distance between the wings, which are connected by the basement slab, is about 1.5 meters, consequently, contact problems induced by ground motion are not considered in the computations.

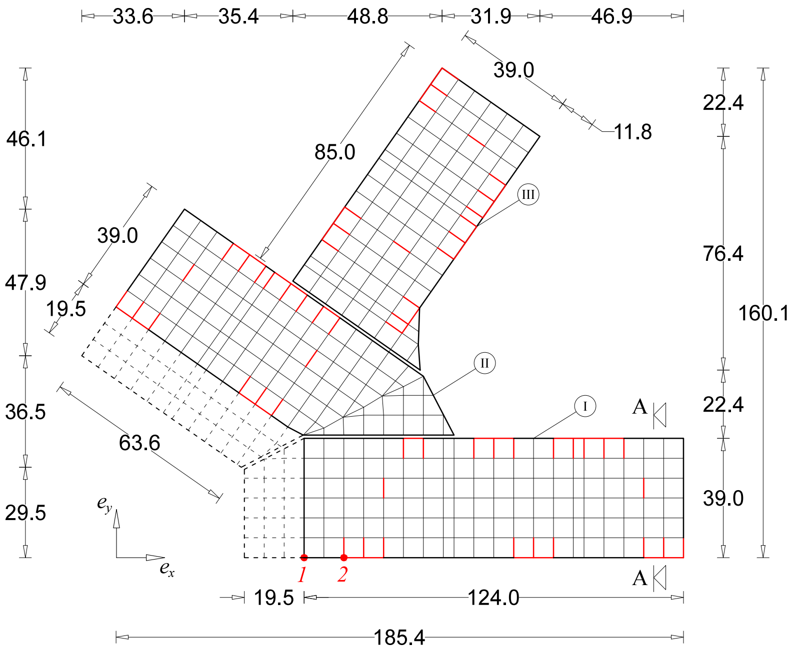

Figure 5.24: Schematic ground plan, building construction (units in meters), output nodes 1 and 2 (red marks)

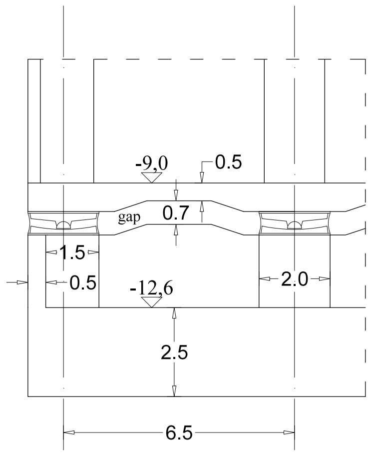

Figure 5.25: A schematic cutout of the vertical section A-A of the basement levels presented in Figure 5.24 (units in meters)

The grid indicates the location of the columns and the binding beams, and the red lines indicate the location of the shear walls, which are responsible for the lateral reinforcement. The regular distance between the columns is 6.5 $[m]$. The building structure has three stories below the ground level, while the highest parts of the building above ground level have 13 stories and the remaining parts have eight stories including the basement levels. Therefore, the plan of the structure is irregular along its height along with the irregularities in the horizontal area. The dashed lines define the area, where the building is only located below the ground. The height of one story is three meters; this leads to a total construction height of 42 meters.

Below the three stories at the basement level, there is the indiscrete slab on the top of the isolators at level of -9.00 $[m]$. Below this slab, along each of the columns, a single friction pendulum (FP) bearing system is attached. Figure 5.25 depicts a part of the cross section A-A of the basement level shown in Figure 5.24. The horizontal diameter of the FP system is 2.00 meter. Thus, the dimension of the quadratic cross section of the columns in the basement and FP story is 2.00×2.00 $[m^2]$, while in the remaining stories the columns are modeled as quadratic cross sections with the dimensions 0.40×0.40 $[m^2]$. All FP bearings have the same radius of the concave surface, which is equal to 3.00 meters.

A representative full-scale finite element model of the building structure was created in the software package slangTNG (*Bucher and Wolff* (2013)). The shear walls and slabs were modeled by shell/plate elements and the columns and beams by beam elements. A linear elastic material was considered for the modeling of the superstructure (Young's modulus $E = 3.5 \cdot 10^{10}$ $[\frac{N}{m^2}]$, Poisson's ratio $\nu = 0.3$ $[-]$, density $\rho = 2500$ $[\frac{kg}{m^3}]$). Nonlinear FP elements, whose implementation in slangTNG is presented in section 5.2.5.2, are assigned below the lowest basement plate of the structure. The total number of DOFs is 33000.

As a result, the superstructure behaves linearly, which is the major reason for implementing base isolator systems for earthquake vibration protection.

5.2.5.2 Dynamic model of the frictional pendulum element

This is to present how the frictional pendulum (FP) element in the finite element model of the structure behaves. The geometrical diagram of the FP element, which is realized as a spherical shell, is defined in Figure 5.26. As depicted, R denotes the radius of the concave spherical surface and the origin of the local coordinate system is chosen to be in the center of the sphere. The position vector of the slider is described by $\mathbf{U} = [u, v, w]^T$. Since the desired behavior of the FP element is an in-plane elasto-plastic bidirectional action, the change of the vertical position w can be neglected. Accordingly, the displacement of the FP element is reduced to an in-plane motion defined only by the components u and v, i.e. $\mathbf{U} = [u, v]^T$. This simplification makes sense as the radius R is much larger relative to the horizontal displacement $|\mathbf{U}| \approx \sqrt{u^2 + v^2}$. The equivalent representation of such an element together with the acting forces on it is represented in Figure 5.27.
The horizontal force equilibrium of the dynamical system is

$$\mathbf{F_{Fr}} + \mathbf{F_k} = \mathbf{F_{ex}} \,, \tag{5.59}$$

where $\mathbf{F_{Fr}}$ and $\mathbf{F_k}$ are the elasto-plastic frictional- and centring force and $\mathbf{F_{ex}} = [F_x, F_y]^T$ accounts for the interacting horizontal force, which couples the FP element to the super structure.
Following, the force equilibrium is split into two parts as two dynamic situations can occur: situation stick and situation slide. The force equilibrium during the situation stick yields to

$$\mathbf{F_{ex}} = \underbrace{k_1 \left\{ \begin{array}{c} u \\ v \end{array} \right\}}_{\mathbf{F_k}} + \underbrace{k_2 \left\{ \begin{array}{c} \Delta u \\ \Delta v \end{array} \right\}}_{\mathbf{F_{Int}}} \quad \text{if} \quad |\mathbf{F_{ex}} - \mathbf{F_k}| < \mu N \,. \tag{5.60}$$

This relation renders a linearly-elastic system, where the friction coefficient μ must be a value between 0 and 1. For the computations, this value was taken to be once 4 % and for the second demonstration run of the method it was set equal to 8 %. The normal contact force N acts orthogonal to the contact area of the slider and the concave surface. The vector $\boldsymbol{\Delta U} = [\Delta u, \Delta v]^T$ defines the radial distance with respect to the current sticking point of the slider if the sticking condition is true. During the situation slide the FP element is described by the following horizontal force equilibrium

$$\mathbf{F_{ex}} = \underbrace{k_1 \left\{ \begin{array}{c} u \\ v \end{array} \right\}}_{\mathbf{F_k}} + \underbrace{\frac{\mu N}{|\dot{\mathbf{U}}|} \left\{ \begin{array}{c} \dot{u} \\ \dot{v} \end{array} \right\}}_{\mathbf{F_{Fr}}} \quad \text{if} \quad |\mathbf{F_{ex}} - \mathbf{F_k}| \geq \mu N \,, \tag{5.61}$$

where $\dot{\mathbf{U}} = [\dot{u}, \dot{v}]^T$ is the velocity vector.
In both relations, i.e. Eq. (5.60) and Eq. (5.61), the centring force $|\mathbf{F_k}| = k_1 r = k_1 \sqrt{u^2 + v^2}$ acts linearly orthogonal to the vertical axis through the deepest point of the surface and the center of the sphere. The fact that the centring force is linear indicates that the spherical shell of the real system is approximated by the paraboloid, whose potential energy increases with $\frac{W}{R} r$ in radial distance from the deepest point, i.e. the stiffness is inversely proportional to the radius of the sphere $k_1 = \frac{W}{R}$.

The frictional force $\mathbf{F_{Fr}}$ is modeled either linearly elastic or elastic-perfectly plastic as presented in Eqs. (5.60) and (5.61), respectively. Note that, $\mathbf{F_{Int}}$ the force corresponding to $\boldsymbol{\Delta U}$ accounts for the internal elastic behavior of the bearing coating material, in a small elastic range (situation stick, Eq. (5.60)) and acts towards the current location of the slider (not the center of the concave sphere). Generally, the implementation of a realistic model requires k_2 to be much larger than k_1, i.e. $k_2 \gg k_1$. During the

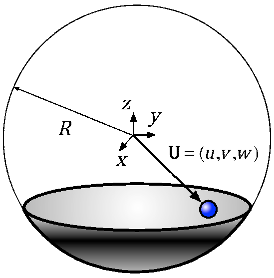

Figure 5.26: Geometric definition of the FP element

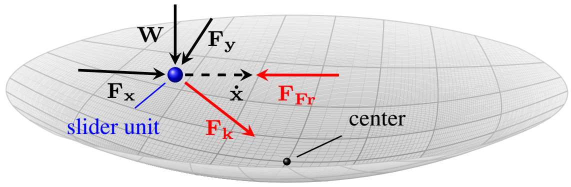

Figure 5.27: Internal specifications of the FP element; F_x, F_y, N, recentering force $\mathbf{F_k}$, frictional force $\mathbf{F_{Fr}}$

situation slide, the frictional force acts in opposite direction to the velocity with the magnitude (perfectly plastic) μN. This is discussed in Eq. (5.61). Another point regarding Eq. (5.60) is that the reacting force N is assumed to be constant throughout the calculation procedure. This is justified by the following reasons: Firstly, just x and y components of the exciting ground motion are taken into account for the computations. Secondly, the motion has already been simplified to be planar and therefore no additional force component due to vertical motion is generated. Finally, in our preliminary analysis, the uplift force on the isolator slap was observed to be extremely small in comparison with the downward force due to the weight of the structure. Considering the above-mentioned fact together with the force diagram given in in Figure 5.27, follows that the normal contact force N is approximately constant and equal to the weight induced force of the super structure, W, i.e, $N = W$ in Eq. (5.61).

The FP bearing element governed by Eqs. (5.59) to (5.61) has been implemented in the software package slangTNG (*Bucher and Wolff* (2013)). For a comparable study on this implemented friction pendulum system, the experimental work of Mosqueda et al. (*Mosqueda et al.* (2004)) is suggested. Concerning the computations in this paper, the friction coefficient μ of the FP slider is assumed to be a constant value, as discussed above. However, μ is indeed a value dependent on velocity, pressure and temperature. Recent publications dealing with this issue are authored by Castaldo and Tubaldi (*Tubaldi* (2015)), as well as Kumar et. al. (*Kumar et al.* (2015)). Regarding the proposed new strategy, it is expected that the implementation of a friction coefficient, which depends on velocity, pressure and temperature, would lead to comparable results concerning accuracy and speed of the reduced order model. In other words, it is envisaged that a specific nonlinear model of the FP bearing element with variable friction coefficient does not influence the overall behavior of the reduced order model in comparison to the full model, i.e. the effectiveness of the model order reduction procedure. In every time step the vector of the inner restoring forces in Eq. (5.57) has to be evaluated in the full (physical) coordinate anyway.

For additional information about friction pendulum systems the reader is referred to the literature (e.g. *Almazan et al.* (1998), *Llera and Almazan* (2003), *Ordonez et al.* (2003), *Ryan and Chopra* (2004), *Ray et al.* (2013) and *Bucher* (2009b)). More detailed examination of this topic would lead beyond the scope of this paper, which should focus more on the methodical extension of the new MOR strategy as well as the application on a complex realistic system.

5.2.5.3 Numerical evaluation

The evaluation of the MOR strategy applied to the realistic building structure is dealt with displacement response calculations to the six different earthquake excitations presented in Table 5.4. The Calculation

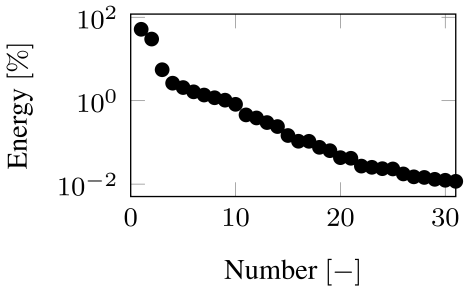

Figure 5.28: POD values; friction coefficient $\mu = 0.04$ $[-]$ (logarithmic scale)

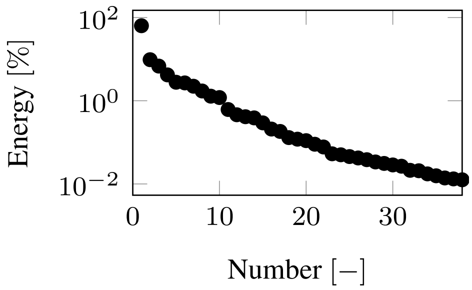

Figure 5.29: POD values; friction coefficient $\mu = 0.08$ $[-]$ (logarithmic scale)

outputs are presented by the in-plane motion response of the slider at the red marked node (node 1: coordinates $[19.5, 0.0, -9.5]^T$ $[m]$) in Figure 5.24 in x- and y-direction. As this node defines the location of a moving friction pendulum, it shows directly the nonlinear response behavior of the system. Additionally, a second output node (node 2: coordinates $[32.5, 0.0, h]^T$ $[m]$) is chosen. Here, the coordinate h stands for every possible storey of the building structure. According to $h = 32.5$ $[m]$ the maximum acceleration of the roof is presented and according to each storey ($h = -9.5, -6.5, -3.5, \ldots, 32.5$ $[m]$), the maximum drift responses are shown.

The numerical demonstrations are performed by assuming two different friction coefficients for the FP-isolators, namely 4% and 8%. The methodology applied to the realistic example is equivalent to the academic example, which is presented in section 5.2.4. Therefore, the main focus below is on the presentation of the numerical results.

Integration over the whole Bam earthquake by the Newmark method in the physical coordinate leads to the snapshot response function $\mathbf{x_S}(t)$ and consequently to the snapshot matrix $\mathbf{X_S}$, which contains 400 snapshots in equidistant time intervals. Following, the evaluation of the left singular vectors of the snapshot matrix leads to the POD modes and its singular values to the POD values in descending order. The number of POD modes that have to be taken into account in order to capture 99,99 percent of the total energy was evaluated to be 31 for the calculations concerning the friction coefficient of 4 % and 38 concerning the friction coefficient of 8 %. The logarithmic plots of the singular values (POD values) for both friction coefficients dependent on the corresponding energy are shown in the Figures 5.28 and 5.29.

Time integration in the 31- and 38-dimensional PODs, which contain 99% of the total energy, reduced subspace over the whole Bam earthquake produces the POD reduced response. After back transformation into the physical coordinate, the reduced response must be compared with the benchmark solution (full Newmark response). The response motion of the slider (output node 1) of the full and the POD-reduced calculation is depicted in Figures 5.30(a) (friction coefficient of 4%) and 5.31(a) (friction coefficient of 8%). As clearly shown, a reliable approximation of the benchmark solution is achieved, therefore, nonlinear effects can be represented. In the next step, the responses to the remaining earthquakes are evaluated in the reduced subspaces, as well as the full reference solutions by application of the standard Newmark algorithm.

The first 30 modes are computed according to a linearization of the slider element. The boundary conditions below each slider element are fixed. The required linearization of the slider element is realized by taking the initial stiffness matrix of the system into account, similarly to the linearization assumption of the academic example. This inevitably leads to an over-estimation of the slider stiffness, although the vector of the inner restoring forces is calculated.

The red lines in the Figures 5.30 and 5.31 show the POD reduced responses and the blue lines the full reference solutions. As depicted in these Figures, accurate approximations are achieved for both assumptions of the friction coefficients (note: the lines cover each other). Additionally, it is clearly shown in these Figures that the modal truncation method fails to approximate the full solution.

The maximum accelerations at the roof in output node 1 are presented in the left and right subplot of Figure 5.32. Additionally, the maximum drifts between all floors above output node 2 are presented in Figures 5.33 and 5.35. As for both friction coefficients, the slider drift itself (drift in the floor 0) is generally much larger (which is actually the purpose of base isolation). Therefore, for each of the friction coefficients a second figure is presented in order to create the possibility to visualize the results, not only in the slider, but also in the hospital building itself. This is realized in Figures 5.34 and 5.36. The numerical values of the drifts of the stories 0 (slider drift), 1, 5, 10 and 14 are presented in Tables 5.5 (for friction coefficient of 0.04) and 5.6 (for friction coefficient of 0.08).

It is expected that the proposed new strategy is also applicable to different types of nonlinearities, e.g. large deformations, viscoelasticity, viscoplasticity, hyperelasticity etc. In addition, concerning seismic protection, it is expected that the proposed new strategy is also applicable to smart structures with shape memory alloy-based seismic damping and isolation tools. The new strategy should produce response approximations with comparable accuracy to the nonlinearites already presented in this paper. However, it is also of utmost importance here to emphasize the fact that the nonlinear deformation patterns, namely the special hysteretic behavior dependent on superelasticity, temperature and memory effect, must be captured in the snapshot matrix.

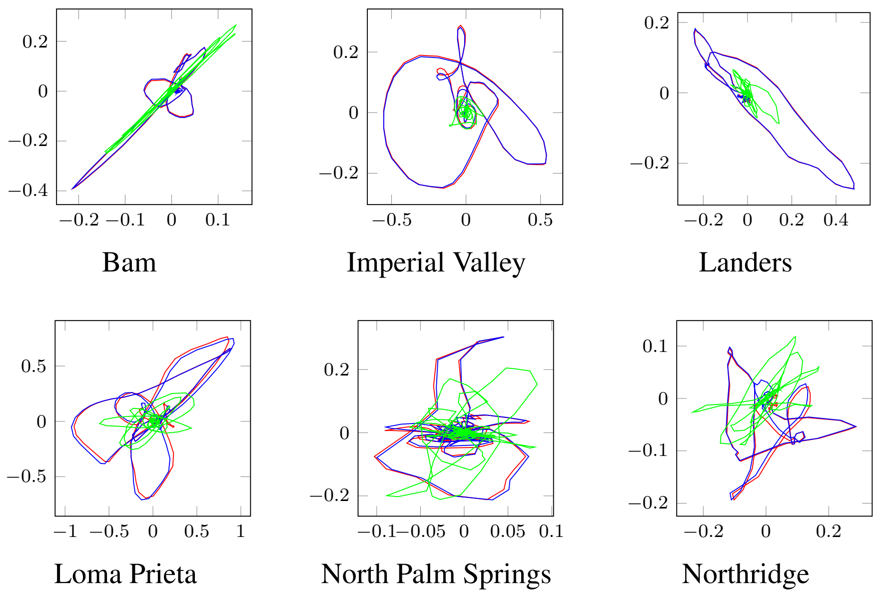

Figure 5.30: Planar position of the FP-element (output node) over the time period of excitation; friction coeficent $\mu = 0.04$; x-axes ... slider displacement in x-direction $[m]$, y-axes ... slider displacement y-direction $[m]$; blue line ... full response; red line ... POD response; green line ... mode superposition response

5.2.6 Conclusion

In this chapter, a model order reduction (MOR) strategy, which is applicable to the dynamic response analysis of linear and nonlinear structural systems is presented. Usually, the analysis of building structures

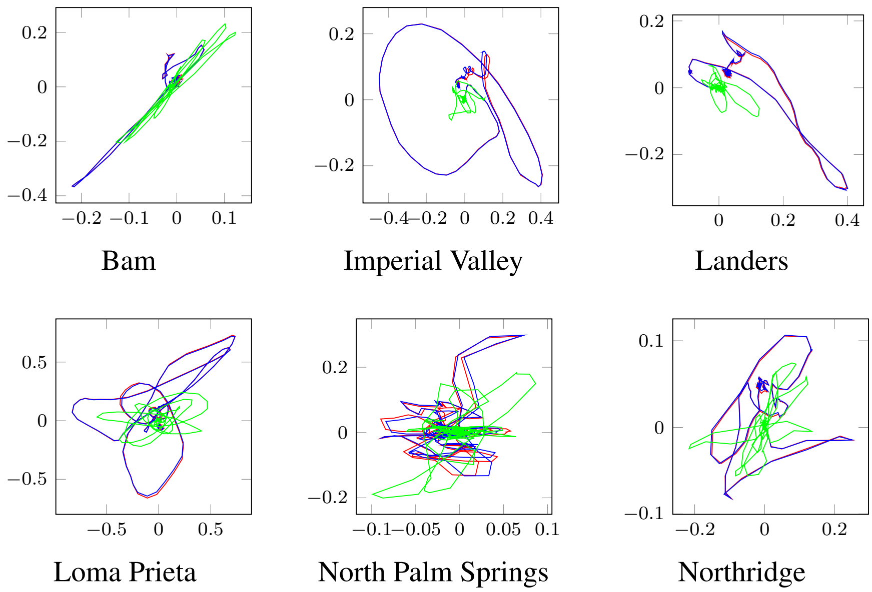

Figure 5.31: Planar position of the FP-element (output node) over the time period of excitation; friction coeficent $\mu = 0.08$; x-axes ... slider displacement in x-direction $[m]$, y-axes ... slider displacement y-direction $[m]$; blue line ... full response; red line ... POD response; green line ... modal superposition response

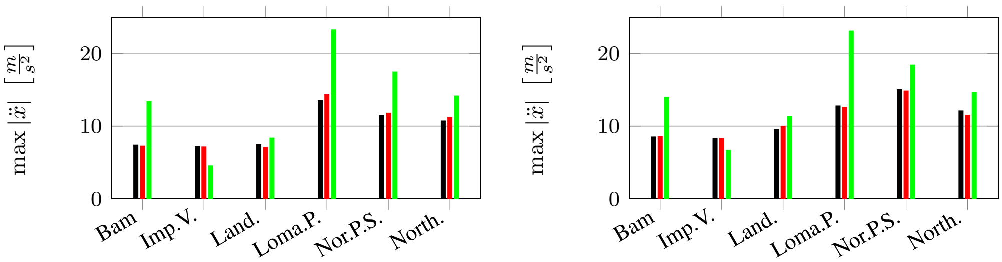

Figure 5.32: Maximum acceleration at the roof; left subplot: $\mu = 0.04$; right subplot: $\mu = 0.08$; full newmark (black), POD response (red), modal truncation (green)

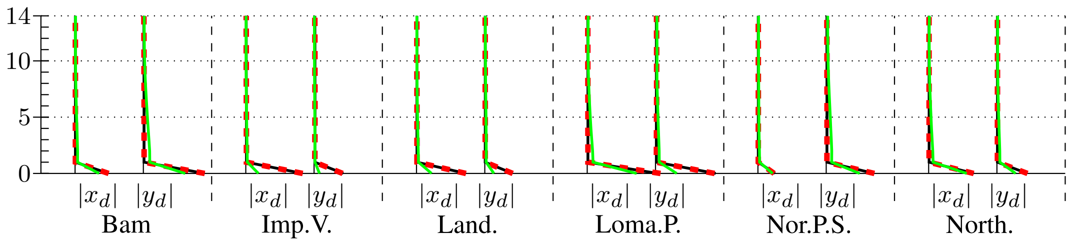

Figure 5.33: Maximum drift of the stories above the output node 2 in x and y direction; friction coefficient: $\mu = 0.04$, including the slider drift in the ground floor 0

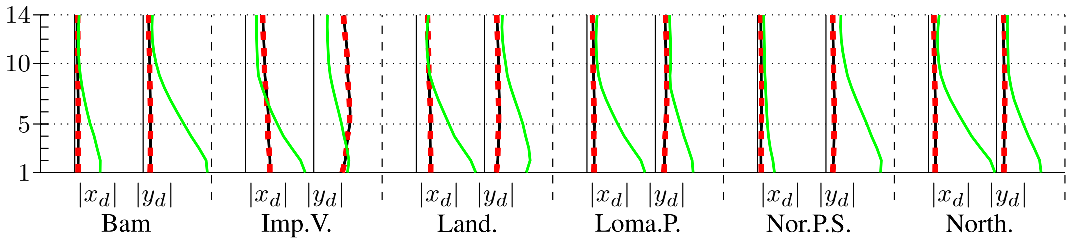

Figure 5.34: Maximum drift of the stories above the output node 2 in *x* and *y* direction; friction coefficient: $\mu = 0.04$, excluding the slider drift in the ground floor 0

Storey	Bam x_d	Imp.V x_d	Land. x_d	Lom.P. x_d	Nor.P.S x_d	North. x_d
0	0.212	0.556	0.482	0.899	0.107	0.287
1	0.00201	0.00618	0.00449	0.00874	0.00215	0.00293
5	0.00223	0.00587	0.00452	0.00947	0.00239	0.00304
10	0.00182	0.00488	0.00385	0.00836	0.00225	0.00259
14	0.00167	0.00439	0.00346	0.00745	0.00190	0.00234

Table 5.5: *x*-component of the maximum drift of node 2 in meter; full system; $\mu = 0.04$ corresponding to the Newmark response function

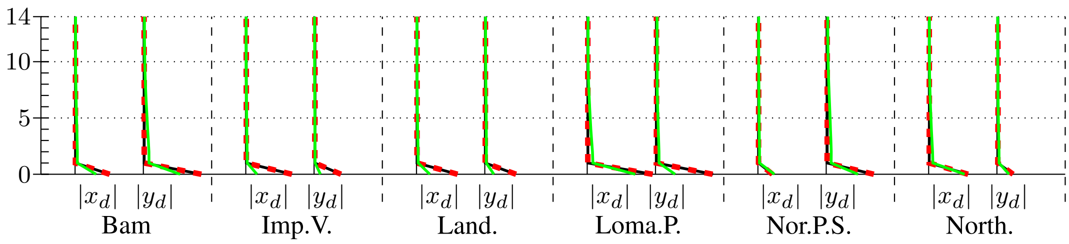

Figure 5.35: Maximum drift of the stories above the output node 2 in *x* and *y* direction; friction coefficient: $\mu = 0.08$, including the slider drift in the ground floor 0

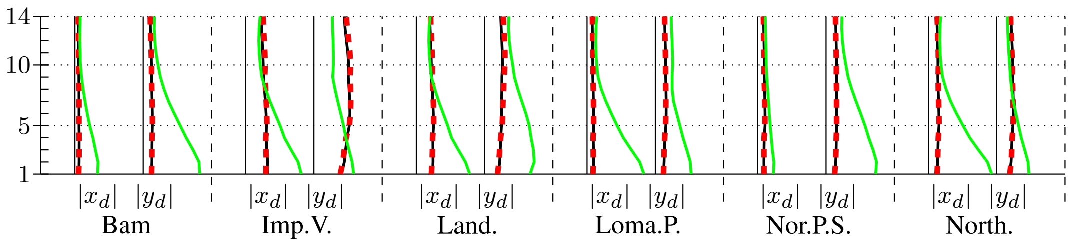

Figure 5.36: Maximum drift of the stories above the output node 2 in *x* and *y* direction; friction coefficient: $\mu = 0.04$, excluding the slider drift in the ground floor 0

Storey	Bam x_d	Imp.V x_d	Land. x_d	Lom.P. x_d	Nor.P.S x_d	North. x_d
0	0.219	0.451	0.399	0.832	0.0933	0.250
1	0.00247	0.00562	0.00514	0.00810	0.00398	0.00370
5	0.00256	0.00529	0.00546	0.00836	0.00463	0.00444
10	0.00243	0.00448	0.00477	0.00732	0.00418	0.00400
14	0.00209	0.00391	0.00426	0.00656	0.00368	0.00352

Table 5.6: x-component of the maximum drift of node 2 in meters; $\mu = 0.08$ corresponding to the Newmark response function

with complex geometries makes the engineer to create a finite element model with a large number of DOFs, which is associated with computational effort in the response analysis. Therefore, the goal of this paper is to provide a new model order reduction strategy that is simple in application, but also very effective even in the presence of nonlinearities for problems in the field of earthquake engineering and structural dynamics. This strategy is extended based on the proper orthogonal decomposition (POD) method to derive a proper transformation matrix in order to transform the nonlinear systems into another low-dimensional subspace, which demands considerably less computational effort for the response calculation. Once the transformation matrix is derived, the approach of the strategy is similar to the method of modal truncation for linear systems. The presentation of the novel approach comes along with a simple and illustrative example that points out the benefit compared to standard methods as modal truncation.

In addition to the development of the MOR strategy, its application for the response calculation of a realistic numerical nonlinear example is demonstrated. The example is the displacement response calculation of a building structure serving as a medical complex, which is base-isolated by friction pendulum bearing systems excited by six earthquake excitations. In order to evaluate the accuracy of the introduced approach, the exact structural responses are also calculated. Numerical evaluations show that reliable approximations can be achieved if nonlinear response patterns of the structure are already captured in the POD snapshots to extract the transformation matrix. The advantage of this strategy is obviously that the transformation matrix is derived just once and it can be used for response calculation of the structure under different earthquake excitations.

Another substantial advantage of the introduced MOR concerns the speed of the response calculations. Firstly, compared to the basic central difference algorithm, the new introduced strategy has a much larger critical time step. Secondly, compared to the Newmark method, which allows usually larger time steps, no iteration procedure is required.

Chapter 6

Conclusions

The primary goal of the dissertation is development of a procedure for inverse identification of the wind load from the measured structural response. This procedure was expanded step-wise from establishing an optimal input-output relation for a structure, adopting proper methods for inverse ill-posed problem, selection of measurement sensors and so on. At each step the validity of the results was verified by means of problem simulations, followed by laboratory tests and afterwards the procedure was implemented in a field application.

In Chapter 2 new formulations to derive the impulse response matrix, which is then used in the problem of load identification with application to wind induced vibration. The applied loads are inversely identified based on the measured structural responses by solving the associated discrete ill-posed problem. To this end — either based on the parametric structural model or modal characteristics — the impulse response functions of acceleration, velocity and displacement have been computed. Time discretization of convolution integral has been implemented according to an existing and a newly proposed procedure, which differ in the numerical integration methods. The former was evaluated based on a constant rectangular approximation of the sampled data and impulse response function in a number of steps corresponding to the sampling rate, while the latter interpolates the sampled data in an arbitrary number of sub-steps and then integrates over the sub-steps and steps respectively. The identification procedure was implemented for a simulation example as well as an experimental laboratory case. The ill-conditioning of the impulse response matrix made it necessary to use Tikhonov regularization to recover the applied force from noise polluted measured response. The optimal regularization parameter has been obtained by Lcurve and GCV method. The results of simulation represent good agreement between identified and measured force. In the experiments the identification results based on the measured displacement as well as acceleration are provided. Further it is shown that the accuracy of experimentally identified load depends on the sensitivity of measurement instruments over the different frequency range.

Chapter 3 develops the procedure of inverse wind load reconstruction, given in Chapter 2, for the large degrees of freedom structures. It was tried to keep the procedure practically applicable and merely based on the data that can be obtained via vibration response measurements, so that extra assumptions for unmeasured degrees of freedom responses or mass and stiffness matrix setup are not required. But instead, just the modal properties of the structural system, which can be obtained directly from the vibration measurements are demanded, in order to generate the augmented impulse response matrix of the system and decompose the measured responses into the modal responses. The presented step-by-step procedure with a fairly comprehensive discussion explains different aspects of the provided wind load identification method for the real applications. An important goal of in this chapter concerned revealing the more consistent response type, i.e. displacement or acceleration, for the wind load recovery. It was found that the measured displacement response is more appropriate for this purpose, due to the higher power of displacement signal in lower frequencies and the smaller condition numbers of the modal displacement impulse response matrix compared to those of the modal acceleration, which consequently makes the inverse problem less sensitive to the contained noise in the displacement data acquired from measurement setup. The quality of the reconstructed modal wind loads based on both response types reduces as the noise level increases. But rather the modal wind load identification from the displacement response, especially by means of the L-curve method, remains sufficiently accurate even at 15% noise level. The background signal of wind load is correctly reconstructed from displacement response whereas the noise-related discrepancy emerges in the high frequency components of the identified load signal above the natural frequency of the corresponding mode.

Chapter 4 presents the field application of the introduced inverse modal wind load identification procedure by full-scale field measurement. The major focus was drawn to the technical aspects of the practical application, including the case study, measurement setup, data processing and the utilized methods within the load identification procedure. It is important to note that all information needed for wind load identification was acquired solely based on the measurement data. In this regard, no additional assumptions were required to be made either on the structural properties e.g. assumptions on system mass or stiffness matrices or on the wind characteristics of the structure's site. It was discussed profoundly, what are the advantages of wind load reconstruction in the modal subspace, use of displacement responses and utilizing the augmented modal impulse response matrices. The structural modal properties were obtained by means of operational modal analysis from the same ambient vibration testing data, which is used for inverse load identification. It is not generally feasible in practice to measure the actual wind loads acting on the structural element, in order to verify the load identification results. It was described that there might not exist another solution for this purpose better than simulation of the problem and observation of the existing analogies. The numerical simulation of the same problem can demonstrate the strength or weakness of the introduced procedure for practical wind load identification. Consequently the validity or failure in the real application of the introduced procedure was verified by means of the analogy between the field and numerical simulation results. It was obviously observed that for a number of first vibration modes the experimental results are reliable.

The dissertation pursued a secondary goal too, which was studied within Chapter 5, section 5.1. This study was a collaborative research work in order to fulfill the requirements of the doctoral program. This work develops methods for stochastic response analysis of structures under wind excitation at least over one year, when the gappy measured response data is available. This work should make it possible to be able to extract response statistics as a function of mean wind speed from the mathematical expressions. The mathematical expressions are derived from the available response data, measured discontinuously at random mean wind speeds in one year. To this end the wind speed data corresponding to each set of response data should be known, moreover the probability distribution of mean wind speeds are required too. For this purpose the wind speed was measured continuously over one year and predominant wind directions as well as mean wind probability density functions based on ten-minute averaging were obtained. The ten-minute structural responses were recorded according to an 18-hour automatic triggering within one year. Then every ten-minute data was tagged by its corresponding mean wind speed. It was comprehensively discussed how to recover the structural response indicators associated with those unmeasured ten-minute time intervals between two consecutive triggering. In this section two response indicators, i.e. displacement response standard deviation and threshold passage counts, were targeted. Those indicators are important for the sake of structural vibration control under long-term random excitations like wind. It was shown that from the sparse response data, the mathematical relationships between response indicator and mean wind speed data can be achieved. In this section an efficient procedure for frequency domain wind fatigue estimation was also introduced. To this end solely the moments of stress PSD is required, in order to calculate the density function of stress amplitude cycle counts. It was represented that the values of the moments of stress PSD at different mean wind speeds corresponding to unmeasured ten-minute time intervals can be retrieved from the existing sparse measurement data. Once the moments of stress PSD are known, the expected one year damage due to wind vibration can readily be calculated. The mathematical relationships between mean wind speed and displacement response standard deviation as well as mean wind speed and moments of stress (displacement) PSD were selected according to the presented theoretical background.

The second collaborative work was described in Chapter 5, section 5.2. This section presents a model order reduction (MOR) strategy, which is applicable to linear and nonlinear structural systems. Usually, the analysis of building structures with complex geometries makes the engineer to create a finite element model with a large number of DOFs, which is associated with computational effort in the response analysis. Therefore a new model order reduction strategy was sought, not only simple in application, but also very effective for problems in the field of earthquake engineering. This strategy is extended based on the proper orthogonal decomposition (POD) method to derive a proper transformation matrix in order to transform the nonlinear systems into another low-dimensional subspace. Once the transformation matrix is derived, the approach of the strategy is similar to the method of modal truncation for linear systems. The application of the method for the response calculation of a realistic numerical nonlinear example is demonstrated. In order to evaluate the accuracy of the introduced approach, the exact structural responses are also calculated. Numerical evaluations show that reliable approximations can be achieved if nonlinear response patterns of the structure are already captured in the POD snapshots to extract the transformation matrix. The advantage of this strategy is obviously that the transformation matrix is derived just once and it can be used for response calculation of the structure under different earthquake excitations. Another substantial advantage of the introduced MOR concerns the speed of the response calculations. Firstly, compared to the basic central difference algorithm, the new introduced strategy has a much larger critical time step. Secondly, compared to the Newmark method, which allows usually larger time steps, no iteration procedure is required.

Chapter 7

Future works and outlooks

Since the introduced procedures and accordingly the results presented in this research appeared to be quite promising and in compliance with the objectives of the research, they imply the possibility to deploy this dissertation's achievements, to be combined with other methods for further researches. I would like to generally address the following outlooks based on the methodological developments, presented in his dissertation:

- As a future work, the online wind load reconstruction (vs. offline method applied in this dissertation) could be mentioned, which essentially leads to application of the state-space observer models of the structural system (*Juang* (1994)) through the structural monitoring. Currently in the existing online load identification methods (see references in sections 3.1 and 4.1), firstly the system matrices (mass, stiffness, damping) in the numerical model of structure — e.g. derived from finite element model of system — must be known. Secondly either the input signal is low-pass filtered or the natural regularization due to the observer behavior (e.g. Kalman filter) is used, in order to cope with noise magnification in identified load. Contrarily, in my opinion and as implemented in this dissertation, firstly the wind load reconstruction procedure should be working based on system modal parameters (natural frequencies, damping ratios and mode shapes) instead of the system matrices. Furthermore the proper regularization scheme, in which the optimal extent of regularization is applicable, should be separately integrated in the procedure (i.e. neither by high-pass filtering nor regularization effect of the observer). Importance is attached to the point that obtaining the modal parameters of complicated structures is more realistic than creating a numerical model of the structure, which can accurately reflect the in-situ structural behavior.

- The verification of the introduced method for wind fatigue analysis based on sparse stress response data (see Chapter 5, section 5.1) can also be explored further. For this purpose, first of all the real stress data is needed. In the presence of measured stress data and in light of the proposed method in section 5.1.6, the expected value of different cycle counts can be compared with those achieved from conventional time domain cycle counting methods. This provides the possibility of cross-check and method verification. Note that, This works demands at least one year collection of stress data and wind speed measurement. However the outcome of this research, once its validity is proven, can be quite attractive, due to its significant practical advantages and computational efficiency.

- Further research work might be the behavior improvement of vibration prone structures by means of in-situ identified wind load. Assume that an actual structure undergoes measurement for the purpose of fatigue analysis and the results show that it does not fulfill the design target lifetime. Consequently the idea of combining the two above mentioned research works could be further explored. In this way, the identified wind load can be deployed for re-analysis of fatigue life of the modified version of the structure, which is going to have the desired fatigue lifetime, as expected in the design. In essence the modified version of the structure has the same geometric shape, but either its mass/stiffness properties will be changed or vibration damper units like TMD or TLCGD will be attached to the structure.

References

Almazan, J., J. Llera, and J. Inaudi (1998), Modelling aspects of structures isolated with the frictional pendulum system, *Earthquake Engineering and Structural Dynamics*, *27*, 845–867.

Anes, V., L. Reis, B. Li, and M. D. Freitas (2014), New cycle counting method for multiaxial fatigue, *International journal of fatigue*, *67*, 78–94.

Arens, E. A., and P. B. Williams (1977), The effect of wind on energy consumption of buildings, *Energy and Bildings*, *1*(77-84).

ASCE (2012), *Wind Tunnel Testing for Buildings and Other Structures*, American Society of Civil Engineers.

Augusti, G., A. Baratta, and F. Casciati (1984), *Probabilistic methods in structural engineering*, Chapman and Hall.

Azam, S. E., E. Chatzi, and C. Papadimitriou (2015a), Experimental validation of the Kalman-type filters for online and real-time state and input estimation, *Journal of Vibration and Control*.

Azam, S. E., E. Chatzi, and C. Papadimitriou (2015b), A dual Kalman filter approach for state estimation via output-only measurements, *Mechanical Systems and Signal Processing*, (60-61), 866–886.

Bamer, F., and C. Bucher (2012), Application of the proper orthogonal decomposition for linear and nonlinear structures under transient excitation, *Acta Mechanica*, *223*, 2549–2563.

Bamer, F., A. Kazemi-Amiri, and C. Bucher (2016), A new model order reduction strategy adapted to nonlinear problems in earthquake engineering, *Earthquake Engineering & Structural Dynamics*, *DOI: 10.1002 \eqe.2802*.

Bannantine, J. A., and D. F. Socie (1991), A variable amplitude multiaxial fatigue life prediction method, in *Fatigue Under Biaxial and Multiaxial Loading*, Mechanical Engineerng Publications.

Belge, M., M. E. Kilmer, and E. L. Miller (2002), Efficient determination of multiple regularization parameters in a generalized l-curve framework, *Inverse Problems*, *18*(1161–1183).

Benasciutti, D., and R. Tovo (2005), Spectral methods for lifetime predition under wide-band stationary random processes, *International Journal of Fatigue*, *27*(867-877).

Blöschl, G., A. P. Blaschke, M. Broer, C. Bucher, G. Carr, X. Chen, A. Eder, M. Exner-Kittridge, A. Farnleitner, A. Flores-Orozco, P. Haas, P. Hogan, A. Kazemi-Amiri, M. Oismüller, J. P. R. Silasari, P. Stadler, P. Strauss, M. Vreugdenhil, W. Wagner, and M. Zessner (2016), The hydrological open air laboratory (HOAL) in Petzenkirchen: a hypothesis-driven observatory, *Hydrology and Earth System Sciences*, *20*, 227–255.

Brandt, A., and R. Brincker (2014), Integrating time signals in frequency domain – comparison with time domain integration, *Measurement*, *58*, 511–519.

Brown, J. C., and I. J. D. Craig (1986), *Inverse Problems in Astronomy, A guide to inversion strategies for remotely sensed data*, CRC Press.

Bucher, C. (2001), Stabilization of explicit time integration by modal reduction, in *Trends in computational structural mechanics*, CIMNE, pp. 429–437.

Bucher, C. (2009a), *Computational analysis of randomness in structural mechanics*, Structures and Infrastructures (Book 3), CRC Press.

Bucher, C. (2009b), Probability-based optimal design of friction-based seismic isolation devices, *Structural Safety*, *31*, 500–507.

Bucher, C., and S. Wolff (2013), slangTNG - scriptable software for stochastic structural analysis, *Reliability and Optimization of Structural Systems, American University of Armenia Press*, pp. 49–56.

Caughey, T. K., and M. M. J. O'Klley (1965), Classical normal modes in damped linear dynamic systems, *Transaction ASME, Journal of Applied Mechanics*, *32*, 583–588.

Chatterjee, A. (2000), An introduction to the proper orthogonal decomposition, *Current Science*, *78*, 808–817.

Chen, T., and M. Lee (2008), Inverse active wind load inputs estimation of the multilayer shearing stress structure, *Wind and Structures*, *11*(1), 19–33.

Cheney, W., and D. Kincaid (2008), *Numerical mathematics and computing*, Thomson learning.

Chopra, A. K. (1995), *Dynamics of Structures, Theory and Applications to Earthquake Engineering*, Prentice-Hall.

Clough, R., and J. Penzien (1995), *Dynamics of structures*, Third ed., Computers & Structures, Inc.

Cusumano, J. P., and M. T. S. B. W. Kimble (1993), Spatial coherence measurements of a chaotic flexible-beam impact oscillator, *American Society of Mechanical Engineers, Aerospace Division*, *33*, 13–22.

Davenport, A. G. (1961a), The spectrum of horizontal gustiness near the ground in high wind, *Quarterly Journal of the Royal Meteorological Society*, *87*, 194–211.

Davenport, A. G. (1961b), The application of statistical concepts to the wind loading of structures, in *Proceedings of the Institution of Civil Engineers*, vol. 19-4, pp. 449–472.

Davenport, A. G. (1963), The buffeting of structures by gusts, in *Proceedings, International Conference on Wind Effects on Building and Structures*, pp. 358–391.

Davenport, A. G. (1967), The dependence of wind loads on meteorological parameters., in *Proceedings International Research Seminar"*, vol. 1, pp. 19–82, University of Toronto Press, Ottawa, Canada.

Deodatis, G. (1996), Simulation of ergodic multivariate stochastic processes, *Journal of Engineering Mechanics*, *122*, 778–787.

Di Paola, M. (1998), Digital simulation of wind field velocity, *Journal of Wind Engineering and Industrial Aerodynamics*, *71-76*, 91–109.

Di Paola, M., and I. Gullo (2001), Digital generation of multivariate wind field processes, *Probabilistic Engineering Mechanics*, *16*(1), 1–10.

Dirlik, T. (1985), Application of computers in fatigue analysis, Ph.D. thesis, University of Wawrick.

Dorvlo, A. S. (2002), Estimating wind speed distribution, *Energy Conversion and Management*, *43*, 2311–2318.

Dowling, N. E. (2013), *Mechanical behavior of materials*, fourth ed., Pearson Education Limited.

Dowling, S. D., and D. F. Socie (1982), Simple rainflow counting algorithm, *International Journal of Fatigue*, (31-40).

Feeny, B. F., and R. Kappagantu (1998), On the physical interpretation of proper orthogonal modes in vibrations, *Journal of Sound and Vibration*, *211*, 601–616.

Friswell, M. I., and J. E. Mottershead (1995), *Finite Element Model Updating in Structural Dynamics*, Kluwer Academic Publishers.

Garcia, A., J. L. Torres, E. Prieto, and A. D. Francisco (1998), Fitting wind speed distributions: A case study, *Solar Energy*, *62*(2), 139–144.

Giaralis, A., and P. D. Spanos (2009), Wavelet-based response spectrum compatible synthesis of accelerograms - eurocode application (ec8), *Soil Dynamics and Earthquake Engineering*, *29*, 219–235.

Gladwell, G. (2005), *Inverse Problems in Vibration*, 2 ed., Springer.

Golivani, G. K. J. C. (2003), A model updating strategy of non-linear vibrating structures, *International Journal of Numerical Methods in Engineering*, *60*, 2147–2164.

Groetsch, C. W. (1984), *The Theory of Tikhonov Regularization for Fredholm Equations of the First Kind*, Pitman.

Gunturk, B. K., and X. Li (2013), *Image Restoration: Fundamentals and Advances*, CRC Press.

Gutierrez, E., and J. J. L. Cela (1998), Improving explicit time integration by modal truncation techniques, *Earthquake Engineering and Structural Dynamics*, *27*, 1541–1557.

Gutierrez, E., and J. M. Zaldivar (2000), The application of karhunen-loeve, or principal component analysis method, to study the non-linear seismic response of structures, *Earthquake Engineering and Structural Dynamics*, *29*, 1261–1268.

Halfpenny, A. (1999), A frequency domain approach for fatigue estimation from finite element analysis, in *Proceedings, International conference on damage assessment of structures*, Dublin, Ireland.

Han, S., and B. Feeny (2003), Application of proper orthogonal decomposition to structural vibration analysis, *Mechanical Systems and Signal Processing*, *17*(989-1001).

Hansen, P. C. (1987), Regularization, gsvd and truncated gsvd, *BIT Numerical Mathematics*, *27*, 543–553.

Hansen, P. C. (2007), A matlab package for analysis of discrete ill-posed problems, *Numerical Algorithms*, *46*, 189–194.

Hansen, P. C., and D. P. O'Lary (1993), The use of L-curve in the regularization of discrete ill-posed problems, *SIAM J. Sci. Comput.*, *14-16*, 1487–1503.

Hartog, J. P. D. (1956), *Mechanical Vibrations*, reprint of 4th ed., McGraw-Hill.

Hebruggen, J. V., P. J. G. V. D. Linden, H. J. Knittel, and S. J (2002), Engine internal dynamic force identification and combination with engine structural and vibro acoustic transfer function, in *Vehicle noise and vibration 2002*, no. 2002-3 in IMechE conference transactions, Professional engineering publishing.

Hillary, B., and D. J. Ewins (1984), The use of strain guages in force determination and frequency response function measurements, in *Proceeding*, pp. 627–634, Proceedings of the 2nd Int. Modal Analysis Conference IMAC, Florida U.S.A.

Holmes, J. D. (2007), *Wind Loading of Structures*, 2 ed., CRC Press.

Holmes, P., J. L. Lumely, and G. Berkooz (1996), *Turbulence, Coherent Structures, Dynamical Systems and Symmetry*, Cambridge University Press.

Huang, M. (2016), *High-Rise Buildings under Multi-Hazard Environment*, Springer.

Hwang, J.-S., A. Kareem, and W.-J. Kim (2009), Estimation of modal loads using structural response, *Journal of Sound and Vibration*, *326*, 522–539.

Hwang, L., A. Kareem, and H. Kim (2011), Wind load identification using wind tunnel test data by inverse analysis, *Journal of Wind Engineering and Industrial Aerodynamics*, *99*, 18–26.

Ibrahimbegovic, A., and E. L. Wilson (1992), Efficient computational procedures for systems with local nonlinearities, *Engineering Computations*, *9*, 385–398.

Irvine, T. (2016), Multiaxial rainflow fatigue methods for nonstationary vibrations, in *Proceedings, Movics and Rasd*, Sothampton, UK.

Jacquelin, E., A. Bennani, and P. Hamelin (2003), Force reconstruction: analysis and regularization of a deconvolution problem, *Journal of Sound and Vibration*, *265*(1).

Jankowski, Ł. (2013), Dynamic load identification for structural health monitoring, *IPPT Report on Fundamental Technological Research 2/2013*, Institute of Fundamental Technological Research, Polish Academy of Sciences, Warsaw.

Jia, J. (2011), Wind and structure modelling for an accurate fatugue life assessment of tubular structures, *Engineering Structures*, *33*, 477–491.

Juang, J. (1994), *Applied System Identification*, Prentice Hal, New Jersy.

Kaimal, J. C., J. C. Wyngaard, Y. Izumi, and O. R. Coté (1998), Spectral characteristics of surface-layer turbulence, *Quart. J. Royal Meteorology Soc.*, pp. 563 – 589.

Kappagantu, R., and B. F. Feeny (1999), An "optimal" modal reduction of a system with frictional excitation, *Journal of Sound and Vibration*, *224*, 863–877.

Kappagantu, R., and B. F. Feeny (2000a), Part 1: Dynamical characterization of a frictionally excited beam, *Nonlinear Dynamics*, *22*, 317–333.

Kappagantu, R., and B. F. Feeny (2000b), Part 2: Proper orthogonal modal modeling of a frictionally excited beam, *Nonlinear Dynamics*, *23*, 1–11.

Kareem, A. (1983), Mitigation of wind induced motion of tall buildingss, *Wind Engineeing and Industrial Aerodynamics*, *11*(273-284).

Karhunen, K. (1947), über lineare methoden in der wahrscheinlichkeitsrechnung, Ph.D. thesis, University of Helsinki.

Kazemi-Amiri, A., and C. Bucher (2014), Identification of fluctuating wind load distribution along the structure's height inversely by means of structural response, in *Advances in civil, environmental and material researches (ACEM 14)*.

Kazemi-Amiri, A., and C. Bucher (2015), Derivation of a new parametric impulse response matrix utilized for nodal wind load identification by response measuremen, *Journal of Sound and Vibration*, (344), 101–113.

Kemper, F. H., and M. Feldmann (2011), Fatigue life prognosis for structural elements under stochastic wind loading based on spectral methods, part i: Linear structures, in *Proceedings of the 18th international conference on structural dynamics, EURODYN*, Leuven, Belgium.

Kerschen, G., and J. C. Golivani (2002), Physical interpretation of the proper orthogonal modes using the singular value decomposition, *Journal of Sound and Vibration*, *249*, 849–865.

Kerschen, G., C. Golinval, F. Vakakis, and Bergman. (2005), The method of proper orthogonal decomposition for dynamical characterization and order reduction of mechanical systems: An overview, *Nonlinear Dynamics*, *41*, 147–169.

Khatibi, M., M. Ashory, A. Malekjafarian, and R. Brincker (2012), Mass–stiffness change method for scaling of operational mode shapes, *Mechanical Systems and Signal Processing*, *26*, 34–59.

Klimer, M., and D. P. O'Lary (2001), Choosing regularization parameter in iterative methods for ill-posed problems, *SIAM J. Matrix Anal. Appl.*, *22*, 1204–1221.

Kosambi, D. (1943), Statistics in function space, *Journal of the Indian Mathematical Society*.

Koutsovasilis, P., and M. Beitelschmidt (2008a), Comparison of model reduction techniques for large mechanical sytems, *Multibody System Dynamics*, *20*, 111–128.

Koutsovasilis, P., and M. Beitelschmidt (2008b), Comparison of model reduction techniques for large mechanical sytems, *Multibody System Dynamics*, *20*, 111–128.

Kristensen, L., and N. O. Jansen (1979), Lateral coherence in isotropic turbulence and in the natural wind, *Boundary-Layer Meteorology*, *17*(3), 353–373.

Krysl, P., S. Lall, and J. E. Marsden (2001), Dimensional model reduction in non-linear finite element dynamics of solids and structures, *International Journal for Numerical Methods in Engineering IJNME*, *51*, 479–504.

Kumar, M., A. S. Whittaker, and C. Constantinou (2015), Characterizing friction in sliding isolation bearings, *Earthquake Engineering And Structural Dynamics*, *44*, 1409–1425.

Law, S., and X. Zhu (2011), *Moving Loads Dynamic Analysis and Identification Techniques*, Structures and Infrastructures, CRC Press.

Law, S. S., J. Q. Bu, and X. Q. Zhu (2005), Time-varying wind load identification from structural responses, *Engineering structures*, *27*(1586-1598).

Lawson, C. L., and R. J. Hanson (1974), *Solving Least Squares Problems*, Prentice-Hall, Englewoods Clifs, NJ.

Leclèrea, Q., C. Pezerata, B. Laulagneta, and L. Polacb (2005), Indirect measurement of main bearing loads in an operating diesel engine, *Journal of Sound and Vibration*, *286*(1-2), 341–361.

Lee, S. (2014), An advanced coupled genetic algorithm for identifying unknown moving loads on bridge decks, *Mathematical Problems in Engineering*.

Lee, Y.-L., J. Pan, R. Hathaway, and M. Barkey (2005), *Fatigue testing and analysis*, Elsevier Inc.

Liang, Y. C., H. Lee, S. P. Lim, W. Z. L. WZ, K. H. Lee, and C. G. Wu (2002), Proper orthogonal decomposition and its applications - part 1: Theory, *Journal of Sound and Vibration*, *525*, 527–544.

Llera, J., and J. Almazan (2003), An experimental study of nominally symmetric and asymmetric structures isolated with the fps, *Earthquake Engineering and Structural Dynamics*, *32*, 891–918.

Loeve, M. (1946), Fonctions al eatoire de second ordre, *Revue Scientifique*, *48*, 195–206.

Lopez-Aenlle, M., P. Fernandez, R. Brincker, and A. Fernandez-Canteli (2010), Scaling-factor estimation using an optimized mass-change strategy, *Mechanical Systems and Signal Processing*, *24*, 1260–1273.

Lourens, E., E. Reynders, G. D. Roeck, D. Degrande, and G. Lombaert (2012), An augmented Kalman filter for force identification in structural dynamics, *Mechanical System and Signal Processing*, *27*, 446–460.

Maia, N. M. M., J. M. M. Silva, J. He, N. A. J. Lieven, R. M. Lin, G. W. Skingle, W. To, and A. P. V. Urgueira (1998), *Theoretical and experimental modal analysis*, Research Studies Press Ltd.

Matsushi, M., and T. Endo (1968), Fatigue of metals subjected to varying stress, in *Japan Society of Mechanical Engineers*.

Meirovitch, L. (1980), *Computational methods in structural dynamics*, Stijhof and Noordhof international publishers, Alphen aan den Rijn.

Melbourne, W. H., and T. R. Palmer (1992), Accelerations and comfor criteria for building undergoing complex motions, *Wind Engineeing and Industrial Aerodynamics*, (105-116).

Mitchell, L. D. (1990), Complex modes: a review, in *8th International Modal Analysis Conference*, pp. 891–899.

Modarresi, K. (2007), A local regularization method using multiple regularization levels, Ph.D. thesis, Stanford university.

Mosqueda, G., A. Whittaker, and G. Fenves (2004), Characterization and modeling of friction pendulum bearings subjected to multiple components of excitation, *Journal of Structural Engineering ASCE*, *130*, 433–442.

Mršnik, M., J. Slavič, and M. Boltežar (2013), Frequency-domain methods for a vibration-fatigue-life estimation- application to real data, *International Journal of Fatigue*, *47*, 8–17.

Nashed, M. Z., and O. Scherzer (2001), *Inverse Problems, Image Analysis, and Medical Imaging*, American Mathematical Society.

Nateghi-A, F. (1996), Assessment of wind speeds that damage buildings, *Journal of the International Society for the Prevention and Mitigation of Natural Hazards*, *14*, 73–84.

Neto, M., F. Duarte, da S. Neto, and A. José (2013), *An Introduction to Inverse Problems with Applications*, Springer.

Niedbal, N. (1984), Analytical determination of real normal modes from measured complex responses, in *25th structures, structural dynamics and materials conference*, pp. 292–295.

Ordonez, D., D. Foti, and L. Bozzo (2003), Comparative study of the inelastic response of base isolated buildings, *Earthquake Engineering and Structural Dynamics*, *32*, 151–164.

Pacific Earthquake Engineering Research Center, P. (2016), http://nisee.berkeley.edu.

Papoulis, A. (1984), *Signal Analysis*, McGraw-Hill, International Student Edition, Polytechnique Institute of New York.

Parloo, E., P. Verboven, P. Guilaume, and M. V. Overmeire (2002), Sensitivity-based operational mode shape normalisation, *Mechanical Systems and Signal Processing*, *16*(5), 757–767.

Peter, B., and G. D. Roeck (1999), Reference-based stochastic subspace identification for output-only modal analysis, *Mechanical System and Signal Processing*, *13*(6), 855–878.

Podrouzek, J., C. Bucher, and G. Deodatis (2014), Identification of critical samples of stochastic processes towards feasible structural reliability applications, *Structural Safety*, *47*, 39–47.

Qu, Z., Y. Shi, and H. Hua (2001), A reduced-order modeling technique for tall buildings with active tuned mass damper, *Earthquake Engineering and Structural Dynamics*, *30*, 349–362.

Qu, Z. Q. (2004), *Model order reduction techniques with application in finite element analysis*, Springer London Limited.

Ray, T., A. Sarlis, A. Reinhorn, and M. Constantinou (2013), Hysteretic models for sliding bearings with varying frictional force, *Earthquake Engineering and Structural Dynamics*, *42*, 2341–2360.

Rega, G., and H. Troger (2005), Dimension reduction of dynamical systems: Methods, models, applications, *Nonlinear Dynamics*, *41*, 1–15.

Reynders, E., and G. D. Roeck (2008), Reference-based combined deterministic-stochastic subspace identification for experimental and operational modal analysis, *Mechanical Systems and Signal Processing*, *22*(3), 617–637.

Reynders, E., R. Pintelon, and G. D. Roeck (2008), Uncertainty bounds on modal parameters obtained from stochastic subspace identification., *Mechanical Systems and Signal Processing*, *22*(4), 948–969.

Reynders, E., M. Schevenels, and G. D. Roeck. (2014), *A MATLAB Toolbox for Experimental and Operational Modal Analysis, MACEC 3.3*, Structural Mechanics division, KU Leuven.

Ryan, K., and A. K. Chopra (2004), Estimating the seismic displacement of friction pendulum isolators based on non-linear response history analysis, *Earthquake Engineering and Structural Dynamics*, *33*, 359–373.

Salcher, P., H. Pradlwarter, and C. Adam (2016), Reliability assessment of railway bridges subjected to high-speed trains considering the effects of seasonal temperature changes, *Engineering Structures*, *126*, 712–724.

Sanchez, J., and H. Benaroya (2014), Review of force reconstruction techniques, *Journal of Sound and Vibration*, *333*(14), 2999–3018.

Schemann, A. G., and H. A. Smith (1998), Vibration control of cable-stayed bridges - part 1: modelling issues, *Earthquake Engineering and Structural Dynamics*, *27*, 811–824.

Seguro, J., and T. W. Lambert (2000), Modern estimation of the parameters of Weibull wind speed distribution for wind energy analysis, *Wind Engineeing and Industrial Aerodynamics*, *85*, 75–84.

Simiu, E., and R. H. Scanlan (1978), *Wind Effcts on Structures*, Wiley.

Sines, G. (1955), Fatigue of materials under combined repeated stress superimposed with static stresses, *Tech. rep.*, National advisory council for aeronautics, Washington D. C.

Solari, G. (1993), Gust buffeting. I: Peak wind velocity and equivalent pressure, *Journal of Structural Engineering*, *119*(2).

Tikhonov, A. N., and V. Y. Arsenin (1997), *Solution of ill-posed problems*, Wiley, New York.

Trefethen, L. N., and D. Bau III (1997), *Numerical linear algebra*, Society for industrial and applied mathematics, SIAM.

Tubaldi, P. C. E. (2015), Influence of fps bearing properties on the seismic performance of base-isolated structures, *Earthquake Engineering And Structural Dynamics*, *44*, 2817–2836.

Tubino, F., L. Carassale, and G. Solari (2003), Seismic response of multi-supported structures by proper orthogonal decomposition, *Earthquake Engineering and Structural Dynamics*, *32*, 1639–1654.

Varah, J. M. (1973), On the numerical solutin of ill-conditioned linear systems with application to ill-posed problems, *SIAM Journal Numereical Analysis*, pp. 257–267.

Vickery, B. J. (1971), On the reliability of gust loading factors, *Cvil Engineering Transactions*, pp. 1–9.

Wahba, G., G. H. Golub, and M. Heath (1979), Generalized cross-validation as a method for choosing good ridge parameter, *Technometrics*, *21*(2), 215–223.

Wang, C. H., and M. W. Brown (1996), Life prediction techniques for variable amplitude multiaxial fatigue, *Engineering Materials and Technology*, *118*, 367–370.

Wilson, A. I. E. L. (1990), A methodology for dynamic analysis of linear structure-foundation systems with local nonlinearities, *International Journal for Earthquake Engineering and Structural Dynamics*, *19*, 1197–1208.

Yeter, B., and C. G. Soares (2013), Spectral fatigue assessment of an offshore wind turbine structure under wave and wind loading, in *Developments in Maritime Transportation and Exploitation of Sea Resources*, pp. 425–433, CRC Press 2013.

Zhu, X., and S. Law (2002), Moving loads identification through regularization, *Journal of Engineering Mechanics*, *128*(9), 989–1000.

Ziegler, F. (1998), *Mechanics of Solids and Fluids*, Second ed., Springer.

Ziegler, F. (2008), Special design of tuned liquid column-gas dampers for the control of spatial structural vibrations, *Acta Mechanica*, *201*(1), 249–267.

Ziegler, F., and A. Kazemi-Amiri (2013), Bridge vibrations effectively damped by means of tuned liquid column gas dampers, *Asian Journal of Civil Engineering (Building and Housing)*, *14*(1), 1–16.

Appendix A

Authorship

Chapter 2 of this dissertation is based on the publication “Derivation of a new parametric impulse response matrix utilized for nodal wind load identification by response measurement” by Abbas Kazemi Amiri and Christian Bucher (*Kazemi-Amiri and Bucher*, 2015). The publication was prepared by Abbas Kazemi Amiri under supervision of Christian Bucher.

Chapter 3 of this dissertation is based on the paper “A practical procedure for inverse wind load reconstruction of large degrees of freedom structures” by Abbas Kazemi Amiri, Christian Bucher and Ruediger Hoeffer. This study was submitted to *Mechanical systems and Signal Processing*. The paper was prepared by Abbas Kazemi Amiri under supervision of Christian Bucher and Rüdiger Höffer.

Chapter 4 of this dissertation is based on the paper “Identification of wind loads from structural responses through full-scale field measurements” by Abbas Kazemi Amiri and Christian Bucher. This study was submitted to the *journal of Wind Engineering & Industrial Aerodynamics*. The paper was prepared by Abbas Kazemi Amiri under supervision of Christian Bucher.

Chapter 5, section 5.1 of this dissertation is based on the collaborative research by Abbas Kazemi Amiri and Patrick Hogan, under supervision of Christian Bucher and Takashi Maruyama. This study is in preparation for submission to a journal. The contribution of Abbas Kazemi Amiri to this paper was:

- Literature review
- Concept development
- Wind and structural data analyses
- Paper writing

Chapter 5, section 5.2 of this dissertation is based on the paper “A new model order reduction strategy adapted to nonlinear problems in earthquake engineering” by Franz Bamer, Abbas Kazemi Amiri and Christian Bucher (*Bamer et al.* (2016)). This paper was recently accepted for publication in *Earthquake Engineering and Structural Dynamics*. The contribution of Abbas Kazemi Amiri to this paper was:

- A part of the literature review
- Formulation of FP element
- Providing FE model of structural system (hospital)
- Paper edition